universität wien

MASTERARBEIT / MASTER'S THESIS

Titel der Masterarbeit / Title of the Master's Thesis

„Two-Dimensional Noble Gas“

verfasst von / submitted by

Manuel Längle, BSc

angestrebter akademischer Grad / in partial fulfilment of the requirements for the degree of

Master of Science (MSc)

Wien, 2020 / Vienna, 2020

Studienkennzahl lt. Studienblatt / degree programme code as it appears on the student record sheet:	A 066 876
Studienrichtung lt. Studienblatt / degree programme as it appears on the student record sheet:	Masterstudium Physik UG2002
Betreut von / Supervisor:	Assoz. Prof. Dr. Jani Kotakoski

To all the people who kept distracting me from finishing this work!

Life would be incredibly boring without all of you.

Abstract

In this work few-layer graphene is irradiated with noble gas ions, which leads to their trapping between the graphene layers and the formation of 2D noble gas crystallites and liquids. Exfoliated few-layer graphene was transferred onto a holey carbon Quantifoil(R) gold grid. The grids were irradiated with low energy ($\ll 1$ keV) and high dose (ca. 10^{15} $\frac{\text{ions}}{\text{cm}^2}$) at the University of Helsinki. The samples were subsequently analysed at the atomic level using the Nion UltraSTEM 100 microscope at the University of Vienna. Our results demonstrate that ions with a suitable energy pass through the first few graphene layers to then become trapped within the structure. It was found that in graphene encapsulation, the noble gas atoms form small two-dimensional crystallites with a remarkable stability under the 60 keV electron irradiation inside the microscope vacuum, and even individual atoms can be imaged. Also liquid phases can be observed. The crystallites and liquids vary in size, and occasionally show dynamic behaviour, presumably triggered by the electron irradiation.

Zusammenfassung

In dieser Arbeit wird die mikroskopische Struktur von Edelgasen – beschränkt auf zwei Dimensionen – untersucht. Dazu wurde mehrlagiges Graphen mit Edelgasen bestrahlt, was zur Implantation dieser Gase zwischen den Graphenlagen führte. Die eingeschlossenen zweidimensionalen Edelgase bildeten Kristallite und Flüssigkeiten, welche im Rastertransmissionselektronenmikroskop atomar abgebildet wurden. Exfolierte mehrlagige Graphenproben wurden auf Carbon-Quantifoil(R)-Probenhalter transferriert. Diese wurden anschließend mit niedrig energetischen ($\ll 1$ keV) Ionen bei hoher Dosis (ca. 10^{15} $\frac{\text{ionen}}{\text{cm}^2}$) an der Universität von Helsinki bestrahlt. Im Anschluss wurden die Proben bei atomarer Auflösung mit dem Nion UltraSTEM 100 Mikroskop an der Universität Wien untersucht. Unsere Ergebnisse zeigen, dass Ionen mit passender Energie durch die ersten Graphenlagen schlagen, bevor sie in der Struktur gefangen werden. Eingeschlossen in Graphen, formen Edelgase kleine zweidimensionale Kristallite von herausragender Stabilität bei Bestrahlung mit einem Elektronenstrahl von 60 keV. Einzelne Atome können abgebildet und flüssige Phasen identifiziert werden. Die Kristallite und Flüssigkeiten variieren in Größe und zeigen dynamisches Verhalten, welches vermutlich durch den Elektronenstrahl ausgelöst wird.

Acknowledgements

I want to thank my supervisor Jani Kotakoski for his tremendous patience and kind help with all of my questions. He has always challenged me while providing me with the tools I needed. Due to his support I was able to do everything I wanted. I am very thankful for that and I'm looking forward to working with him also on the next part of my journey.

I also want to thank Toma Susi, Kimmo Mustonen and Clemens Mangler for the teaching and training they provided and the hours of insightful discussions. They've always had time to help me with my questions and their enthusiasm for science motivated me throughout these last years. Harriet Åhlgren set the basis for much of this work and conducted the irradiation experiments together with me in Helsinki, as well as Alberto Trentino, and I am very glad to have had the support of the two of them. In Helsinki Kenichiro Mizohata supervised me and provided not only the experimental know how but also he gave me and my colleagues there, Anna Liski and Tomi Vuorihimmy, the freedom and possibility to learn about setting up experiments and ion implantation. Without the support of these three the experiments would not have been possible. Also I want to thank Jacob Madsen for helping me with simulating images for this work.

Many thanks also go to Viera Skakalova, who I shared an office with and helped me with interpreting my images, and Mohammad Monazam, who did simulations and discussed the stability of the structures with me. I would also like to thank all my former and present colleagues: Bernhard Fickl, Georg Zagler, Gregor Leuthner, Thi Thuy An Bui, Gudrun Pötzelberger, Heena Inani, Rajendra Singh, Michael Somma, Alexander Markevich, Andreas Postl, Alexandru Chirita, Ursula Ludacka, Stefan Noisternig, Mukesh Tripathi, Daniel Scheinacker and Felix Herterich. We had interesting and insightful discussions as well as fun lunches and evenings. I hope the coming years will be as good as the past ones.

For the process of writing the thesis I want to especially thank Kathrin Linke, who was an immense help during the process of finishing and improving the readability of the thesis, and Sophie Scharinger who gave me feedback on everything I wrote and did not complain but was happy and motivated to read it. Also I want to thank Laura Hödl for reading and correcting my (sometimes awful) spelling.

Special thanks go to Daniel Scheinacker, Mukesh Tripathi, Alberto Trentino and Christina Schmolmüller for providing me with figures for this work.

Also I want to thank all the people who supported me throughout the process of this work while at the same time distracting me and thus prolonging the process of finishing it. Thanks for supporting me during the past, you will have to keep doing that for some more time. It's not always easy with me, but it is never boring.

Five lamps, 23 TEM grids and one deceleration lens were destroyed in the course of this thesis.

List of acronyms

2D	two-dimensional
3D	three-dimensional
FLG	few layer graphene
MD	molecular dynamics
STM	scanning tunneling microscopy
Gr/Ir(111)	graphene placed on top of an iridium crystal oriented in the (111) direction
AES	auger electron spectroscopy
DFT	density functional theory
XPS	X-ray photoelectron spectroscopy
TDS	thermal desorption spectroscopy
STEM	scanning transmission electron microscopy
ADF	annular dark field
FLG	few layer graphene
TEM	transmission electron microscopy
FIM	field ion microscopy
HIM	helium ion microscopy
SEM	scanning electron microscope
EELS	electron energy loss spectrscopy
EDX	energy dispersive x-ray spectroscopy
eV	electron volt
AFM	atomic force microscopy
HOPG	highly ordered pyrolytic graphite
IPA	isopropy alcohol
PMMA	polymethylmethacrylat
FFT	fast fourier transformation
MC	Monte Carlo

Contents

Chapter 1

Introduction

Graphene was first isolated in 2004 [1]. Ever since then, more and more of its fascinating properties have been discovered and different applications have been proposed [2]. Not only are the extraordinary electronic properties very exciting [3], but also its mechanical properties are remarkable. Graphene is, for instance, the strongest material ever measured [4, 5]. Despite being an extremely thin material, consisting of just one layer of atoms, it can withstand a pressure imposed by a macroscopic amount of gas [6] while being impermeable for standard gases including helium at room temperature [7, 8] and exerting a pressure of 1.2 ± 0.3 GPa on trapped atoms in van der Waals structures [9]. In other words, one can take some gas with atoms bigger than helium, put it somehow between graphene sheets and not only does the graphene stay intact and the gas remains trapped inside, it also compresses that gas due to a massive pressure between the layers. This can be used for studying materials that normally cannot be put into vacuum. Graphene has indeed been utilized in its multi-layer form as a two-dimensional (2D) petri dish to study the chemistry of materials via transmission electron microscopy [10, 11, 12]. It has been shown that atoms and molecules thus encapsulated exhibit behaviour unlike their bulk equivalents, including ultrafast diffusion [13] and truncated intramolecular distance [10, 14]. All of the aforementioned properties combined motivated us to implant inert gas atoms into the van der Waals gap between graphene layers to study their diffusion and aggregation into crystals and liquids.

1.1 State-of-the-art noble gas implantation under graphene

Previously, implantation of noble gas atoms has been achieved at the interface between graphene and metal substrates. Graphene grown on an iridium surface in a specific crystallographic orientation, Gr/Ir(111), was one of the studied systems. It was irradiated with different noble gases and studied with surface science methods.

In 2013, Åhlgren et al. [15] used a Gr/Ir(111) system to study the creation of defects in

graphene. Molecular dynamics (MD) simulations and scanning tunneling microscopy (STM)[1] were used to examine the effect of low-energy (0.1 - 1 keV) Ar^+ irradiation. The authors found depressions and protrusions in the STM topography images of Ar^+ irradiated samples, which they interpreted as defects and Ir atoms knocked out of the lattice intercalating between Ir(111) and the graphene layer, respectively. However, in the supplementary material Åhlgren et al. discuss moving and disappearing protrusions, which turn out to be Ar when measured with Auger electron spectroscopy (AES)[2].

A decreasing Ar AES signal for increasing irradiation energy was interpreted as Ar atoms being implanted deeper into the sample. Thus the authors did find implanted argon, but did not mention that in the actual paper but only in the supplement. They do, however, state that there were more and larger protrusions in the surface at higher energies.

In 2014, Herbig et al. [17] conducted a similar study in which the authors irradiated a Gr/Ir(111) interface, with He^+, Ne^+, Ar^+ and Xe^+ at low energies (100 eV - 5 keV) at elevated and room temperatures. After irradiation, the structures were annealed and studied using STM. Similar to Åhlgren et al., protrusions were observed, which were interpreted as C atoms being knocked out of the graphene lattice by ion irradiation forming carbon nanoplatelets, extra layers of graphene between the Ir surface and the covering graphene layer. Herbig et al. relied on density functional theory (DFT) calculations for interpreting the findings, which led them to this conclusion. They noted that the bubbles were bigger for heavier ions but argued that the noble gases stay in the bulk and do not diffuse to the interface.

In [18] Herbig et al. revoked the assumption of the previous paper that desorption of noble gases could not be stopped by the graphene membrane. They used x-ray photoelectron spectroscopy (XPS)[3] to measure the content of Xe in covered and uncovered Ir. The result was that in graphene covered Ir, the characteristic peaks are more pronounced, implying a higher concentration of the implanted species. That was especially visible after annealing the sample. They concluded that Xe trapping by graphene is very efficient even though it does not chemically bind to Ir or graphene and the graphene membrane is heavily damaged. 15% of carbon atoms should have been removed by the irradiation according to MD simulations. They now state that

[1] STM is a technique for imaging surfaces by measuring the tunneling current between an atomically sharp tip and a sample. The tip scans over the sample and if the current, which is exponentially dependent on the distance, is kept constant by adapting the height of the tip, one gains a profile of the sample surface. This technique was established in 1981 by Binnig and Rohrer [16] and has ever since been extremely important for surface science. In STM, one probes the electronic properties of the top layer, not the actual structure of the material. What is beneath the top layer is not detectable unless it affects the electronic surface properties. This makes the interpretation of data difficult, as will be seen in the following.

[2] Auger electrons are produced when bound electrons from energetically lower orbitals of an atom are removed. When these lower shells are then filled with electrons from higher orbitals, the energy difference can either be emitted as an x-ray photon or can kick out an electron from an outer shell. These so-called Auger electrons can be used to analyse the composition of a material. They have very low energy and, therefore, cannot travel far within the sample due to the strong interaction of electrons with matter. That limits the volume where signal can be obtained to the very surface.

[3] In XPS, a surface is irradiated with x-rays while measuring the number and kinetic energy of electrons being ejected. Based on these measurements, calculations about the elemental composition and the chemical and electronic state of the material can be drawn.

formation of noble gas bubbles takes place and leads to elastic deformation of the graphene cover. Bulges form because Xe aggregates at the interface between Ir and graphene. The same occurs for Ne and Ar. These studies show that it is possible to implant noble gases into the interface between graphene and Ir. However, since STM does not directly measure the atomic structure or the composition of the implanted atoms, but only that of the surface, the atomic structure of the implanted noble gas aggregates remained unknown.

In 2015, Herbig et al. [19] demonstrated the effectiveness of trapping Xe at a Gr/Ir(111) interface, even for defective graphene. They investigated the tunability of size, areal density and formation of bulges with and without irradiation damage. The sample was irradiated with Xe^+ at different energies and STM, XPS and thermal desorption spectroscopy, a method where desorbed molecules from a surface are measured as a function of the temperature, were applied. The authors found two effects that are responsible for the efficient trapping of atoms: (1) decreased ion reflectivity up to a few keV. This results from ions easily penetrating through the top graphene layer due to the small scattering cross section after which they do not escape because of the second effect: (2) efficient energy loss in the bulk. They also stated that the strong binding of the irradiation induced graphene edges to the Ir(111) layer makes escaping through there unlikely. The intercalated atoms first form monolayer regions and thus flat bulges. When annealed at higher temperatures, they grow larger, in all dimensions, and form pressurized blisters. The authors suggest that that this formation should occur for all 2D materials which adhere to substrates. Furthermore, it is argued that the gap between graphene and the substrate can be used as pressurized (photochemical) nanocavities or for the growth of substitutional layers between the materials. In [20] Herbig et al. focused on the implantation process. The goal was to find parameters for nanopatterning the same system without atoms getting trapped. Relevant for the present study was the fact that trapping works best at normal incidence.

Finally, in 2018, Yoo et al. [21] succeded in intercalating low energy Kr^+ (30 - 120 eV) below the first layer of graphite, thereby creating a graphite/graphene interface. Since this system is probably most similar to the settings of the present study, the findings of Yoo et al. are most relevant for comparison. In their study, room temperature thermal diffusion of intercalated Kr was found to be almost completely frustrated, i.e. diffusion was barely observable. The growth of Kr nanostructures is explained by already intercalated atoms colliding with incoming Kr. The authors state that the growth of these nanostructures depends on extrinsic variables such as surface vacancies and the local topography of the sample. These affect the diffusion and limit the maximal Kr pressure the sample is able to sustain. Small protrusions were interpreted to be individual Kr atoms at energetically favorable high symmetry sites. Thermal diffusion starts becoming effective at 873 K, causing some nanostructures to enlarge via coalescence, while others disappear through leaking of the pressurized Kr atoms. MD simulations predict that for low energies Kr ions would reflect from the surface and the authors propose that the observed intercalation proceeds through defect sites such as surface vacancies and grain boundaries. Furthermore, depending on the size of the blisters, pressurized Kr atoms can build up enough pressure so that they explode and leave behind craters of varying depth.

1.2 Two-dimensional noble gas on graphite surfaces

Noble gases adsorbed on surfaces were one of the first 2D systems ever studied. Phase transitions in these systems were observed experimentally and studied theoretically for a long time [22, 23, 24, 25, 26, 27, 26, 28]. For krypton on graphite the phase diagram appears to be quite complex having commensurate and incommensurate solid as well as liquid phases. The phases also change with the number of layers covering the surface as the van der Waals interaction of Kr with the graphite potential is quite strong and gets weaker with increasing number of layers.

1.3 Motivation

When studying the effects of noble gas irradiation of graphene on surfaces, the formation of noble gas bubbles has been observed. These bubbles have been investigated thoroughly, however, the atomic structure of the encapsulated atoms stays hidden beneath the surface. Whether they are in a solid, liquid or gaseous phase remains unknown. The phases of two dimensional noble gases on surfaces have also been studied thoroughly. krypton physisorbed on graphite exhibits different solid and liquid phases. This study closes the gap by studying the atomic structure of pressurized two dimensional noble gases encapsulated between graphene layers.

STEM is the main method used in this work. In this method a probe scans the sample, however contrary to STM, it consists of electrons which travel through the sample. Elastically and inelastically scattered electrons are collected from each sample position to gain information about the structure and properties of the material. Via aberration correction, the size of this probe can be decreased down to the order of $1 - 2$ Å, which makes atomic resolution imaging possible. STEM provides so-called Z contrast, Z being the atomic number or charge of the nucleus. It emerges when electrons scattered to large angles are collected using an annular dark field (ADF) detector. This results in atoms acting as individual scattering centres with the scattering cross section depending only on the nuclear charge. In simple terms, this means that atoms with higher atomic numbers appear brighter in images. Additionally, electron energy loss spectroscopy (EELS) can be used to determine the atomic species in the sample. With all of that combined it enables us to investigate the formation and dynamics of intercalated krypton at the atomic level. This will be elaborated in more detail in the methods section.

1.4 Brief explanation of the results

In this work, exfoliated few-layer graphene was transferred onto a holey carbon Quantifoil(R) gold grid to create few layer graphene (FLG) samples with varying thicknesses. The samples were irradiated with low energy ($\ll 1$ keV) and high dose ($\approx 10^{15}$ $\frac{\text{ions}}{\text{cm}^2}$) at the University of Helsinki (Finland), with a 500 kV ion accelerator (High Voltage Engineering) called KIIA operated at

20 kV. A special deceleration lens was developed by our collaborators to reduce the energies to 10-20,000 eV. Depending on the source material, this set-up is able to reach a beam current of several μA and has proven to be a valuable tool to study the effect of low energy and high dose ion irradiation in few-layer graphene.

The samples were subsequently characterized at the atomic level using the Nion UltraSTEM 100 microscope at the University of Vienna. Our results demonstrate that ions with a suitable energy pass through the first few graphene layers and become trapped within the structure. In graphene encapsulation, the noble gas atoms form small two-dimensional crystallites and liquids. The crystallites exhibit a remarkable stability under the 60 keV electron irradiation inside the microscope vacuum, and even individual atoms can be imaged. They vary in size and occasionally show dynamic behaviour, presumably triggered by the electron irradiation. Thus, in addition to protecting the encapsulated materials from vacuum and irradiation damage, the graphene layers can also help in creating structures that would otherwise not be stable.

Chapter 2

Materials

2.1 Graphene

2.1.1 Historical introduction

With the invention of the pencil, graphite became widely known to the world. It is a layered material consisting of a stack of graphene layers bound by the weak van der Waals interaction. Due to the weak binding between the layers, these layers are sheared off easily and stick to paper. A few hundred years after the invention, in 2004, Novoselov and Geim isolated and characterized a monolayer of graphene [1]. As a toy model, graphene has already been studied as a theoretical material in the 1940s [29]. Its discovery was remarkable as before the discovery of graphene, the existence of two dimensional materials without a supporting substrate was believed to be impossible. The discussion goes back to the 1930s when Landau, Peierls and Mermin theoretically showed that perfect 2D crystals cannot exist free standing [30, 31, 32, 33, 34] and Mermin and Wagner proved that a magnetic long-range order could not exist in two-dimensional crystals [35]. In addition, many experiments indicated that if a film gets too thin it becomes thermodynamically unstable unless supported by a substrate. Indeed, perfect crystals are forbidden in two dimensions, however, the stability of graphene can theoretically be explained by having deformations in three-dimensional (3D) space which was confirmed experimentally [36]. A nearly perfect 2D crystal can exist in 3D space if crumbled. The deformations in the third dimension can reach up to seven times the distance between atoms in the lattice.

It's discovery involved some luck, since graphene absorbs 2.3% of incident white light [37]. Detecting this in an optical microscope would be quite impossible. However, graphene produces an optical effect on $90\ \mathrm{nm}$ SiO_2 substrates where the absorption is approximately 12% and it can thus be observed with an optical microscope [38]. Even though it probably has been produced every time someone used a pencil, it was discovered long after graphite, fullerenes or nanotubes which are other famous carbon materials [3].

The properties of graphene are outstanding in many ways [2]. The discovery of its electronic

properties in combination with the easy way of producing it [1] was the foundation of the still developing field of 2D materials [39].

2.2 Structure

The chemical element carbon (symbol C, atomic number 6, atomic mass 12.0107 u) is characterized by the electronic ground state configuration $1s^2 2s^2 1p_x^1 1p_y^1$. The $2s$ and p orbitals can hybridize into two sp plus two p, three sp^2 plus one p or four sp^3 orbitals. The hybrid orbitals determine the structure: sp^3 crystallizes into the diamond-structure, sp^2 into the graphene (or graphite) structure and sp into the carbyne structure, i.e., a one dimensional chain of atoms [40].

Figure 2.1 illustrates the structure resulting from sp^2 hybridization. It is a planar structure in which every atom has three nearest neighbors and an angle of $120°$ between the bonds, thus forming a honeycomb structure. The sp^2 hybrid orbitals form covalent σ bonds, which are very strong and result in the robust lattice structure responsible for the mechanical properties of graphene. Their bands have filled shells and form a deep valence band. The from the hybridisation unaffected p_z orbitals are perpendicular to the planar structure. They are responsible for the formation of a delocalized π-band, which is half filled since each carbon atom has one electron left after hybridization [3]. The average distance between two nuclei (the bond length) is given

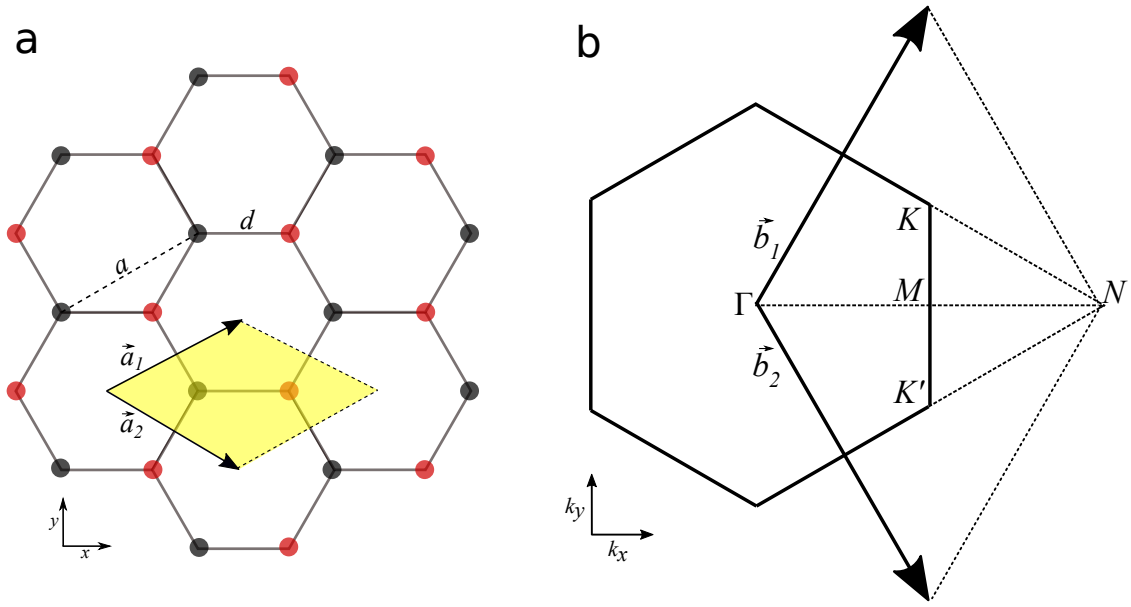

Figure 2.1: Honeycomb lattice structure of graphene and its first Brillouin zone with corresponding symmetry points. (a) Lattice structure of graphene, made of two interpenetrating triangular lattices; $\vec{a}_1$ and $\vec{a}_2$ are the unit vectors. The unit cell is highlighted in yellow. The lattice constant a is 2.46 Å. The bond length d is 1.42 Å. (b) Corresponding first Brillouin zone with the high symmetry points Γ, K, K' and M and reciprocal lattice vectors $\vec{b}_1$ and $\vec{b}_2$. The figures were taken from [41] with kind permission of the author Mukesh Tripathi.

by $d = 0.142$ nm. The real space lattice vectors can be defined as

$$\vec{a}_1 = \sqrt{3}d\begin{pmatrix}\frac{\sqrt{3}}{2}\\ \frac{1}{2}\end{pmatrix},\ \vec{a}_2 = \sqrt{3}d\begin{pmatrix}\frac{\sqrt{3}}{2}\\ -\frac{1}{2}\end{pmatrix}, \tag{2.1}$$

shown in figure 2.1(a). Using the relation between real and reciprocal space

$$\vec{b}_i \cdot \vec{b}_j = 2\pi\delta_{ij} \tag{2.2}$$

we get the reciprocal vectors as

$$\vec{b}_1 = \frac{2\pi}{3d}\begin{pmatrix}1\\ \sqrt{3}\end{pmatrix},\ \vec{b}_2 = \frac{2\pi}{3d}\begin{pmatrix}1\\ -\sqrt{3}\end{pmatrix}. \tag{2.3}$$

The first Brillouin zone, the Wigner-Seitz cell of the reciprocal lattice [40], is a hexagon with the four symmetry points Γ, K, K' and M shown in figure 2.1 (b). In graphene, K and K' are called Dirac points and play an important role in the electronic structure. Their coordinates in reciprocal space are given by

$$\vec{K} = \frac{2\pi}{3d}\begin{pmatrix}1\\ \frac{1}{\sqrt{3}}\end{pmatrix},\ \vec{K'} = \frac{2\pi}{3d}\begin{pmatrix}1\\ -\frac{1}{\sqrt{3}}\end{pmatrix}. \tag{2.4}$$

Figure 2.2 shows a filtered medium angle ADF STEM image of monolayer graphene taken with the Nion UltraSTEM 100.

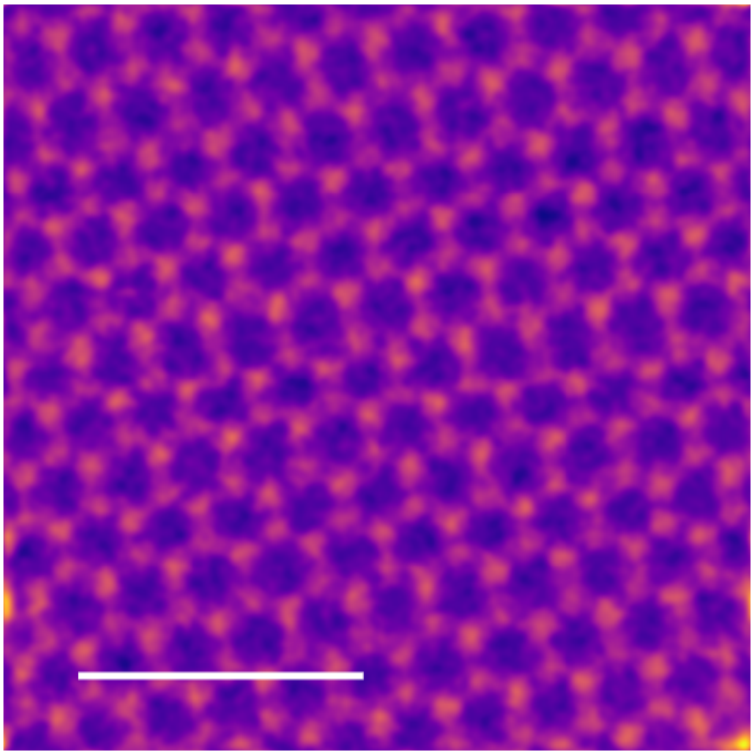

Figure 2.2: Filtered MAADF STEM image of graphene, Scale bar: 1 nm.

2.3 Properties

Reference [3] gives an overview of the electronic properties of graphene, the most prominent of which is the linear dispersion of the band structure around the K and K' points illustrated in figure 2.3, mimicking the physics of quantum electrodynamics for massless fermions, though they move 300 times slower than the speed of light. The energy dispersion relation using the tight binding model [29] is given by

$$E_{\pm}(k_x, k_y) = \pm\gamma_0\sqrt{1 + 4\,\cos\frac{\sqrt{3}k_x a}{2}\cos\frac{k_y a}{2} + 4\,\cos^2\frac{k_y a}{2}} \tag{2.5}$$

where γ_0 is the transfer integral between two neighbouring $\mathrm{p_z}$ orbitals (≈ 3 eV). Around the two Dirac points (K and K') this can be approximated to

$$E_{\pm}(\delta\vec{k}) = \pm\hbar v_F|\delta\vec{k}| \text{ with } v_F = \frac{\sqrt{3}\gamma_0 a}{2\hbar} \tag{2.6}$$

with v_F being the electronic group velocity or Fermi velocity and $\hbar$ being the reduced Planck constant. The derivation of equation 2.6 is given in reference [42]. From the equation it is obvious that the dispersion is linear around K and K'. The bottom of the conduction and the top of the valence band touch at the two Dirac points in the first Brillouin zone at the Fermi level where the density of states is zero. The band structure shows unusual semi-metallic behaviour and the integer quantum Hall effect can be measured up to room temperatures.

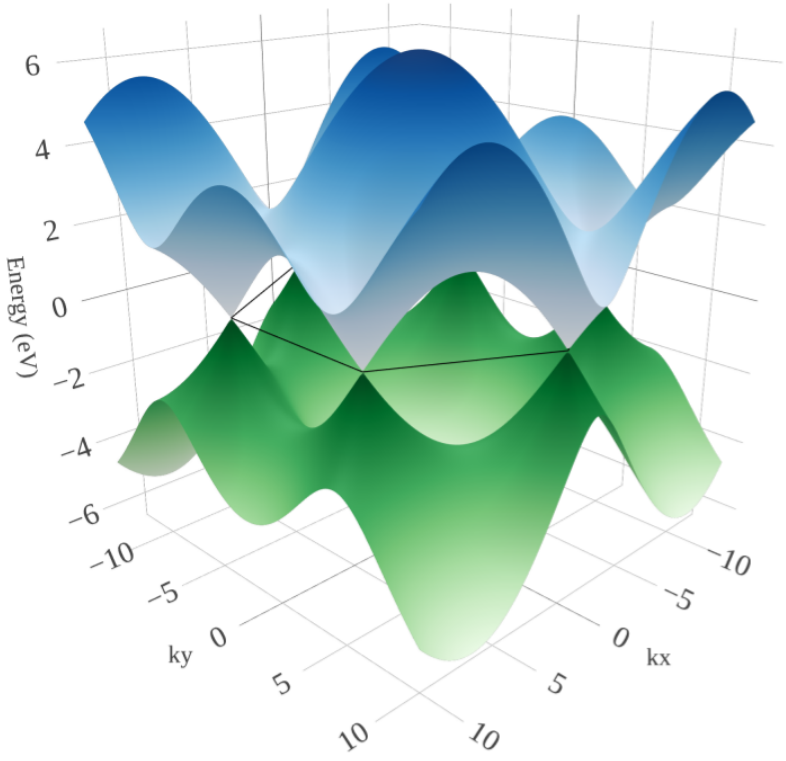

Figure 2.3: Electronic dispersion relation in the honeycomb structure. Plotted with Plotly, code provided by Jani Kotakoski.

The electronic properties of graphene depend sensitively on the number of layers [39]. Whereas in a monolayer there is linear dispersion at the Dirac points and the charge carriers imitate massless Dirac fermions, in a bilayer a small band gap opens, the mass of the carriers is non-zero and they follow a parabolic dispersion [43]. The charge carrier mobility is extremely high [44], providing graphene with an immense electronic, as well as an extraordinarily high thermal conductivity [45]. The maximum current density that graphene can bear is several million times larger than in copper and the electron mobility can reach values up to $2.5 \cdot 10^5\ \mathrm{cm^2 V^{-1} s^{-1}}$, being the highest for any material at room temperature [46]. As a consequence of its unique electronic structure, graphene absorbs 2.3 % of incident white light despite it being only one atom thick [37].

2.3.1 Specific properties relevant for the present study

The use of graphene for the present study has already been motivated in the introduction. Its mechanical strength has been measured using nanointendation [4] and Raman spectroscopy [5]. In reference [7], the authors found that graphene is an impermeable atomic membrane. They investigated the gas leak while changing the pressure outside of a graphene covered hole introducing a pressure difference across the membrane. This was done for varying thicknesses. In [8] the authors investigated the impermeability even further and were capable of discerning permeation of a few helium, neon, nitrogen, oxygen, argon, krypton and xenon atoms per hour with only hydrogen showing noticeable permeation. In [6] Stolyarova et al. showed that graphene can withstand macroscopic amounts of gas. The authors exposed mechanically exfoliated graphene mounted on a SiO_2/Si substrate to HF/H_2O etching or proton irradiation. Gas was released from the substrate and accumulated at the graphene/SiO_2 interface resulting in the formation of bubbles in the graphene sheet. These bubbles were investigated using STM and atomic force microscopy (AFM)[1]. Many studies have been conducted after this on gases and especially inert gases trapped below graphene membranes, some of which were already mentioned in the introduction.

Graphene can also be seen as a (S)TEM sample holder in this study, holding inert gas atoms in place to be imaged. Reference [47] lists the requirements for (S)TEM specimens as to explain why:

1. A S(TEM) specimen should be thin enough for the electrons to pass through with only a modest phase shift. The amplitude should stay the same, meaning that all electrons should pass through the sample.

2. The specimen should be substantially thinner than the mean free path for inelastic scattering processes. This implies that the heavier the atoms in the samples are, the thinner it should be.

3. The electron beam spread induced by the sample should be negligible.

[1] AFM is a technique similar to STM where the interaction between the tip and the surface is not tunneling electrons but the van der Waals force.

4. The specimen should be self-supporting over a large enough region.
5. Surfaces should be far enough apart to measure bulk characteristics and not surface characteristics.
6. Surface contamination should not dominate the signal and thus be kept at a minimum.
7. Scattering events should provide sufficient signal for imaging.

There is no single material that fulfills all requirements given above. However, graphene does fulfill many of them. It is thin, granting points 1-3 and the mechanical properties make it stable being suspended over a large region as shown in reference [36]. Since graphene consists of surface only, the requirements on bulk are irrelevant here, removing point 5. A big issue, however, is surface contamination, point 6. If a specimen is only one layer of atoms thick, every atom sticking to it will disturb the image and cover areas that one would want to observe. This will be visible on most of the images in the results of this thesis. Contamination indeed is one of the biggest issues in atomic resolution electron microscopy and different ways of removing it have been tried in the past. In this work we clean our samples using laser heating as described in [48] and heating with white light sources.

Another problem in electron microscopy is the stability of the specimen under the electron beam. Graphene is very stable since the displacement cross section for an atom is very small, ranging from 10^{-4} barn[2] at 80 kV to ≈ 0.2 barn at 100 keV [49, 50]. The images for this study were taken with an acceleration voltage of 60 kV at which this effect is negligible.

Knowing that graphene is a material which is very suitable for (S)TEM with the additional knowledge that atoms can be trapped between layers, it has been used as a sample support for microscopy for samples which would not survive vacuum or would not even exist without the supporting graphene layers [10, 11, 12, 51]. Materials between the layers show interesting phenomena, for example a pressure of 1.2 ± 0.3 GPa is exerted on trapped molecules between the van der Waals structures [9], very dense stacking of Li and fullerenes was observed [14, 10], but also ultra fast diffusion of Li atoms stuck between the layers [13].

2.4 Free standing FLG samples

To produce free standing FLG samples there are two main approaches. One is to start with a macroscopic crystal and strip it down until only a thin flake is left. This is the top-down approach. The other is starting with individual atoms and building up the sample from these, which is the bottom-up approach. Both of these approaches have been used in this thesis for producing samples. These samples then have to be transferred onto a sample holder, which can be irradiated with ions and imaged in the electron microscopes. TEM holey carbon Quantifoil(R) gold grids have been used for this purpose, if not specified otherwise.

[2] 1 barn $= 10^{-28}$ m^2

2.4.1 Top-down

Different top-down approaches are described in [52]. In general, these methods produce small samples, up to few $\mu\mathrm{m}^2$, and with most of them it is quite hard to control the thickness and size of the samples. The in many ways "best" procedure for producing high quality, $\mu\mathrm{m}^2$-sized samples is micromechanical cleavage, also called the "Scotch tape method" named after the sticky tape producer "Scotch tape". This method was also used for producing the first ever graphene samples [1, 43]. The method is relatively simple and the steps are illustrated in figure 2.4. A crystal of graphite, in the ideal case highly ordered pyrolytic graphite (HOPG), is put on adhesive tape and then reduced in size by bringing the tape into contact and pulling it apart several times. The crystals are spread around a wide area and become smaller and thinner with each repetition as they are being ripped into smaller pieces. In order to find usable FLG flakes they need to be transferred from the tape to a substrate. The tape is thus attached to a piece of a $\mathrm{SiO_2}$-coated Si wafer. The wafer can be plasma irradiated before adhering it to the tape and heated with the tape attached for a higher yield of larger flakes [53]. The contrast of the flakes in the optical microscope depends on the thickness of the $\mathrm{SiO_2}$ coating. It is maximal for $90\ \mathrm{nm} \pm 5$ % for green light and reaches 12 % for a monolayer [38]. The chip is placed under the microscope and checked for transferable flakes, mostly with the 20x magnification objective since it is bright while providing high magnification. One way for doing this is to start at a corner and to raster-scan over the chip, adjusting the focus at all times. If a suitable flake (big enough and varying in thickness) is found, the transfer process can begin.

The transfer process is illustrated in figure 2.5 and described in [54]. First, a TEM sample holder, consisting of gold bars with a holey carbon film attached, is placed on the $\mathrm{SiO_2}$/Si wafer on top of exfoliated graphene in a way that the sample is usable afterwards. The fine adjustment can be done using a micromanipulator, which is a needle connected to three motors. The sample should attach to the membrane and should not be covered by one of the gold bars as the electron beam can not pass through there. If possible, the sample should be placed at a characteristic position close to the centre as shown in figure 2.6. Then a drop of isopropyl alcohol, often called isopropanol or IPA, is used to adhere the flexible carbon membrane on the lower side of the sample holder to the substrate. The grid can be held in place by the micromanipulator. The liquid sits between the grid and the wafer, evaporates and thus pulls the carbon membrane down to the substrate due to its surface tension. There, the membrane sticks to the surface. Then a drop of potassium hydroxide (KOH) is placed on the grid to etch the $\mathrm{SiO_2}$ layer beneath the grid. Once the $\mathrm{SiO_2}$ is etched, the grid loses contact with the wafer and starts floating with the graphene flake being attached to the carbon membrane. After that the grid is washed in deionized water to dilute the KOH and then in isopropanol to remove water and to clean it. The grid is then ready to use. This process is illustrated in figure 2.5.

Using this method, samples can be easily produced and high-quality mono-crystalline flakes are obtained. For industrial applications, these flakes would be too small, but in electron microscopy a few square micrometers are more than enough. The advantage of micromechanical

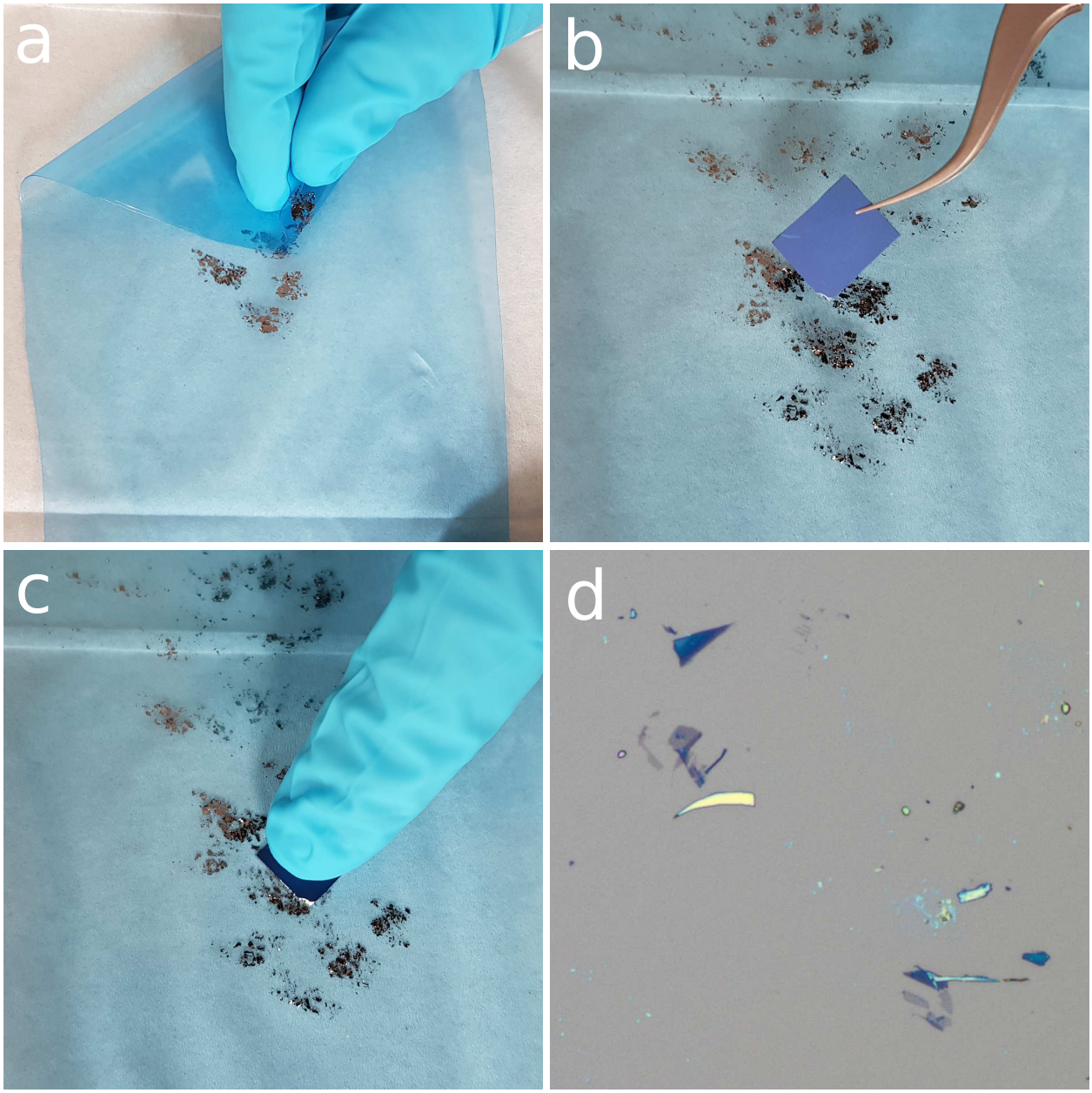

Figure 2.4: Illustration of the "Scotch tape method": (a) Graphite was put on top of the sample. Scotch tape is used to reduce the crystals in size and spread them. (b - c) A SiO_2/Si wafer is put on the tape and pressed against it. (d) The surface of the wafer in a reflected light microscope after the scotch tape was removed. The darker a piece is, the thicker it is. At some thickness the particles become white because they start to reflect all the light. The figures were taken from [41] with kind permission of the author Mukesh Tripathi.

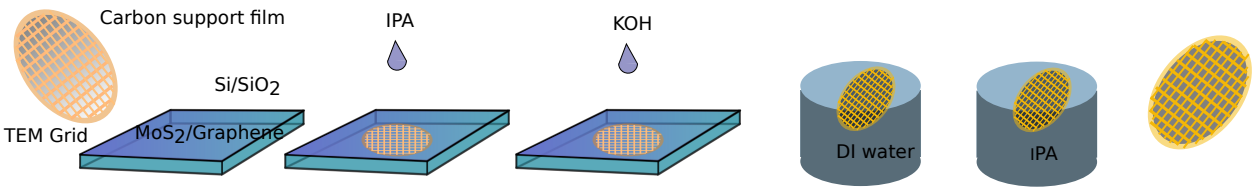

Figure 2.5: Schematic illustration of the transfer process. The figure was taken from [41] with kind permission of the author Mukesh Tripathi.

cleavage most relevant for the present study is that it creates flakes of varying thicknesses next to

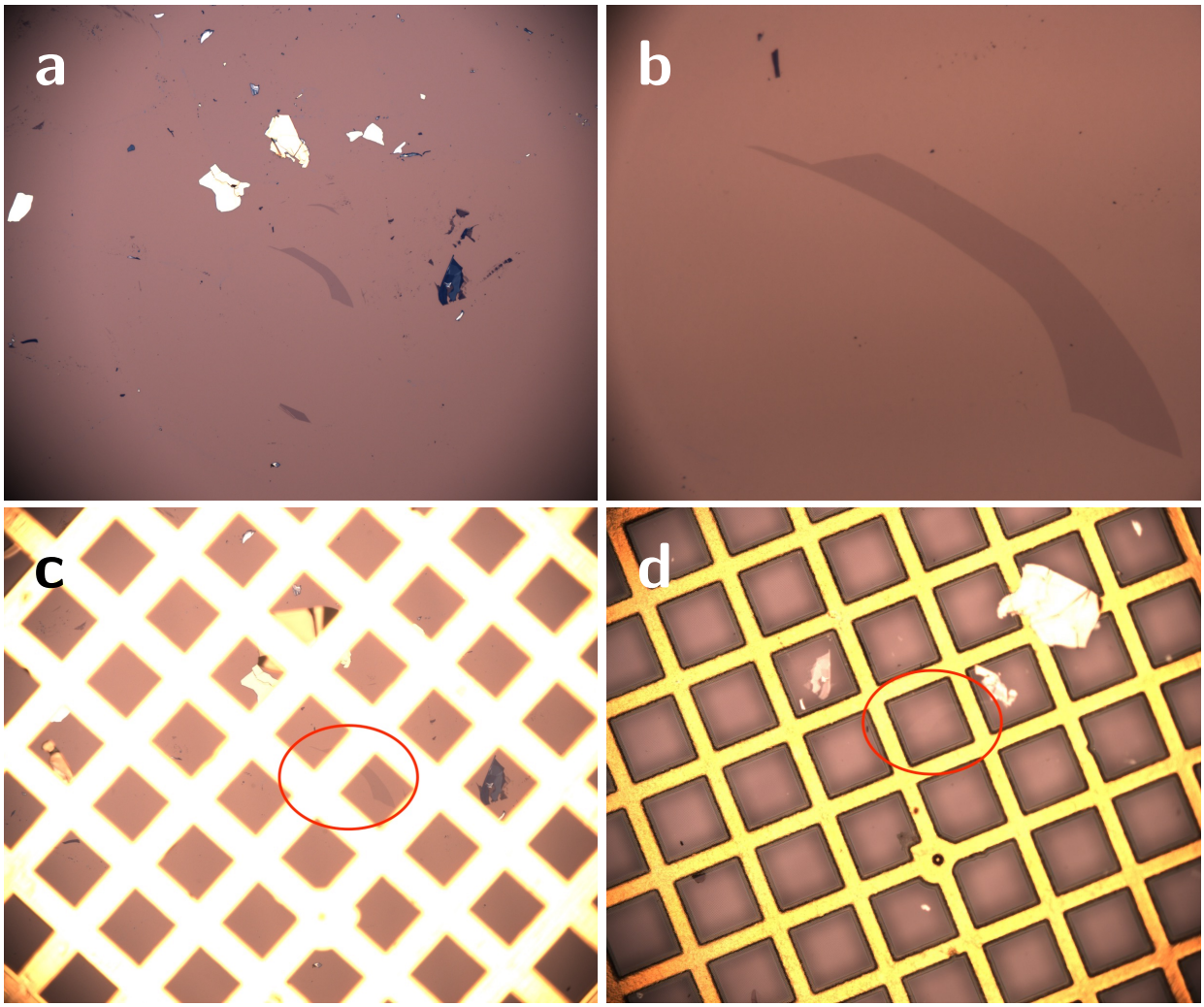

Figure 2.6: Light microscopy image of the transfer process. (a) Isolated monolayer flake at 20x magnification. (b) Isolated monolayer flake at 100x magnification. (c) Flake unattached under TEM grid (d) flake after successful transfer to TEM grid, view from the bottom. From [55] with kind permission of the author Daniel Scheinecker.

each other. This way the irradiation effects and implantation efficiency as a function of thickness can be investigated. The big disadvantage of this method is that it is labour intensive and time consuming.

It is crucial to take images of the flakes before placing the grid on the chip. Once a sample is attached and successfully transferred, it can be difficult to find it, which makes a sample unusable. It is also important that the graphene flake is placed close to the middle of the grid at a position where it can easily be found in the microscope and to prevent the sample from being destroyed or contaminated by touching it with tweezers. After fabrication the samples are put into trampoline boxes which are labelled appropriately.

2.4.2 Bottom-up

Bottom-up describes an approach where a structure is built starting from the individual parts, for example growing graphene from carbon atoms. The method used for the production of some

samples in this work is called chemical vapour deposition (CVD).

Very simplistically, the production of CVD graphene requires an oven, some source material and a substrate. The source material, for example methane, is flowing through the oven. Due to the heat from the oven and catalytic reactions with the substrate, the methane molecules break apart and carbon sticks to the substrate. It then diffuses on top of or into the substrate. Normally copper is used where only surface diffusion is important. After some time the diffusing carbon atoms finds each other and they start forming bonds and building up a structure. The thus grown macroscopic samples have many nucleation sites where they start growing, leading to poly-crystalline samples with grain boundaries [56]. The produced samples can be quite large: even mm-sized samples are easily possible. The quality of CVD graphene is lower than that of exfoliated flakes with regard to intrinsic defects and mono-crystallinity. The CVD samples used for the present study were commercial samples produced by Graphenea[3].

2.4.3 CVD grown double-layers

Since (commercial) CVD grown samples are monolayers by default, they were not directly suitable for the present study. For the irradiation experiments commercially available monolayers were used to create artificial double-layer samples on TEM grids. Note that bilayer and a double-layer are two different samples. A bilayer is exfoliated from a large monocrystal and thus AB stacked with a well-defined crystal structure, whereas a double-layer is produced by putting two monolayers on top of each other at random orientation. This random orientation results in moiré patterns occurring in the lattice as well as two sets of diffraction spots in the electron diffraction pattern (Figure 2.7 (a)). The pattern was taken from a hole in the carbon membrane, covered by a graphene double-layer. Diffraction patterns, among other things, reveal information about the structure of the sample. A monolayer or a, perfectly aligned, bilayer would only show one hexagonal pattern of diffraction spot for each set. In the image two sets of six diffraction spots can be seen. The angular misalignment between the spots (θ) arises from the misalignment of the lattices. Figure 2.7 (b) shows a bright field TEM image of another hole of the same sample. In bright field, the darker a part of an image is, the thicker or heavier material there typically is. Large dark regions can be explained by what happens while bringing two dirty graphene sheets into contact. Due to the pressure between the layers caused by van der Waals attraction between them the contamination is squeezed into these pockets. Surface contamination is also visible in the image. Figures 2.7 (c) and 2.7 (d) show two MAADF STEM images of double-layer graphene samples. Moiré lattices can be observed. They occur when two lattices are put on top of each other with slight misalignment. In figure (d) bright regions are visible. Since in dark field imaging, the contrast is contrary to bright field, so the brighter something is, the more it scatters, bright regions correspond to more material (in this case contamination).

[3] https://www.graphenea.com/

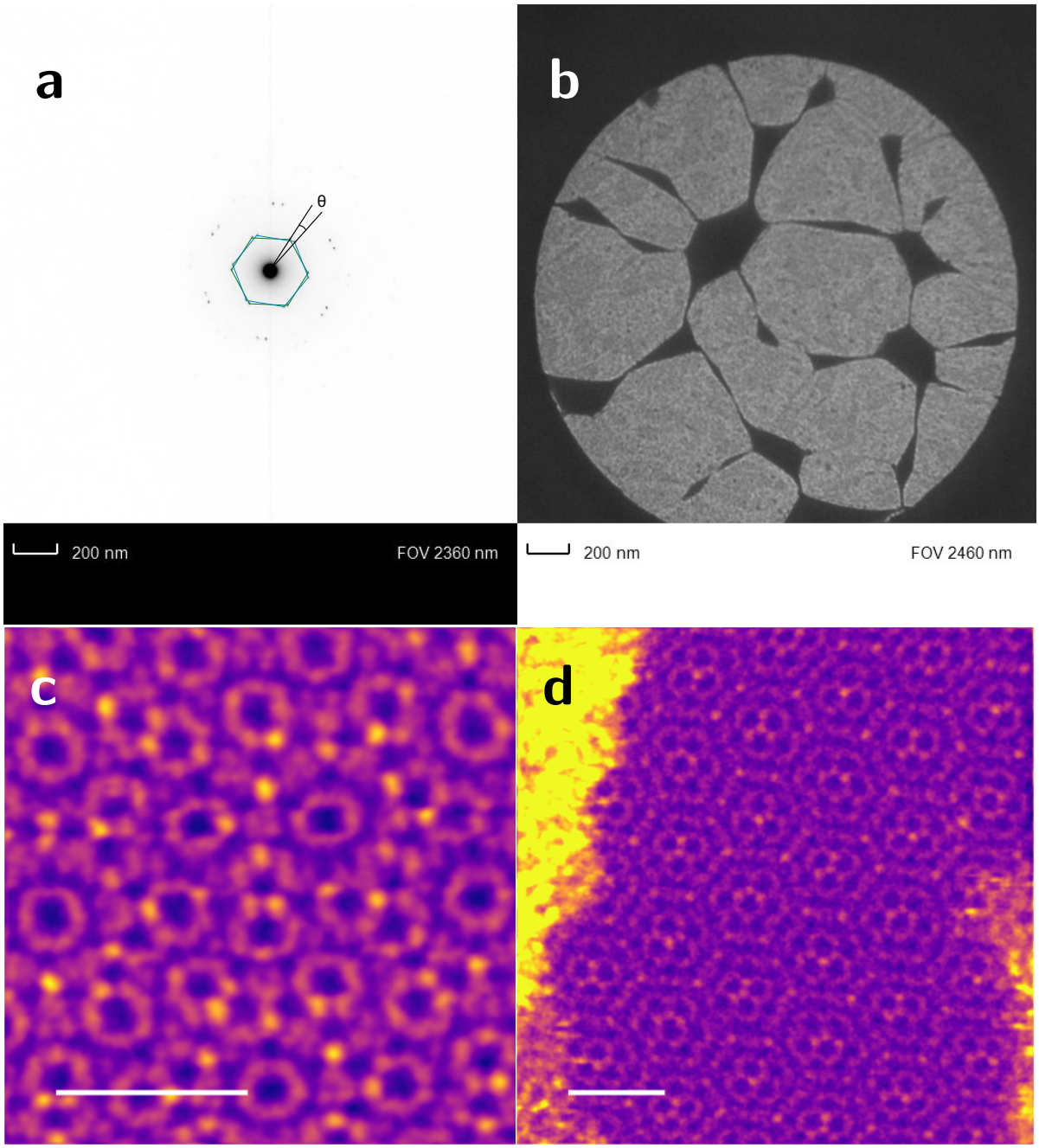

Figure 2.7: (a) Contrast inverted TEM diffraction pattern of CVD double-layer graphene. (b) TEM bright field image of CVD double-layer graphene. Images were taken with Low Voltage Electron Microscope, LVEM5. (c) & (d) Filtered MAADF STEM images of CVD double-layer graphene, scale bar 1 nm; (c) misaligned by roughly 30 degrees, (d) misaligned of roughly 13 degrees

2.4.4 Production of CVD FLG

The samples for this study were produced by taking holey carbon Quantifoil(R) TEM grids, to which graphene has either already been transferred by the supplier or graphene was transferred to by us. The transfer is done by putting "easy transfer monolayer graphene", in our case produced by Graphenea, on top of a polymethylmethacrylat (PMMA) membrane on top of paper. This paper is cut into small pieces and put into water. The paper gets wet and sinks to the bottom

while the PMMA membrane with the graphene is floating on the surface of the water and can be collected with a TEM grid. The grid is then left to dry for 30 minutes and heated on a hot plate at 150 °C for 60 minutes so that the membrane attaches to the grid. According to the instructions, it should also be left in vacuum for 24 hours, but the transfer also works without that and it was time-wise not possible for us to do. Afterwards, the PMMA needs to be removed. This can be done by either putting the TEM grid into acetone for 24 hours or, if cleaner graphene is desired, by putting the grids into a CVD furnace and baking the samples at 400 °C in a controlled Ar/H atmosphere for roughly 4 hours.

Once the first layer of graphene was in place and the PMMA had been removed, a second layer of graphene is placed on the TEM grid. Again the sample was dried and heated as described before. After attaching the second layer, the PMMA was removed in the CVD oven. For the first layer, removing the PMMA was not as critical since the contamination between the layers is going to be squeezed into pockets shown in figure 2.7 (b), whereas the contamination after the second layer stays on the sample.

These processes are not restricted to standard gold TEM quantifoil grids but can also be applied to (more expensive) SiN grids. These have also been used since they are less fragile with respect to high laser powers when the sample is cleaned.

2.4.5 Summary of sample production

Table 2.1 shortly summarizes the advantages and disadvantages of the different samples.

Table 2.1: **Choices of samples for irradiation experiments**

Exfoliated	CVD grown
oriented stacking, varying thicknesses	random stacking, only single or double layers
cheap, labour-intensive	commercially available
small sample at specific location	grid entirely covered with sample
holey Quantifoil membrane	holey Quantifoil or SiN membrane

2.5 Noble gases

Noble gases, also called inert gases, include the elements helium, neon, argon, krypton, xenon and radon. These elements belong to the main-group eight of the periodic table. All of them have full electron shells, which means that they are in the energetically most favorable state. Thus, under standard conditions, they form mono-atomic colourless gases [57].

At low temperatures, they crystallize due to van der Waals interaction, which is also responsible for holding graphene sheets together. This can be understood by looking at electrons around the nucleus. When the electron shell is full, these electrons are, on average, distributed

Table 2.2: **Summarized properties of inert gases.** The table lists the melting and boiling points of inert gases (second and third column taken from [57], fourth, fifth and sixth column taken from [58]).

	melting point [°C]	boiling point [°C]	crystal structure	lattice constant [Å]	conditions
He	-272.2 *	-268.9	hcp	3.531	**
Ne	-248.6	-245.9	fcc	4.43	4.2 K
Ar	-189.3	-185.8	fcc	5.25	4.2 K
Kr	-157	-152.9	fcc	5.72	5.8 K
Xe	-112	-107.1	fcc	6.2	58 K
Ra	-71	-61.8			

* Melting point of He at a pressure of 2.6 MPa. Helium can only condensate when pressurized.
** He^4 1.15 K 66 bar, He^3 3.3 K 183 bar

symmetrically around the nucleus. However, since they are in motion at all times, they can be considered as fluctuating dipoles. Two interacting dipoles create an attractive, though very weak, potential. This interaction provides the second term of the Lennard-Jones potential. The first term is an approximation of the Pauli repulsion. The potential is given by

$$U(R) = \epsilon \left(\frac{\sigma^{12}}{R^{12}} - 2\frac{\sigma^6}{R^6} \right), \tag{2.7}$$

where ϵ and σ denote the depth and the position of the potential well governing this interaction. In atoms with a higher nuclear charge, the outer electrons experience weaker binding to the nuclei. Thus the dipole moment can be larger, which leads to stronger binding between the atoms. The bonding energy per atom is in the order of 0.1 eV resulting in crystals that are unstable at room temperature [40, 42]. Table 2.2 summarizes the melting and boiling points of inert gases.

So far, binding of inert gases has not been observed for He, Ne and Ar. Kr does bind with F as well as Xe, which can form xenonfluorides. Ne, Ar, Kr and Xe are produced by filtering air from the atmosphere, where argon is by far the most common and, thus, the cheapest. Therefore, Ar is most commonly used for creating inert atmospheres for experiments or in light bulbs for longer lifetimes. Helium is mostly used for cooling since it has a very low boiling temperature. Additionally, noble gases are used in lights as they glow when subjected to an electric discharge. Xenon can be used for narcosis without side effects, though it is very expensive. Radon, which is radioactive, is used in medicine as an α radiator [57].

2.5.1 Krypton

Krypton has the atomic number 36 and a van der Waals radius of 202 pm. The reason for using it in the experiments was that the high atomic number would provide increased contrast as compared to argon and it would thus be easier to find in the electron microscope.

A fun fact about krypton is that it was used for the definition of the meter for 23 years,

from 1960 to 1983 [59]. During that time, the meter was defined as 1,650,763.73 times the wavelength of light emitted by the krypton-86 isotope until it got redefined by setting the speed of light as 299,792,458 $\frac{\mathrm{m}}{\mathrm{s}}$.

Krypton, as well as other noble gases, was one of the first ever studied two-dimensional systems. Noble gas atoms on surfaces at low temperatures were considered two-dimensional and phase transitions in these systems were studied already in the 1970s and 1980s [22, 23, 24, 25, 26, 27, 26]. The phase behaviour of adsorbed krypton appears to be quite complex. There are different phase transitions, commensurate and incommensurate solid and also liquid phases. The transitions also change for different coverages. The first few layers appear to be affected by the strong van der Waals potential of graphite, whereas starting at the third layer this is not the case anymore. The adsorbed layers act as independent two-dimensional system, where a monolayer acts quite differently from a bilayer and there have been observations of order-disorder transitions [28].

Krypton has also been in the discussion for being used in Hall thrusters for space travel [60]. Krypton implanted between FLG layers is very dense, and graphene would be the lightest material one could use for encapsulating it. Thus, theoretically, krypton implanted bilayer graphene would make an excellent tank for space travel, being as light as theoretically possible while providing very high fuel density. One would need to come up with an easier way to get it in and out, though.

Chapter 3

Methods

The goal of this work is to study and characterize the atomic structure of encapsulated noble gas bubbles with STEM. For this it was investigated how noble gases and other atoms implant into the van der Waals gap between graphene layers. In this chapter, aberration corrected STEM will be introduced as the method used for these observations as well as ion implantation which is needed for creating the studied structures. Furthermore the analysis of the collected data, which was done in a Jupyter Notebook, using self-written code, will be described. The instruments used were the NION UltraSTEM 100, an aberration corrected dedicated STEM instrument located in Vienna, and the ion implanter KIIA located in Helsinki.

3.1 Scanning transmission electron microscopy (STEM)

In modern microscopy, electrons are most commonly used to gain microscopic structural information about a sample. The structure of materials has significant impact on their properties. Thus, when new materials are to be discovered, created and understood, it is crucial to understand the microscopic structure. Aberration corrected scanning transmission electron microscopy (STEM) is one of the current state-of-the-art techniques in microscopy. Here, an introductory discussion of STEM is given. For more details, see [47], which also served as the basis for this section.

Transmission electron microscopy (TEM), a complimentary and more commonly used method was used here only for pre-characterisation and will thus not be discussed (see [61] for a very detailed and in-depth discussion about the method).

Electrons are superior to visible light with respect to high resolution imaging since they can resolve much smaller features, atomic distances in the order of Å, compared to few hundred nm. However, difficulties such as aberrations and beam damage arise when using electrons for imaging or spectroscopy. Nevertheless, decades of improvements in instrumentation and theory have led to the point where electron microscopes can be used to study materials at the atomic level.

3.1.1 Particles as probe

The resolution of every microscope is ultimately limited by the Abbe diffraction limit

$$d \geq \frac{\lambda}{n \cdot \sin(\alpha)} = \frac{\lambda}{NA}, \tag{3.1}$$

where d is the spatial resolution, λ is the wavelength of the particle used, n is the refractive index of the lens and α is its collection angle. Since the last two variables are given by the instrument, they are often summarized as the numerical aperture NA, which normally is in the order of 1 for optical light microscopes [62]. The length scale of interest is the interatomic spacing, which is in the order of an Ångström (10^{-10} m). Equation 3.1 tells us that the wavelength of the particles for resolving these structures has to be in the same order of magnitude or shorter.

Louis de Broglie postulated that every massive moving particle has a corresponding wavelength [63]. This wavelength λ_{dB} is defined as

$$\lambda_{dB} = \frac{h}{p}, \tag{3.2}$$

where h is the Planck constant and p is the momentum of the particle, which in the non-relativistic case is given by $p = \sqrt{2m_0E}$, with m_0 being the rest mass and E being the kinetic energy of the particle. Thus, the wavelength of particles depends on their energy. If a particle with charge e travels through a potential U, it gains the energy eU. Knowing that, the non-relativistic de Broglie wavelength can be written as

$$\lambda_{dB} = \frac{h}{\sqrt{2m_0eU}}, \tag{3.3}$$

which, for relativistic particles, becomes

$$\lambda_{dB} = \frac{h}{\sqrt{2m_0eU}} \frac{1}{\sqrt{1 + \frac{eU}{2m_0c^2}}}. \tag{3.4}$$

For example, if electrons travel through a potential of 60 kV, this results in a wavelength of $\lambda \approx 5$ pm using equation 3.3, or $\lambda \approx 4.8$ pm using equation 3.4. Even for the electron relativistic effects are negligible at this energy. In principle every particle with a short enough wavelength should be usable to resolve structures.

Different particles

A requirement for building a microscope is the manipulation of the probe particles used. A microscope has to be able to focus the particles to a small area to gain information from that area. Different particles, or waves, will be briefly discussed in the following with regard to wavelength, types of interactions and technical feasibility.

X-rays are electromagnetic waves with wavelengths ranging from a few nm to a few pm. The corresponding energy of the photons ranges from few hundred eV to few hundred keV as can be calculated using

$$E = \frac{hc}{\lambda} \tag{3.5}$$

with E being the energy, h the Planck constant, c the speed of light and λ the wavelength. X-rays are difficult to produce at high brilliance[1] without big facilities such as synchrotrons. Additionally, they have the disadvantage that it is very difficult to build optical components for them, meaning that a beam cannot be properly focused. Focusing elements that exist are bent monocrystals using Bragg reflexes that loose a lot of intensity. X-rays are commonly used for taking diffraction patterns with which the crystal structure of materials can be concluded. However, they are not suited for imaging purposes.

Alternatively, neutrons can be used. At relatively low energy, ≈ 80 meV, they have a short wavelength, ≈ 1 Å, resulting in little irradiation damage in the sample. It is, however, very hard to build optics for neutrons since they are neutral particles and thus do not interact electromagnetically but only with the nuclei of atoms. Additionally, one needs a nuclear reactor for the production, which is costly.

Charged particles on the other hand are relatively easy to manipulate electromagnetically. Protons, which are similar to neutrons in the sense that they have approximately the same mass, thus the same wavelength, require a nuclear reactor, which is expensive, as do positrons. The latter have the added disadvantage of needing an extremely good vacuum since they annihilate every electron they meet. Protons however are indeed used for microscopy, as are muons, particles with the same charge as an electron but with higher mass. These techniques are quite exotic though. Another technique that is more widely in use is ion microscopy. Ions are easy and cheap to produce and they interact electromagnetically, which makes them easy to manipulate. Field ion microscopy (FIM) is a technique where gas flows next to a tip at a high potential. The gas is ionized and accelerated away from the tip towards a phosphorous screen where an image of the tip is thus created. In helium ion microscopy (HIM) a focused helium ion beam is scanned over a surface to collect information about the topography and composition of it. At every point, secondary electrons (electrons that get kicked out from the valence band) Auger electrons, characteristic x-rays etc. can be collected and used for image creation and spectroscopy, similar to what will be described in this chapter. Instruments for HIM have been commercially available since 2007. The technique provides very good contrast, has reached a surface resolution of 0.24 nm, and minimizes sample damage due to the light mass of the helium ions. Heavier ions tend to cause too much damage to the sample due to the higher momentum transfer and are often instead of microscopy used for nanopatterning.

Electrons are charged particles that are very light, the mass is around $\frac{1}{7000}$ compared to a

[1] Brilliance is a quantity which describes the quality of a source. It is defined as $\text{brilliance} = \frac{\text{photons}}{\text{second}\cdot\text{mrad}^2\cdot\text{mm}^2\cdot 0.1\%\text{BW}}$ with BW being the bandwidth of 0.1 % of the central wavelength or frequency. It contains information on the number of photons, the angular divergence of the photons, the cross-sectional area of the beam and the energy spread of the beam.

helium ion, which means that they can be focused more easily and they induce even less damage to the sample. Furthermore, there exist electron sources with extremely high brightness (current density per unit solid angle). Therefore, electrons are the particle of choice in most modern microscopy set-ups. With their wavelength of the order of pm for 60 keV electrons, assuming a perfect optical system, it should easily be possible to resolve structural features in the order of Å.

3.1.2 Electron scattering

Scattering processes are traditionally divided into elastic and inelastic scattering. A process is called elastic when, in the center of mass frame (the inertial frame where the center of mass is at rest) the total kinetic energy of the system does not change. This implies that the energy lost by the impinging particle, in our case the electron initially hitting our sample, is too small to be detected. In inelastic scattering, on the other hand, the particle interacts with the specimen so that the energy change is significant and thus can be detected.

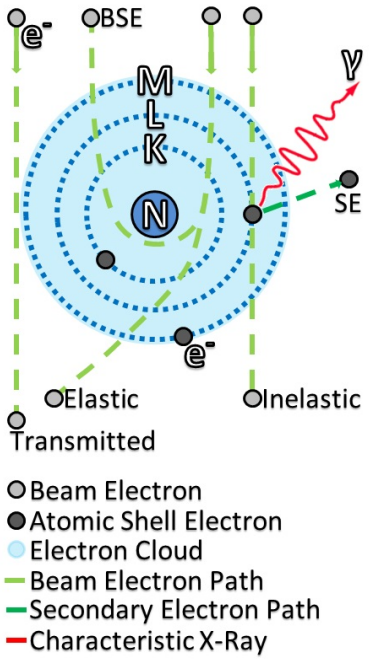

Figure 3.1: Illustration of possible interactions of a primary electron with an atom. K,L and M indicate the electron shells. N referes to the nucleus of the atom. Primary electrons travel from top to bottom. In elastic scattering, the trajectory is altered from its normal course. This can even result in back scattered electrons (BSE). In inelastic scattering, a primary electron excites some kind of internal degree of freedom resulting in a significant amount of energy loss of the impinging electron, in this figure it ejects an electron from the atomic cloud. Ejected electrons are called secondary electrons (SE). γ is a characteristic x-ray photon, which is created when an electron from the inner shell is kicked out and this hole is then filled up by an electron from an outer shell. The energy difference between the two states is released as an x-ray photon. This figure was created by IndianFace and published under the GNU Free Documentation License Version 1.2

In elastic scattering, the primary electron interacts with the electrostatic potential of an atom,

which is an attractive potential created by the protons in the nuclei screened by the surrounding electron cloud. This form of scattering can be used to create images since the interaction changes the trajectories of electrons providing information about the positions of the nuclei, and thus atoms, in the specimen. This type of scattering is used in annular dark field (ADF) imaging. Inelastic scattering involves interactions between the primary electron and electrons, phonons, plasmons, etc. in the material. This can be exploited to gain information about the properties of the material, for example using electron energy loss spectroscopy (EELS) or energy dispersive x-ray spectroscopy (EDX).

Every process has an associated cross section σ, which corresponds to the probability of that specific process happening. In simple words, one can say that if the area of the cross section is hit by an electron, this process will occur. Another useful term is the mean free path, Δ, which describes the path an electron can travel through a sample without interacting with it. The following relationship holds

$$\Delta = \frac{1}{N_V \sigma}, \tag{3.6}$$

where N_V is the number of scatterers (atoms) per unit volume.

3.1.3 Inelastic scattering

Energy conservation and quasi particles in solids are fundamental concepts. Inelastic scattering connects them in such a way that if our primary electron loses a significant amount of energy, it excites some kind of internal degree of freedom. This is called an interaction with either a particle, like an electron, or a quasi particle, like a phonon, plasmon, etc. In the following, the most important interaction processes in the investigated system are introduced.

Phonons

Phonons are vibrational states in a crystal lattice, which have energies in the order of meV to few eV. This energy is too low to be resolved using the NION Ultra STEM 100 available for the current study, even though the cross section for this process would be the largest, and will therefore not discussed in greater detail. In general, it is possible to resolve phonons by using monochromated instruments, i. e. all electrons have the same energy, and improving the resolution of the EELS spectrometer.

Plasmons

Plasmons are excitations that correspond to a collective movement of electrons in the sample and have energies in the order of tens of eVs. They appear in metals and non-metals, have a broad energy spread and cannot be used to uniquely identify elements. The mean free path for these excitations is approximately 100 nm, which is large enough for them to be clearly visible in

the spectrum.

Ionisation of atoms and interband transitions

Impinging electrons experience energy loss when colliding with a bound electron. Depending on the transferred energy, the bound electron is either transferred to an unoccupied state or ejected into vacuum. The cross sections for these processes are small, i.e. the mean free path is often larger than one μm, but the energy loss is characteristic since the bound electron had a specific binding energy. This energy does not only depend on the element but also on the bonding state. Some electrons of the primary beam lose energy and these losses can be observed as edges in the energy spectrum which correspond to core binding levels. The shape and the fine structure of the signal reveals information about the bonding and environment of the atom since that determines the empty energy states available for the electron. When there are empty states in inner orbitals of an atom, they get filled by electrons sitting in higher orbitals. The energy difference can be emitted as x-rays, which can be used for EDX. The different processes are illustrated in figure 3.1.

3.1.4 Elastic scattering

Elastic scattering can be described with equation

$$\frac{\mathrm{d}\sigma}{\mathrm{d}\Omega} = \frac{4\gamma^2 Z^2}{a_0^2 q^4}, \tag{3.7}$$

where the magnitude of the scattering vector is given by $q = |\vec{q}| = 2k \cdot \sin(\theta/2)$ with θ being the scattering angle, $\gamma = \sqrt{1 - v^2/c^2}$ being the relativistic factor with c being the speed of light and v being the speed of the particle, Z being the atomic number, and $a_0 = 0.529 \cdot 10^{-10}$m, the Bohr radius [64]. The scattering centres being not only nuclei, but nuclei screened by the surrounding electrons, can be taken into account by adding a screening radius r_0^2 so that q^2 is replaced by $q^2 + r_0^2$. During the scattering process, the trajectory of the electron is changed, it is scattered at an angle θ. Using a ring-like detector behind the sample, the electrons whose trajectories have been altered to a certain angular range can be collected, which is illustrated in figure 3.2 (left) after the projector lens, where the beam is split up into a central beam travelling upwards, and a beam hitting the detectors. This is the basis of annular dark field (ADF) imaging.

3.1.5 Set-up of a STEM

Figure 3.2 shows a schematic drawing and a photograph of the Nion Ultra STEM 100 in Vienna. The electron beam travels from bottom to top. Electrons are emitted from a cold field emission gun, which is used since it has a very high brightness and a narrow energy spread, which is important with regard to aberrations and spectroscopy, as will be discussed later.

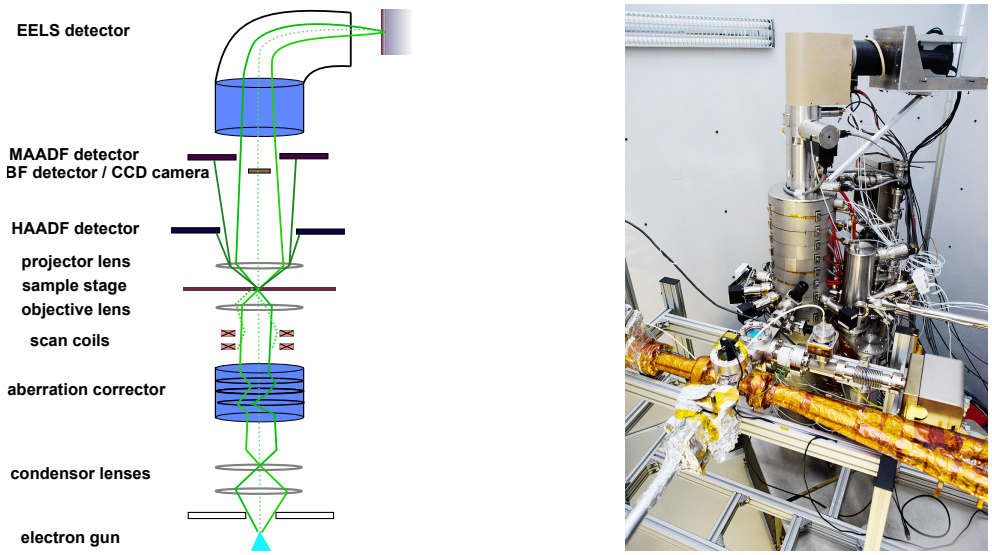

Figure 3.2: Left: Schematic set-up of a scanning transmission electron microscope with the electron beam going from bottom to top. Taken from [41] with kind permission of the author Mukesh Tripathi. Right: Photograph of the NION Ultra STEM 100 in Vienna. From `https://physnano.univie.ac.at/equipment/nion-ultrastem/`.

The emitted electrons are accelerated upwards by an electrostatic lens and travel through an aperture, which defines the collection angle, α, mentioned in equation 3.1. After passing through the aperture, they are manipulated into a convergent beam by the condenser lenses before they reach the aberration corrector. There the aberrations, which have been previously measured, are corrected. There are two scan coils that move the probe across the sample by first tilting the beam in a certain direction and then tilting it back so that it is realigned. The magnification of the microscope is given by the scanned area. At the sample, the objective lens creates the probe. The lens can be very strong, with a focal length of only a few millimeters, and is the key to the resolution of the microscope since it is responsible for the spot size of the electron beam. The probe hits the sample and interacts elastically or inelastically with the specimen. Finally a projector lens is used to spread the beam and the electrons can be collected using different detectors.

3.1.6 Electron lenses

Lenses are used for shaping the electron beam. Since at any point in time there is only one electron in the microscope column, this is the same as altering individual electron trajectories. There are two types of lenses: electrostatic and electromagnetic. The first one could for example be a plate at a high potential, which creates an electric field, while the second one could be a wire with a current passing through, which creates a magnetic field. These fields interact with an electron according to the Lorentz force

$$\vec{F} = -q(\vec{E} + \vec{v} \times \vec{B}), \tag{3.8}$$

where $\vec{F}$ describes the force, $\vec{E}$ the electric and $\vec{B}$ the magnetic field, $\vec{v}$ the speed and q the charge of the particle. Electrostatic lenses are usually used to extract electrons from the electron gun and to accelerate them towards the specimen. However, they are less used for fine changes in the trajectories, because they are quite sensitive to contamination on surfaces, which is almost impossible to control accurately.

For that reason electromagnetic lenses are used for changing electron trajectories. They are usually rotationally symmetric coils, where a current is passed through to create a magnetic field. Electrons travelling on-axis through the lens experience no force, since their trajectory is parallel to the magnetic field. Off-axis they start performing a cyclotron motion around the field lines. The path of the electrons will be a helix, which spirals towards the center due to the lower magnetic flux there. Thus the beam is focused at the focal length, which is proportional to $|\vec{B}|^2$. Consequently, the focus can be controlled by changing the current that runs through the lens coils which creates the magnetic field.

3.1.7 Aberrations and corrections

In an ideal optical system, every point on the object will be perfectly reproduced in the image. This is illustrated in figure 3.3 (a). Distortions from this are called aberrations, which can occur in a variety of forms due to different reasons. As discussed in section 3.1.1, the resolution limit is determined by the wavelength and the quality of the optical system. In (optical) light microscopy, lenses can be corrected rather easily, which means that the resolution is limited only by the wavelength. In contrast, the limiting factor in electron microscopy are aberrations.

Chromatic aberrations arise when an electron beam is not monochromatic, which means that not all wavelengths in the beam are the same. It is known from equation 3.4, that if the energy of two electrons is different, so is their wavelength. This can either happen due to inherent energy spread from the electrons emitted from the source, fluctuations in the electron gun or accelerating voltage or different energy losses from interactions with the sample. As trajectories of electrons with different velocities are altered differently (see equation 3.8) they are not focused into the same spot, which is illustrated in 3.3 (d) where different colours represent different energies. Although the microscope used in the present study does not have a monochromator, i.e. a means to correct chromatic aberrations, the energy spread of the electron gun is small enough for this to not be the limiting factor for image creation.

Atomic resolution is most seriously limited by monochromatic aberrations. They include spherical aberration, astigmatism, coma, curvature and distortion, some of which are illustrated in figure 3.3. Spherical aberration describes the phenomenon of over-focusing electrons which are further away from the optical axis. If that happens, not all electrons hit the same spot on the sample resulting in a blurred out image. For decades this has been the limiting factor in electron microscopy. Already in 1936, Scherzer found that electron lenses have spherical aberration if they are used for producing a real image of an object, have axially symmetric fields, no space

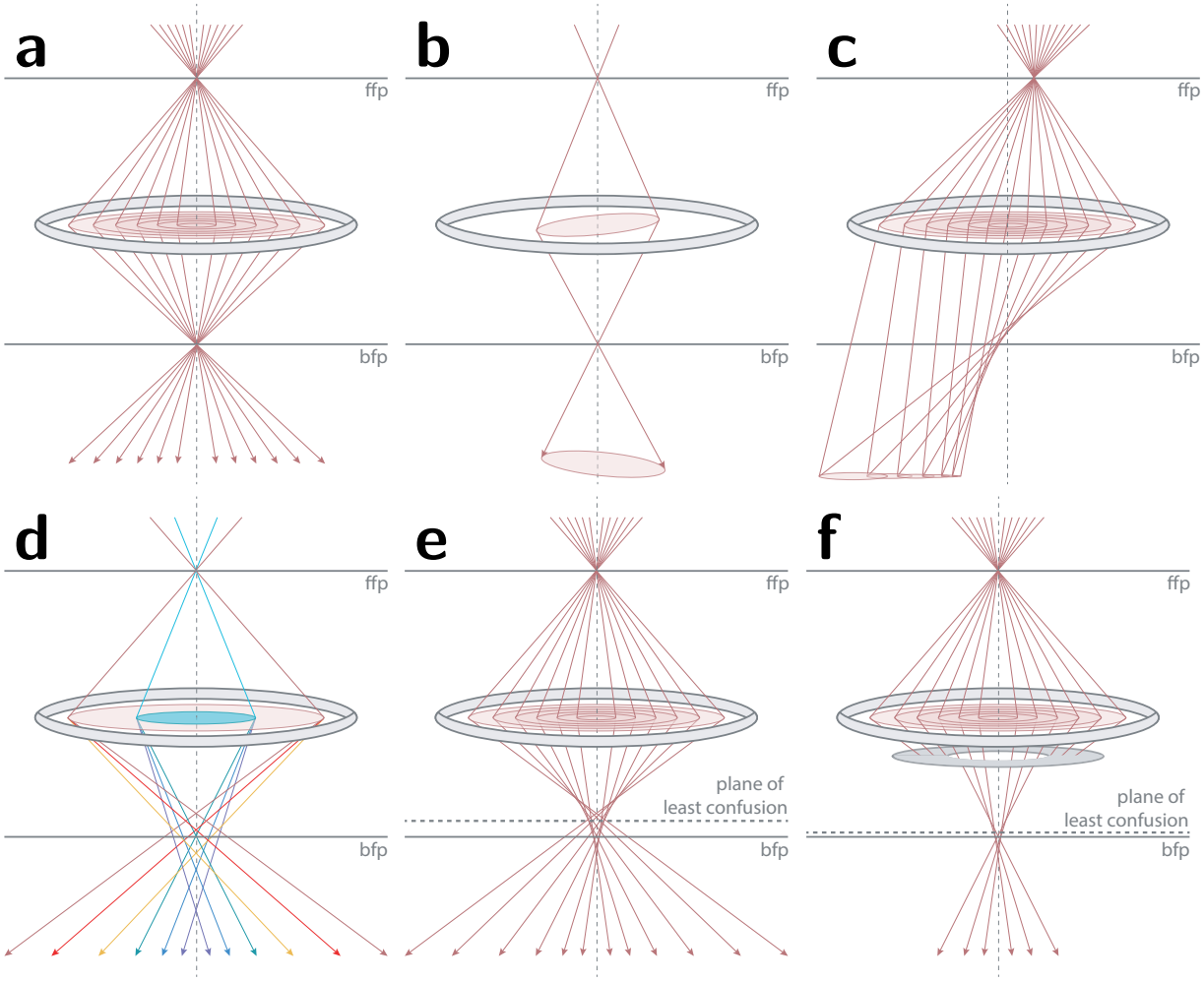

Figure 3.3: Illustration of different types of aberrations (a) aberration-free beam, (b) two-fold astigmatism, (c) off-axis coma, (d) chromatic aberration, (e) spherical aberration, (f) spherical aberration, (g) aperture limited beam; From [55] with kind permission of the author Daniel Scheinecker.

charge and time independent fields, whereas other types of aberration are in principle fixable [65]. In 1947, Scherzer theoretically analyzed different ways for aberration correction of round lenses and proposed a corrector design based on multipole lenses creating non-axially symmetric fields [66]. In the paper he also introduced the so-called Scherzer defocus that balances aberrations by underfocusing the lens, which is important in TEM. The highest obtainable resolution with such a setting is around 50 times the wavelength of an electron with a kinetic energy of 100 keV.

In a simplistic picture, one could say that every round lens overfocuses the electron beam. If the collection angle α in equation 3.1 is increased, stronger aberrations are introduced. However, if the collection angle is decreased, we limit the information we can collect from the sample. If the collection angle is chosen like in figure 3.3 (f), the disk of least confusion is minimized. It characterizes the smallest spot size of the electron beam after the lens and lies in the plane of least confusion as illustrated in figures 3.3 (e) and (f).

After the first aberration corrector had been suggested, it took 50 years for the first working quadrupole/octupole probe corrector to be developed for STEM [67, 68], which soon proved to

be able to do directly interpretable sub-Å imaging [69]. The history of this is laid out in [47]. Relevant papers are also listed on the homepage of the company Nion[2].

Compensating aberrations is complicated. In the Nion UltraSTEM 100, a combination of four quadrupoles and three octopoles is used to correct the aberrations of the other magnetic lenses, primarily the objective lens. First, the beam is squeezed into a thin line. This highly elliptical beam is then manipulated by an octopole lens along its direction thereby forcing negative spherical aberration upon it. The beam is then rotated towards the other axis and subjected to negative spherical aberration again. Finally, the beam is rotated again and returned back to a circular form. In order to carry out the process, the aberrations of the beam have first to be measured and then corrected iteratively since every change in the beam shape introduces new aberrations. Aberrations are measured using the ronchigram method by which well-defined beam shifts are done on an amorphous spot of the specimen and images are collected with a ronchigram camera [70]. From those, the local magnifications are calculated and the aberration function can be obtained. This process needs very fine electrical tuning of the lenses using a computer algorithm (see [47] for a more detailed description).

3.1.8 Detectors

The strength of a dedicated STEM instrument is that many detectors can be used simultaneously to collect the elastically and inelastically scattered electrons. For example ADF detectors and an EELS set-up can be used at the same time since they do not interfere with each other, see figure 3.2 (a).

Ronchigram camera

The ronchigram camera is a CCD[3] which, in our case, makes digital images of a luminescent film hit by the electron beam. It is mostly used for navigating around the sample and tuning the beam as previously described. It can also be used for collecting convergent beam diffraction patterns.

Annular dark field (ADF) detectors

ADF imaging, first used by Crewe in 1970 [71] and described in his paper from 1980 [72], makes use of electrons, which are scattered to angular ranges, $\theta_{min} < \theta < \theta_{max}$. It uses a ring-like detector where the unscattered electrons pass through the hole in the middle and the scattered electrons are detected. This is a very powerful technique due to the incoherent image formation process. Intensities detected by the ADF detectors are integrated scattered intensities by each atom, resulting in the so called Z-contrast [73]. The minimum angle, θ_{min}, should be large enough for Bragg reflections to be suppressed and thus diffraction contrast being eliminated.

[2] http://www.nion.com/resources.html
[3] A CCD (charged-coupled device) is essentially a digital camera.

Then only the result of Rutherford scattering of single scattering centres are observed. The corresponding intensity depends on the atomic number as Z^{ζ}, thus called Z-contrast, with ζ in the range of $1.5 - 1.8$, depending on the signal collection geometry and the atomic number of the studied elements [74]. This leads to a straightforward qualitative interpretation of atomic resolution ADF images by providing a high contrast between atoms with higher and lower atomic number Z which allows to probe the local atomic structure and to directly identify defects and hetero atoms.

In high angle annular dark field (HAADF), the angular range in our microscope goes from $\theta_{min} = 80$ mrad to $\theta_{max} = 300$ mrad. The resulting Z contrast in our set-up is given by $\zeta = 1.64$ [75]. Since the intensity depends on the composition of the specimen, HAADF imaging is well-suited for finding new structures made of heavy atoms. If the probe is small enough to interact with each atom individually, the atomic composition can be resolved.

In medium annular dark field (MAADF), the detector collects electrons from smaller angles, in our set-up $\theta_{min} = 60$ mrad to $\theta_{max} = 200$ mrad. This leads to a higher intensity and thus better contrast for light elements such as carbon, but the accurate Z-contrast is lost and the images are not as easily interpretable.

In ADF imaging, the electron beam is raster-scanned across the sample. Electronics correlate the recorded position of the beam with the number of electrons hitting the detectors. The more electrons are scattered to the angular range, the brighter that pixel is. Thus, heavier atoms and thicker areas appear brighter in the images.

3.1.9 Electron energy loss spectroscopy (EELS)

STEM EELS allows to determine the chemical composition and the nature of chemical bonding at an atomic scale. The technique is powerful but not straightforward to interpret. The inelastically scattered electrons travel through the hole of the ring-like ADF detector(s) and are used to record an electron energy loss spectrum (see figure 3.4).

A magnetic prism functions as an electron energy loss spectrometer. Put simply, a magnetic field perpendicular to the initial velocity of the electrons is applied. Assuming that the force of a particle is given by Newton's second law and it is equal to the centripetal force, this leads to

$$F = ma = \frac{mv^2}{R}, \tag{3.9}$$

where F is the force, m is the mass, a the acceleration, v the velocity and R the radius. Setting 3.9 equal with the Lorentz force given by equation 3.8, this yields

$$R = \frac{mv}{qB}. \tag{3.10}$$

under the assumption of orthogonal $\vec{v}$ and $\vec{B}$.

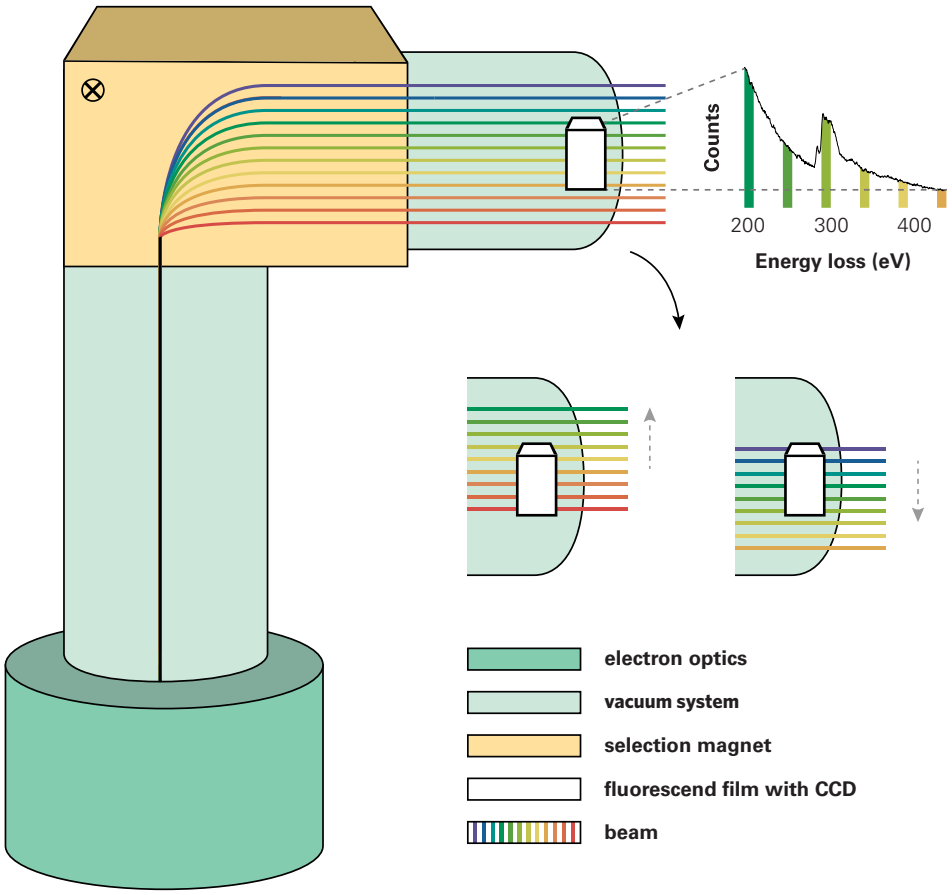

Figure 3.4: Schematic illustration of an electron energy loss spectrometer. The electrons are split by a magnetic field according to their energies with the colour spectrum representing the most energetic electrons (purple) to the least energetic ones (red). The beam can be moved up by decreasing the magnet's strength and thus looking at electrons with higher energy loss. Edges can be investigated in more detail by spreading the beam using the selection magnet in combination with electron optics. Thus, a certain part of the spectrum can be selected to hit a fluorescent film, which is filmed by a CCD camera. The spectrum on the top right shows the spectroscopic signal of graphene. Illustration: Christina Schmolmüller

The radius of the circle travelled by the electron depends on its velocity, which depends on its energy. The mass m, the charge q and the magnitude of the magnetic field B are the same for all electrons. This provides us with a filter where electrons of different energies hit a fluorescent film at the end of the prism at different positions creating a spectrum (see figure 3.4). The colour of the electrons correspond to different energies, which were chosen in analogy to the energies of light with purple corresponding to the highest and red corresponding to the lowest energies. The beam can be moved up and down and can be spread wider or thinner for selecting a specific part of the spectrum.

The interpretation of EELS can be quite difficult, but one can either use the EELS atlas [76] or simulate spectra for comparison. Different parts of the spectrum, and thus different excitations

(see section 3.1.3) can be selected and studied.

The spatial resolution of STEM EELS is limited by the probe size and the cross sections of the different processes. Compositional maps of the specimen are one of the very powerful tools provided, which are created by collecting a spectrum at each pixel and putting them together into an image. The intensities of the pixel then depend on the intensities of the energy loss in the selected range.

The electron gun has an energy spread of around 0.25 eV, which means that not all the electrons are emitted with the exact same energy. Also, there is a limit to the instrument's resolution given by the quality of the EELS set-up, which is 0.1 eV. Most of the electrons pass through the sample without interacting. These electrons make up the zero loss peak. Since there is a spread in the electron energies, this peak has a certain width, which introduces a background to the low loss area of an EELS spectrum. The spread of the zero loss peak for the used instrument is also larger than the energy of phonons which makes it impossible to resolve them.

3.1.10 Energy dispersive x-ray (EDX)

Another important spectroscopic method common for STEM and TEM is energy dispersive x-ray (EDX) spectroscopy. This method is based on electron ejection from a target atom due to a scattering event. The created hole is then filled with an electron from the Fermi level. The released energy is emitted via an x-ray photon with an energy that is characteristic for each element. This results in a spectrum of characteristic peaks on top of a background of Bremsstrahlung. The resulting spectrum is easier to analyse than EELS, but it has other disadvantages. For example, while in EELS almost all electrons are collected and contribute to the signal, in EDX only a fraction of the emitted photons can be collected since the detector only covers a small solid angle. Also, the process is not very efficient due to its small cross section.

3.1.11 Technical data

The instrument used for the present study is a NION UltraSTEM100 with a customized objective and sample stage connecting the instrument to an UHV system, which can be seen in the photograph of figure 3.2. The angular ranges of the detectors are $60 - 200$ mrad for MAADF and $80 - 300$ mrad for HAADF. EELS is done with a Gatan EEL spectrometer using a Andoer iXon Ultra 897 electron-multiplying charge-coupled device EMCCD camera. For tuning and fine adjustment of the electron beam, a BF CCD camera is used as ronchigram camera. The electron source is a 100 kV high-brightness cold field emission electron gun (CFEG). The microscope is equipped with a 3^{rd} generation C3/C5 aberration corrector with a minimum probe size of $1 - 1.3$ Å at $60 - 100$ kV. The base pressure at the gun and the sample is in the order of $10^{-11} - 10^{-10}$ mbar, which is around two orders of magnitude lower than other commercially available STEMS.

3.2 Ion implantation

3.2.1 Implantation set-up

To create the desired noble gas bubbles, FLG samples, introduced in chapter 2.4, were irradiated with different ions at different doses and energies in the Helsinki Accelerator Laboratory.[4] The device used for this was a linear accelerator called KIIA, a 500 kV Air Insulated Accelerator from High Voltage Engineering. Figure 3.5 schematizes the experimental set-up. More details on ion sources and accelerators in general are given in [77].

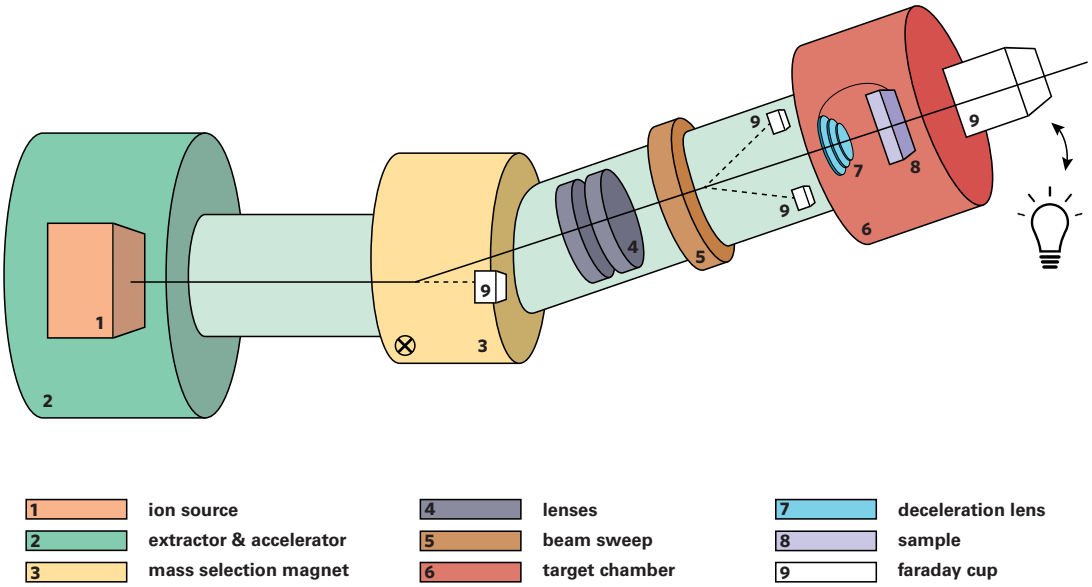

Figure 3.5: Schematic drawing of the accelerator set-up at the Helsinki Accelerator Laboratory. The beam travels from left to right. Illustration: Christina Schmolmüller

Two different ion sources (1) are used. There a plasma is created consisting of the desired species. Ions are extracted from the source by the extractor (2) and can be accelerated further in the accelerator tube to reach the desired energy. The first step is optimizing the ion source and extraction to create a stable beam. For that, the correct isotope has to be selected by the mass selection magnet (3) to hit the first Faraday cup (9) The underlying physical interaction of the selection magnet with the ions is the same as in an electron energy loss spectrometer. We assume all charged particles to have the same energy and charge, but their masses differ. By adapting the magnetic field, the desired charge to mass ration is selected by directing it through a slit behind the magnet while eliminating the undesired masses. The first Faraday cup is used for measuring the beam current while changing the ion source parameters. Once the beam current reaches a satisfying level and is stable, the selection magnet and other electromagnetic lenses in

[4] https://www.helsinki.fi/en/faculty-of-science/faculty/physics/research/materials-physics/accelerator-laboratory

the system (4) are used for directing the beam to the sample chamber. The beam then passes through a lens system, similar to the ones in electron microscopes for forming a probe, which is swept over the sample by the beam sweep (5) at 10 kHz horizontally and 1 kHz vertically. In the target chamber (6) a multi electrode ion beam deceleration lens (7) is used to slow down the ions so that they hit the sample (8) with the desired energy. Two Faraday cups, one behind the sample and a ring-like cup before the lens, can be used for aligning and focusing the beam. On top of that the Faraday cup behind the sample can be used for estimating the beam energy while the other can be used for measuring the beam current.

The energy of the primary beam in this system is determined by two voltages: the extraction voltage of the ion source, which can be chosen as 10, 20 or 30 kV, and the additional acceleration in the tube. Since the deceleration lens provides a maximum stopping voltage around 20 kV before becoming unstable and the desired energies of implantation were in the order of tens to hundreds of eV, we used the lowest possible beam energy by which the beam could still be focused with reasonable effort, being 20 kV. The Faraday cup behind the sample can be exchanged with a heating system to elevate the temperature of the samples during the irradiation.

3.2.2 Ion sources

Irradiation experiments were carried out with gases and metals. The ion source used for implanting gases is called SO-60-1 produced by High Voltage Engineering. It is a cold cathode penning source, which is explained in more detail in reference [77]. It is especially suited for the production of multiply charged ions from gases, though in our experiments only single charged ions were used. Creating a beam with this source is rather easy as there are only three parameters one can change, the leak to control the gas flow into the source, the magnet current to shape the plasma and the anode voltage.

The ion source used for metal implantation is called SO-55-1, also produced by High Voltage Engineering. It is a hot filament, hollow cathode source, also explained in [77]. It is able to ionize materials that have a vapour pressure of 10^{-2} mbar at temperatures of up to 1700 °C. It is suited for creating ion beams from different source materials and was used to create all beams except for the noble gas ones. Gaining an ion beam from this source is more difficult as there are more parameters. As for the gas source there is the leak controlling the gas inlet, the magnet current and the anode voltage, but there also the filament current and the oven current. Here, first an argon plasma needs to be produced which, together with the heating current, heats up the source material. The evaporating metal ions are then used for creating the beam. If the oven is not hot enough, the beam is very weak and may die due to lack of source material. If the oven is too hot, too much of the sample melts and can block the leak. The source has to be opened, disassembled and cleaned if that happens.

3.2.3 Handling the samples

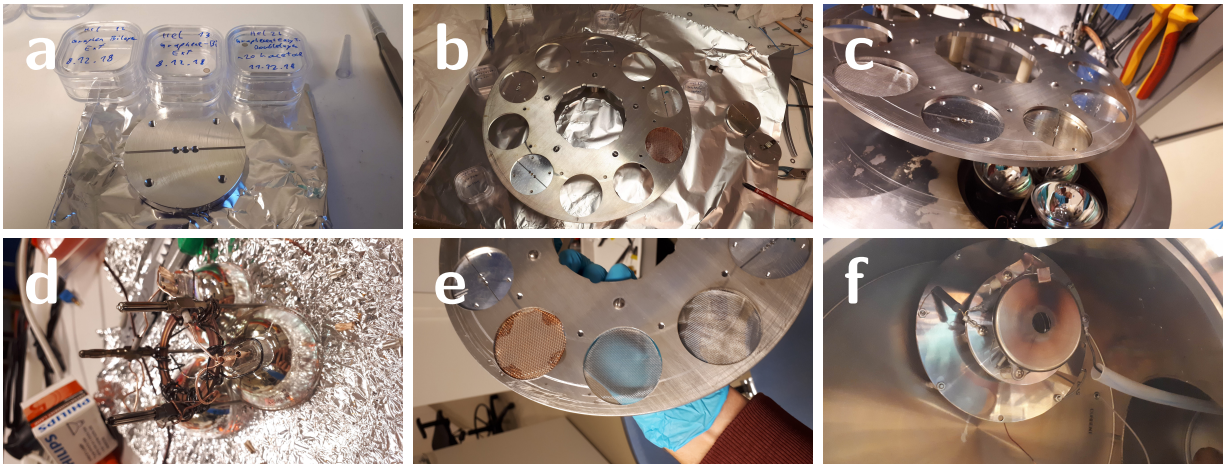

Figure 3.6: Photographs of different parts of the irradiation set-up. (a) Samples in trampoline boxes and sample holder plate. (b) Rotatable sample holder. Sample holder plates are put into the holes and fixed from the back. (c) Sample holder attached to the target chamber wall. Heating lamps in position for heating. (d) Heating lamps outside of the target chamber. (e) Different meshes for tests of the stopping voltage. (f) Deceleration lens mounted in the target chamber. Copper connector touches sample holder when the target chamber is closed.

Figure 3.6 shows the sample holder system and some important parts used in the implantation experiments. For the irradiation the samples are put into sample holder plates, (a). These plates are made of aluminium with a groove and three round indentations at the size of TEM sample holders. The grids are put into the indentations and a metal ring is placed on top of them to hold them in place. These plates are then mounted in the sample holder, (b). The sample holder is placed at the back end of the irradiation chamber, (c). It is rotatable to allow different implantation parameters using the same ion beam for different samples without opening the target chamber for a sample exchange. The holes can be covered with metal meshes for the calibration of the deceleration lens, (e). The heating system, figure 3.6 (d), can be mounted behind the sample holder, figure (c). When the target chamber is closed, the deceleration lens is in contact with the sample holder via a copper spring, figure (f).

3.2.4 Deceleration lens

Our collaborators in Helsinki developed a multi electrode ion beam deceleration lens. The lens is used to slow down ions and thus to lower the beam energy. Since an electrostatic potential is used to slow down the ions, the deceleration voltage can be calculated using

$$eU_{Decel} = E_{Beam} - E_{Desired}, \tag{3.11}$$

where U_{Decel} is the deceleration voltage, E_{Beam} is the energy of our beam and $E_{Desired}$ is the desired implantation energy.

The beam energy is determined using the Faraday cup behind the sample holder. The

beam travels through a hole in the sample holder covered by a mesh and the charge in the cup behind the mesh is measured while increasing the deceleration voltage. The deceleration voltage is increased until the current goes to zero. This bias is then called the stopping voltage and corresponds to the energy of the fastest ions in the beam. The lens is built in a way, that the ions have the set energy after they travelled through it. This only works if between the lens and the sample there is no electric field, thus the back of the lens is connected to the sample holder. If there is a hole in the sample holder the ions "see" the potential difference from the lens to the rest of the target chamber and the Faraday cup, thus the mesh is needed as an ion transparent equipotential "plate" for calibration. Figure 3.6 (e) shows three different meshes used to test whether the exact position or the making of the mesh had an influence on the stopping voltage. We did not find any differences of significance here.

If the potential of the lens is decreased by 10 V, the energy of fastest ions passing through of the lens is 10 eV. For deceleration voltages higher than 20 kV there were sparks from the lens to the the chamber leading to unstable experimental conditions. Also bad vacuum and the heating system led to more sparks.

Dose at the sample

Estimating the dose hitting the sample is done using a ring-like Faraday cup right before the deceleration lens, see figure 3.5. The beam is swept over the sample and the cups. The dose is then estimated using equation

$$T = \frac{D \cdot N \cdot q \cdot 1.602 \cdot 10^{-19}}{B \cdot 10^{-6}}, \tag{3.12}$$

with D being the required dose in ions/cm^2, q being the charge of the particles, N being the area of the Faraday cup in cm^2 and B the selected range of the current integrator in μA. The area of the Faraday cup is $N = 1.7$ cm^2 and the charge of the particles was always $q = 1$. The desired dose was often chosen as $D = 10^{15}\ \frac{ions}{\mathrm{cm}^2}$, which corresponds to $10\ \frac{ions}{\mathrm{nm}^2}$, compared to $\approx 38\ \frac{\mathrm{atoms}}{\mathrm{nm}^2}$ in a graphene monolayer.

Investigating the beam spread

Estimating the dose with a detector before the deceleration lens is problematic as can be understood when looking at figure 3.7. It shows a Gaussian beam profile with an FWHM of 50 eV centred at 20 keV. If the desired ion energy is very low, only a small fraction of the ions actually reach the sample due to that spread. Thus the dose measured before the deceleration is not the same as the dose hitting the sample.

The beam shape and spread are unknown. Attempting to measure the beam spread, the current in the Faraday cup behind the mesh was measured as a function of the deceleration voltage, see figure 3.8. The curve should correspond to the integral of the ion beam profile,

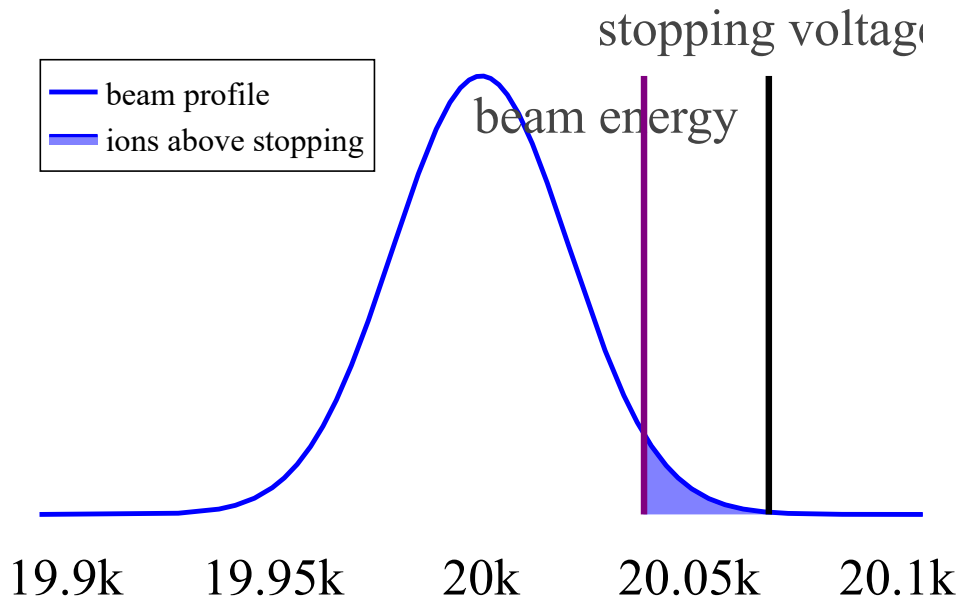

Figure 3.7: Illustration of the beam profile with a stopping voltage set in black and the beam energy set in purple. The marked area corresponds to the ions which reach the sample whereas the whole curve corresponds to the measured dose. The beam has an FWHM of 50 eV, the stopping voltage is located where the beam has an energy of 1/200 of the maximum of the profile and the beam energy is set at 20 eV.

however, since the ions are accelerated by the electric field between the back side of the sample holder and the Faraday cup, there are also other effects contributing to the current. The ions get accelerated to an energy of roughly 20 keV, the potential difference, before hitting the metal surface of the Faraday cup. Thus secondary electrons are emitted, which get accelerated towards the sample holder due to the potential there. These electrons contribute to the current measured by the cup. As can be seen the current keeps rising for 150 eV when measuring the profile with tin ions and 220 eV and 267 eV when measuring the profile with nickel ions. It is not possible to draw any conclusions from this apart from that there is an energy spread and it is probably somewhere between 50 and 200 eV. When measuring the current for the first time with nickel the beam was very weak and also the stopping voltage was strangely off. This will be elaborated in further detail in the discussion.

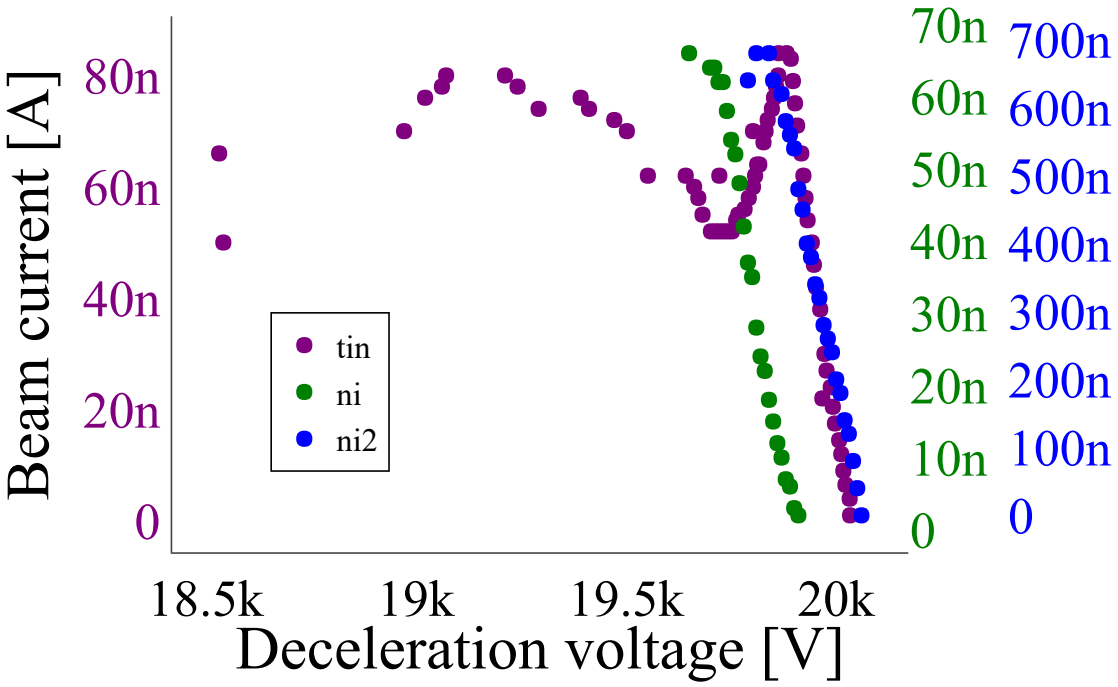

Figure 3.8: Current measured by the Faraday cup behind the deceleration lens for different deceleration voltages.

3.2.5 Heating system

Contamination on samples is a serious problem in high resolution microscopy of 2D materials. Tripathi et. al. investigated the effect of different treatments and found that heating in vacuum is a reliable method for cleaning graphene [48]. Thus a heating system was developed for cleaning samples right before and during the irradiation process.

Two main approaches were tested. Heating by a hot filament through direct contact or radiative heating with lamps. The first approach was quickly discarded since several wires would need to be attached to every sample holding plate and the filament would need to be separated by a thermally conductive electrical insulator. Lamps were easier to install into the set-up with the disadvantage that reaching high temperatures requires more power due to losses and is slower.

The finalised system is shown in figure 3.6 (c) and (d). It is positioned behind the sample holder and has a fairly simple design. Three 150 W halogen lamps illuminate the sample with white light. As indicated in figure 3.5, the Faraday cup behind the samples can be exchanged with an electrical feedthrough for the lamps.

Developing, testing and improving the heating system to be able to clean samples while doing implantation experiments was time-consuming. The challenge was the combination of a rotatable sample holder, the high potential at the sample holder and the limited space due to the vacuum chamber.

Heating capacity

The goal was to reach temperatures of up to 500-600 °C. Restricting factors were the time needed for heating up the samples as well as the vacuum level while the heating was on and compatibility with the deceleration lens. Figure 3.9 shows the temperature at the sample for different heating cycles, with one and three lamps. We were able to reach almost 400 °C after approximately 90 minutes of heating. The red dots mark the time when the heating was either turned off or down.

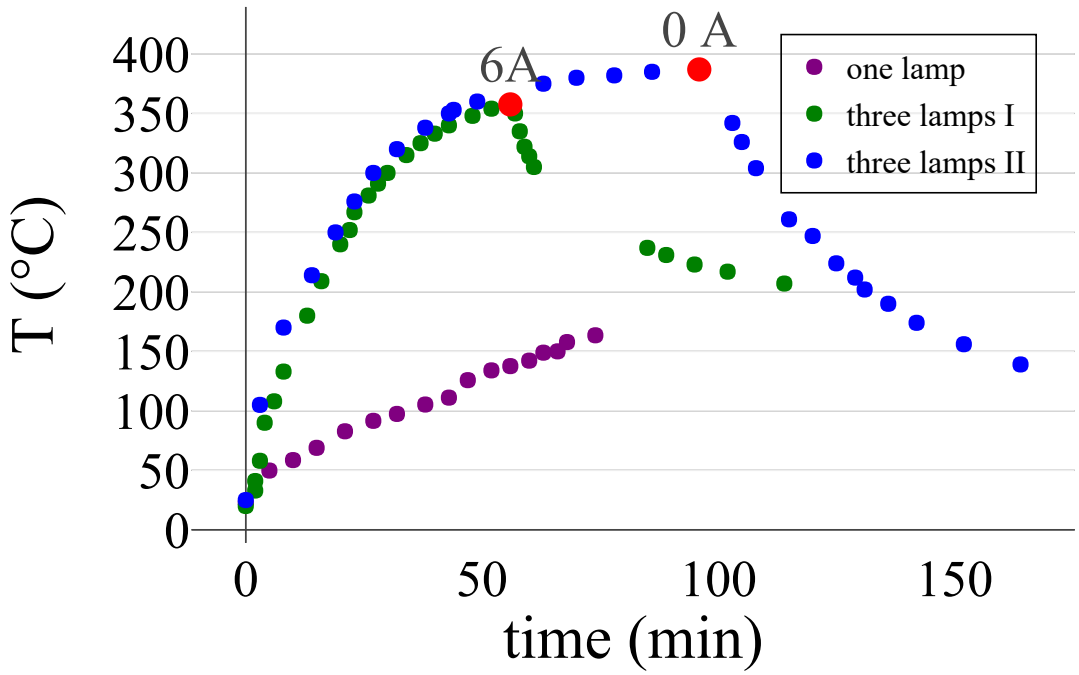

Figure 3.9: Temperature as a function of time for one lamp in purple, and three lamps in green and blue. The heating system was run at full power (10 A, 520 W) for a given time, indicated by the red dots. The heating current was set to 6 A for the green curve and turned off for the blue curve.

3.2.6 Summary

Exfoliated FLG samples on TEM grids were transported to Helsinki and irradiated with different ions using the accelerator. The energy was set using a 20 kV beam, decreasing the energy with the deceleration lens. All samples were heated before the irradiation, some in vacuum, others simply on a hot plate in air. After the irradiation the samples were taken to Vienna for analysis.

3.3 Image analysis

Image analysis was done in a Jupyter Notebook using self-written Python[5] code. The latest version of the notebook is attached in the appendix. It was developed while doing the analysis and evolved into a quite versatile tool for plotting images as well as auto scaling, filtering, extracting line profiles and analysing these to study characteristic distances in the system. This way of doing the analysis was chosen to increase the reproducibility of the work as well as the possibility of automating parts of the data analysis.

3.3.1 Semi-automatic scaling

When data is collected with an instrument one has to pay attention that the instrument is calibrated correctly. The same is, of course, true for images taken with microscopes. For equipment updated and modified frequently, ensuring correct calibration is important. Therefore, an automated method for image scale calibration during post processing was developed.

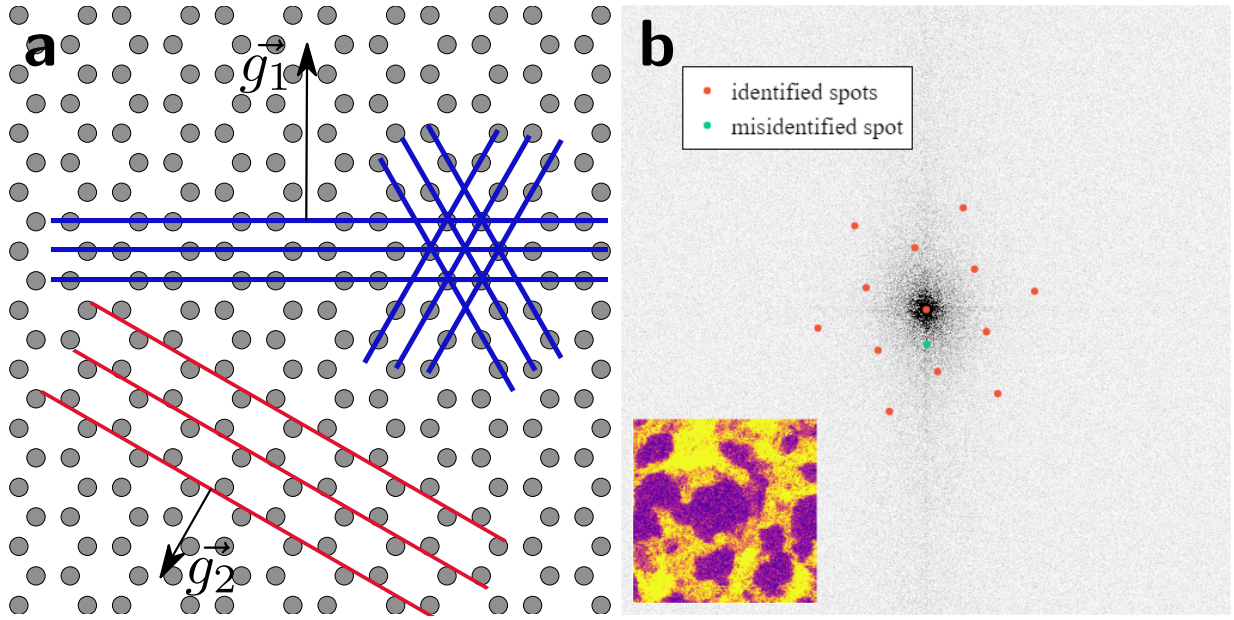

Figure 3.10: (a) Illustration of the graphene lattice drawn using the *atomic simulation environment package* in Python [78]. Atomic planes are marked in red and blue. Periodicity vectors perpendicular to the planes with the length proportional to the frequency are shown. (b) Fast Fourier transform with the, by the algorithm detected, dots representing the frequencies in the image marked in red. One extra spot was misidentified here. The inset is the original image, also shown in figure 3.11 (d)-(f)

Reciprocal space is used for scaling the images. The Fourier transform (FT) is a mathematical operation which associates a function or signal to its reciprocal counterpart, for example time is associated with frequency. It can also be used for transforming a function in space into its spatial frequencies, as done here. The FT of a microscopy image is similar to a diffraction pattern and contains similar information. Figure 3.10 (a) shows a schematic illustration of the graphene

[5] https://www.python.org/

lattice. The atomic planes can be represented by vectors $\vec{g}_1$ and $\vec{g}_2$, which are orthogonal to the planes pointing in the direction of periodicity, and the length inversely proportional to the distance between the planes, the frequency.

The set of planes shown in blue goes along the armchair direction. The spacing between the planes is given by

$$d_1 = \frac{|\vec{a}|}{2} \propto |\vec{g}_1|, \tag{3.13}$$

with d_1 being the spacing between the planes, $\vec{a}$ being a lattice vector of graphene, and g_1 being the frequency vector. The planes drawn in red go along the zigzag direction in graphene and the distance between them is given by

$$d_2 = |\vec{a}| \cdot \sin(60^\circ) \propto |\vec{g}_2|, \tag{3.14}$$

which results in a lower frequency and thus a shorter vector $\vec{g_2}$.

The FT takes the frequency components and denotes every frequency with a discrete point. A complex function varying in space is decomposed into its harmonic components. Every set of planes results in two symmetric dots around the centre since $\vec{g}$ can point in both directions. Every plane has three equivalent directions resulting in six spots per spatial frequency. Figure 3.10 (b) shows the FT of an microscopy image of a FLG lattice with peaks, identified by a peak-finder function, marked in red. Every point is the end of one frequency vector from the centre. The outer spots represent the higher frequency $\vec{g}_1$, the inner spots the lower frequency $\vec{g}_2$. In the image one peak is misidentified as a diffraction spot.

To scale images in real space the relationship between real and reciprocal distances needs to be understood. A distance of x pixels in an array of $L \times L$ pixels in real space is transformed to a reciprocal length $\frac{L}{x}$. This can be understood by thinking about two images of the same structure but with different fields of views. In a larger field of view the same features have a higher frequency and thus the spots in reciprocal space are further away from the centre. Thus the natural distance in the FT is calculated by taking the size of an image and dividing it by the distance from the centre, r. Since the length of the lattice constant $\vec{a}$ is known in real space we can scale our images by measuring the distance in reciprocal space.

The fast Fourier transform (FFT), an efficient implementation of a discrete Fourier transform, is used to transform the microscopy images. A peak finder is used for finding spots and then the distance, r from the spots to the centre is calculated. The value of $\frac{L}{r}$, in pixels is then set equal to either d_1 or d_2. The quality of some of the images was too poor to be able to detect the diffraction spots in the FFT. For these images no scale bar was added to the image but the field of view was stated in the caption of the image to indicate that the distances were not evaluated using this method.

3.3.2 Plotting

For plotting images, the Heatmap function of the Python library Plotly[6] was used. The lookup table Plasma is used to enhance the contrast. This makes it easier to recognize features in the images. The contrast can be adjusted by setting a minimum and a maximum value and by plotting all values in between on a linear scale. For FFTs, a linear scale was chosen with approximately $0.3 - 0.5$ % as the maximum.

3.3.3 Double Gaussian filter

Aberrations cause an extended tail in the electron beam shape, which can cause nearest-neighbour atoms to contribute to the intensities of the scanned atomic column and thus make the interpretation of images more difficult. These probe tails can be removed using a double Gaussian filter, which is particularly useful when measuring and comparing intensities [74]. The filter is implemented by multiplying the FFT with two Gaussian functions and then using the back-transformation. Basically, some spatial frequencies are enhanced in the image. Multiplying with a positive Gaussian smoothens the intensity variation between pixels by cutting off spatial frequencies beyond those that are actually transferred by the microscope. This was implemented by choosing the radius of the positive Gaussian as 1.3 times the distance to the outer spot. Multiplying with a negative Gaussian adds a negative skirt to the image of each atom. This is done to decrease the extended probe tail at the location of the nearest neighbours. The radius of the negative Gaussian was chosen as 0.6 times the distance to the inner diffraction spots. Since the distance between krypton atoms is much higher than that between carbon atoms in graphene the filter would remove information about the krypton structures since the frequency is a lot lower. Thus the radius of the negative Gaussian was chosen as 0.15 time the distance to the inner graphene spot whenever there was also krypton in the images. Figure 3.11 shows images plotted with varying contrast, filtered and unfiltered. In (g) it also shows how the double Gaussian filter changes the FFT when it is applied. On the left the unfiltered image is visible, in the middle the double Gaussian and on the right the FFT multiplied by the filter can be seen.

[6] `https://plotly.com/python/`

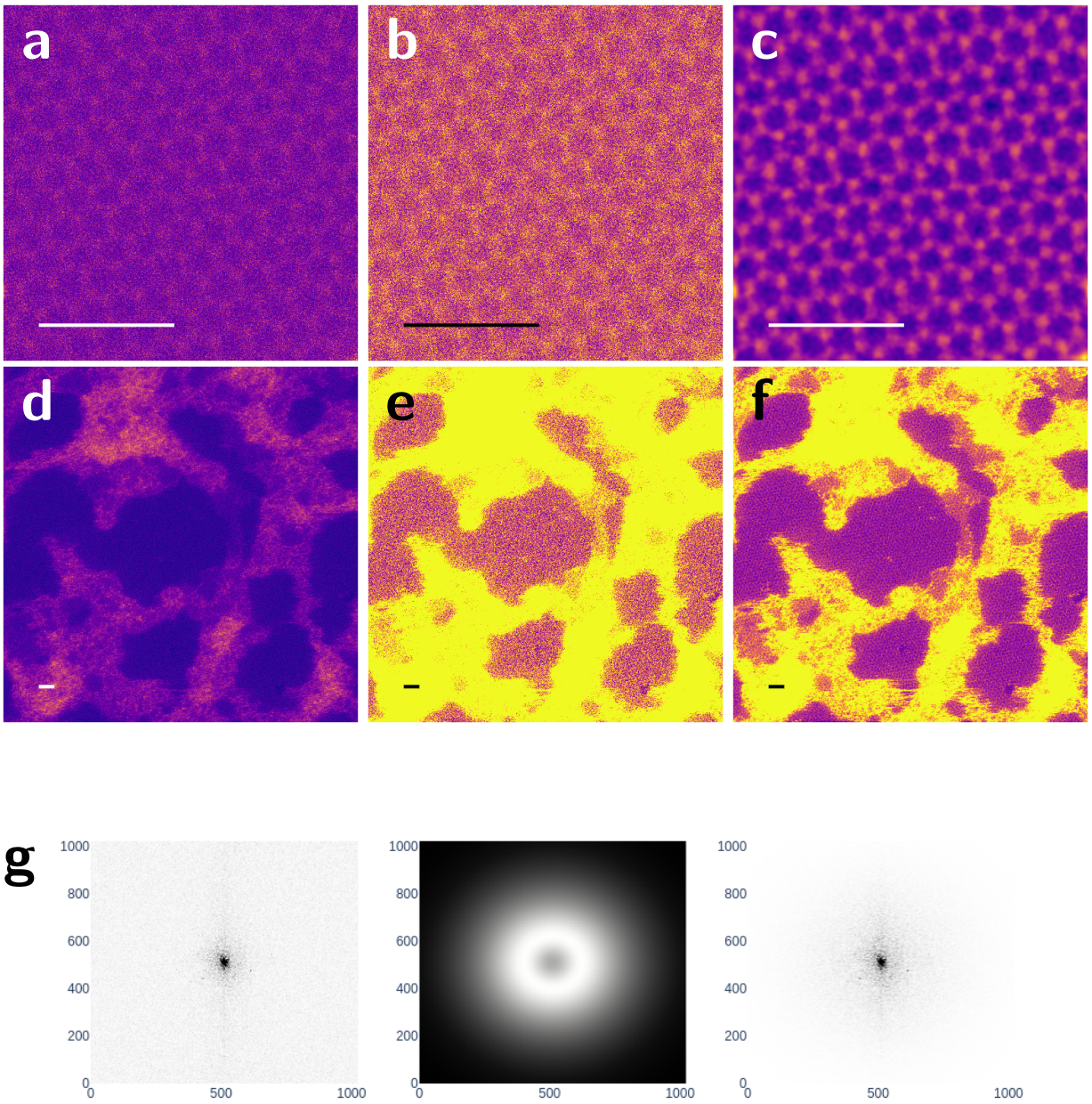

Figure 3.11: (a) & (b) STEM MAADF image of a graphene monolayer plotted with different contrast settings. (c) Double Gaussian filtered image (a) & (b). Scale bar: 1 nm. (d) & (e) Larger field of view image at the same position as (a)-(c) plotted with different contrast settings. (f) Double Gaussian filtered image (d) & (e). Scale bar: 1 nm. (g) Unfiltered FFT on the left, the double Gaussian filter in the middle and the filtered FFT, which will then back-transformed, on the right. The colour scheme in the FFT is linear, white to black, from 0 to 0.5 % of the maximum intensity with all values above displayed in black. The filter applied is shown in the middle with inverted contrast (black corresponds to low, white to high values). The radius of the Gaussians depends on the distance between the spots and the centre.

3.3.4 Identification of characteristic distances

As will be seen in the results, two characteristic distances in the images were of interest to us. The interatomic spacing and the distance between clusters as there appeared to be a systematic

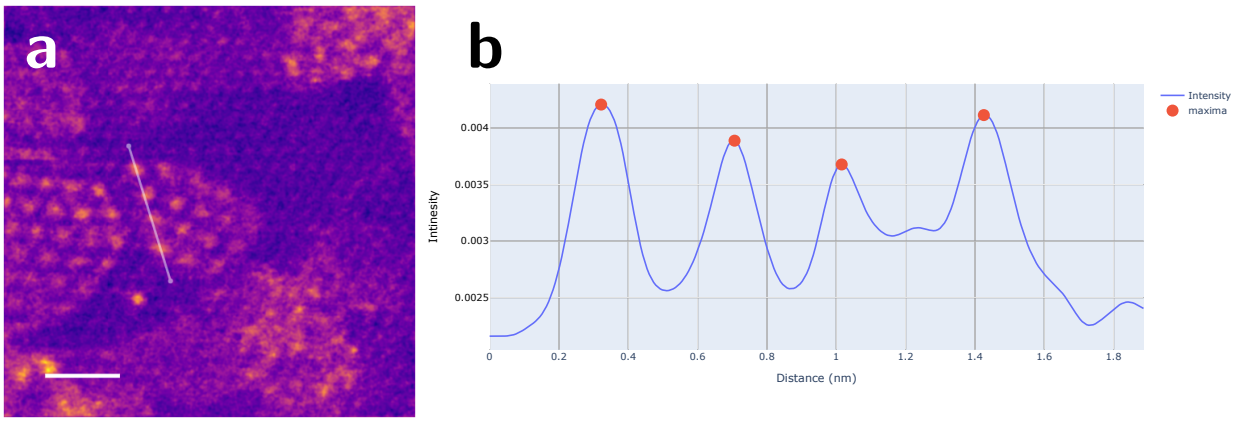

Figure 3.12: (a) & (c) STEM MAADF images of FLG encapsulated krypton structures. (b) line profile along the line in (a). & (d) Intensity along line profiles drawn in (a) & (c)

behaviour. In order to identify these characteristic distances a function is used which extracts intensity values along a line between a starting and an end point, i.e. a line profile. The width of the profile is set by blurring the image with a Gaussian filter, which smoothens the image. The data is extracted with the function map_coordinates from the ndimage package in scipy [79]. Figure 3.12 (a) & (b) show a Kr cluster with a line and the intensity along that line. The interatomic distance is determined by finding the peaks along the line profile and calculating the distance between these peaks, figure 3.12 (b). As will also be discussed in the results and can be seen in figure 3.12 (a), some atoms are distinct bright spots, whereas other atoms appear blurry and can not be distinguished. Thus it is hard to estimate where the edge of a crystal is sometimes.

3.4 Image simulation

Image simulation is done, to understand microscopy images better. The main goals are understanding the detailed structure in the image and how they are formed. Using computational tools developed in our group called abTEM, previously called PyQSTEM [80], it is easy to build structures using the *atomic simulation environment* [78] and simulate STEM images. First ab initio electrostatic potentials are generated, then the multislice method is used to simulate microscopy images using this potential. The specimen is divided into thin slices which only provide minor perturbation on the forward motion of the electron. The influence of each slice is approximated as a simple phase shift of the wave function which is then propagated between the slices. For more details on the FFT based multislice method see reference [81]. Simulated images can be compared to the images taken with the microscope. Image simulation results are shown in chapter 4.4.

3.5 Implantation simulations

In order to understand the experimental results better the implantation depth of krypton in graphite was calculated using the SRIM[7] (Stopping and Range of Ions in Matter) software. First the module "Stopping / Range Tables" was used to calculate tables of the ranges of ions in matter. They are calculated using the code PRAL (Projection RAnge ALgorithm) [82, 83]. Using the transport equation approach the ranges of atoms in a homogeneous target of infinite thickness consisting of (complex) compounds can be calculated. It is a very fast method which calculates ion ranges over a large band of energies with quite high accuracy (ca. 5% discrepancy to TRIM methods). Tables of the projected ranges of Kr in graphite were calculated and are plotted in figure 4.21 in the results.

As these calculations are not very accurate Monte Carlo (MC) simulations of the implantation experiments were carried out as well using the TRIM (the Transport of Ions in Matter) module. Monte Carlo methods use random numbers to solve numerical and non numerical problems. For the simulations in SRIM the binary collisions approximation describes the interaction between the impinging ion and the target. Thus, depending on the density of the target material, random binary collisions are used to simulate the implantation process. With the help of this software, various aspects of ion irradiation can be calculated. Ref. [84] explains the software in great detail. For the purpose of this work, it was used to calculate the energy loss of noble gas ions in graphite. In chapter 4.5 the results of the simulation are shown.

[7] http://www.srim.org/

Chapter 4

Results

4.1 Ion irradiation experiments

The implantation experiments took place in the Accelerator Laboratory of the University of Helsinki, Finland. More than 100 samples were irradiated in three rounds with ten different ion species. The goal was to implant atoms into the van der Waals gap between FLG layers as well as into the lattices of monolayers and FLG samples and to study the emerging patterns. Here only the results of inert gas irradiation will be shown as this is the topic of this master's thesis, and the author was mainly responsible fore these experiments.

4.1.1 First set of irradiation experiments (IRR1)

During the first set of irradiation experiments (IRR1, Helsinki, December 2018/January 2019), 30 samples were irradiated with argon (Ar^+) and silver (Ag^+) ions at energies ranging from $50 - 200$ eV and doses ranging from $10^{14} - 10^{15} \frac{\text{ions}}{\text{cm}^2}$. The parameters used for the different samples are listed in table 4.1.

Argon (Ar, 18, 40 u)

During the irradiation experiments with argon, the vacuum level in the target chamber was kept in the range of $10^{-6} - 10^{-5}$ mbar. The stopping voltage for the Ar implantation was 19.908 kV. The samples were baked at 140 °C for 15 hours before entering the vacuum chamber to minimize the contamination. Whey were put into the target chamber while still being warm to prevent water condensation. Unfortunately the stopping voltage was calibrated without a net, thus it was too high and no ions reached the sample.

Table 4.1: **Irradiation parameters of IRR1**

Batch	Samples			Energy [eV]	Dose [$\frac{\text{ions}}{\text{cm}^2}$]	Element
A	Hel 18	Hel 19	Hel 29 CVD 2	not irradiated		
B	Hel 16	Hel 17*	Hel 28 CVD 2	50	10^{15}	Ar
C	Hel 14	Hel 15	Hel 27 CVD 2	100	10^{14}	Ar
D	Hel 12	Hel 13	Hel 26 CVD 2	100	10^{15}	Ar
E	Hel 10	Hel 11	Hel 25 CVD 2	200	10^{14}	Ar
F	Hel 08	Hel 09	Hel 24 CVD 2	40	10^{14}	Ag
G	Hel 06	Hel 07	Hel 23 CVD 2	60	10^{13}	Ag
H	2018-10-18#5.2	2018-10-19#03	Hel 22 CVD 2	60	10^{14}	Ag
I	2018-10-19#13	2018-10-19#6	Hel 21 CVD 2	60	10^{15}	Ag
J	Hel 02	Hel 04	Hel 30 CVD 2	100	10^{14}	Ag

* This sample was lost

Silver (Ag, 47, 108 u)

During the irradiation experiments with silver, the stopping voltage was 20.172 kV. The vacuum level was not recorded.

4.1.2 Second set of irradiation experiments (IRR2)

During the second set of irradiation experiments (IRR2, Helsinki, April 2019) 41 samples were irradiated with argon (Ar^+), krypton (Kr^+), platinum (Pt^+) and silver (Ag^+) at energies ranging from $30 - 300$ eV and doses ranging from $10^{14} - 10^{15} \frac{\text{ions}}{\text{cm}^2}$. The parameters used for the different samples are listed in table 4.2.

Argon (Ar, 18, 40 u)

The vacuum level in the target chamber was $1.2 \cdot 10^{-7}$ mbar before and $3.7 \cdot 10^{-7}$ mbar after the irradiation. When the beam was on, it was most likely an order of magnitude higher. The stopping voltage for the Ar implantation was 19.758 kV. The samples were baked at 140 °C for 50 minutes before being put into the irradiation chamber.

Krypton (Kr, 36, 84 u)

The vacuum level in the target chamber was $1.6 \cdot 10^{-6}$ mbar at the start of the irradiation. The stopping voltage for the Kr implantation was 20.016 kV. The samples were baked at 140 °C for approximately 1 hour before being put into the irradiation chamber. The pressure during the irradiation was roughly $1.6 \cdot 10^{-6}$ mbar.

Table 4.2: **Irradiation parameters of IRR2**

Batch	Samples & thickness (# layers)			Energy [eV]	Dose [$\frac{\text{ions}}{\text{cm}^2}$]	Element
1	Hel 32 2+3	Hel 31 1		150	10^{15}	Ar
2	Hel 34 2+3	Hel 36 1+2+3	Hel 57 SiN 2	70	10^{15}	Ar
3	Hel 43 3+4	Hel 40 2+3+4	Hel 53 SiN 2	30	10^{15}	Ar
4	Hel 38 4+1	Hel 46 2+3+4?+6	Hel 54 SiN 2	300	10^{15}	Ar
5	Hel 42 2+3	Hel 49 2	Hel 50 1	50	10^{15}	Kr
6	Hel 41 3+other	Hel 37 2+4+5+6	Hel 55 SiN 2	100	10^{15}	Kr
7	Hel 34 3	Hel 48 2+4	Hel 54 SiN 2	300	10^{15}	Kr
8	CVD_1_Pt_1 1			40	10^{14}	Pt
9	CVD_1_Pt_2 1	Hel 60 CVD 2		60	10^{14}	Pt
10	Hel 33 2-3 exf	Hel 62 CVD 2		80	10^{14}	Pt
11	Hel 66 CVD 2			100	10^{14}	Pt
12	Hel 47 2-3	Hel 64 CVD 2		150	10^{14}	Pt
13	Hel 59 CVD 2			250	10^{14}	Pt
14	Hel 51 1-5	Hel 58 CVD 2		300	10^{14}	Pt
15	2061 CVD 1			30	10^{14}	Ag
16	2060 CVD 1			40	10^{14}	Ag
17	Hel 45 1+2	2062 CVD 1		50	10^{14}	Ag
18	Hel 52 1+2	Hel 61 CVD 2		150	10^{14}	Ag
19	Hel 44 2+3	Hel 63 CVD 2		200	10^{14}	Ag
20	Hel 39 2+3+4	Hel 65 CVD 2		250	10^{14}	Ag

Platinum (Pt, 78, 195 u)

The vacuum level in the target chamber was $5.6 \cdot 10^{-8}$ mbar before the irradiation, which must have worsened once the beam was on by at least one order of magnitude. The stopping voltage for the Pt implantation was 20.168 kV. The samples were baked at 140 °C for about 90 minutes before being put into the irradiation chamber. Platinum has five stable isotopes, four of which were used for the implantation, ^{194}Pt-^{198}Pt. Two tungsten filaments were used in the ion source. Due to the small relative mass difference between Pt (194 u) and W (184 u) coimplantation is possible. It was als noted, that the Faraday cups could have been hit by secondary e^-, which might cause the actual dose to be higher. After the irradiation, the grids appeared to have been charged.

Silver (Ag, 47, 108 u)

The vacuum level in the target chamber was $1.1 \cdot 10^{-6}$ mbar at the start of the irradiation. The stopping voltage for the Ag implantation was 20.172 kV. The samples were baked at 140 °C for roughly 45 minutes before being put into the irradiation chamber.

4.1.3 Third set of irradiation experiments (IRR3)

During the third set of irradiation experiments (IRR3, Helsinki, August & September 2019) 41 samples were irradiated with noble gases (xenon, krypton, argon and neon) and metals (aluminium, manganese, nickel and tin) at energies ranging from 30 eV to 20 keV and doses ranging from $10^{14} - 10^{15} \frac{\text{ions}}{\text{cm}^2}$. The parameters used for the different samples are listed in table 4.3. Here, not only FLG but also monolayer graphene and MoS_2 monolayers were irradiated. For cleaning the samples the heating system described in the methods was used.

General remark

The rotatable sample holder system was a bit off axis and tilted by a few degrees and was fixed after the tin irradiation. This has to be taken into account when investigating the samples.

For argon the variation of the stopping voltage was tested for three different meshes at slightly varying positions of the meshes. Also the current was measured with the meshes being slightly off axis. The maximum variation in the deceleration voltage that could be detected was 5 V implying that the irradiation set-up is stable and robust with respect to small changes that could happen during normal operation.

The temperatures are not given as we could not measure them in the newly developed heating set-up. The temperatures of the samples can be estimated using the curves im figure 3.9 on page 40 in chapter 3.2.5. The general rule here is: the longer the sample was baked, the hotter it was during the irradiation.

Krypton (Kr, 36, 84 u)

The samples were baked for two hours in vacuum, then the chamber was vented because the deceleration lens could not hold a bias of 20 kV. A cable coming from another feedthrough was touching the sample holder. After fixing that, the lens was able to hold the required voltage. The stopping voltage for this irradiation was about 20.020 kV. The heating system was adjusted in such a way, that sample Hel 85 would be heated the most. The samples were put into the irradiation chamber and baked with the maximum power for 30 minutes. After that the samples were heated with 6 A (ca. 150 W), for 25 minutes. The samples were irradiated while the heating was running with 4 A heating current (ca. 100 W). The pressure during the irradiation went from $3.3 \cdot 10^{-6}$ mbar down to $1.8 \cdot 10^{-6}$ mbar for the last irradiation. There were a few sparks in the chamber during the irradiation.

Aluminium (Al, 13, 27 u)

The day before the irradiation, the samples were heated for several hours in vacuum at maximum power, 520 W heating, and at lower powers. The sample cooled down completely and, right

Table 4.3: **Irradiation parameters of IRR3**

Batch	Samples + thickness (# layers)		Energy [eV]	Dose [$\frac{\text{ions}}{\text{cm}^2}$]	Element
Kr 1	Hel 76 2+3+4		70	$1 \cdot 10^{15}$	Kr
Kr 2	Hel 75 1+2+3+4		80	$1 \cdot 10^{15}$	Kr
Kr 3	Hel 79 3+4+thicker		90	$1 \cdot 10^{15}$	Kr
Kr 4	Hel 85 1+2+3+4+5,+,...		100	$1 \cdot 10^{15}$	Kr
Al 1	Hel_Al_#1 CVD 1		20	$5 \cdot 10^{14}$	Al
Al 2	Hel_Al_#2 CVD 1	Hel_Al_#3 CVD 1	30	$5 \cdot 10^{14}$	Al
Al 3	Hel_Al_#4 CVD 1		40	$5 \cdot 10^{14}$	Al
Mn 1	Hel_Mn_#1 CVD 1		20	$5 \cdot 10^{14}$	Mn
Mn 2	Hel_Mn_#2 CVD 1		25	$5 \cdot 10^{14}$	Mn
Mn 3	Hel_Mn_#3 CVD 1		25	$5 \cdot 10^{14}$	Mn
Mn 4	Hel_Mn_#4 CVD 1		30	$5 \cdot 10^{14}$	Mn
Ni 1	Hel_Ni_#1 CVD 1		20	$1 \cdot 10^{15}$	Ni
Ni 2	Hel_Ni_#2 CVD 1		30	$1 \cdot 10^{15}$	Ni
Ni 3	Hel_Ni_#3 CVD 1		35	$1 \cdot 10^{15}$	Ni
Ni 4	Hel_Ni_#4 CVD 1		25	$1 \cdot 10^{15}$	Ni
Sn 1	Hel_Sn_#1 CVD 1		15	$5 \cdot 10^{14}$	Sn
Sn 2	Hel_Sn_#2 CVD 1		20	$5 \cdot 10^{14}$	Sn
Sn 3	Hel_Sn_#3 CVD 1		25	$5 \cdot 10^{14}$	Sn
Sn 4	Hel_Sn_#4 CVD 1		30	$5 \cdot 10^{14}$	Sn
Ar 1	Hel 19 2	Hel 83 1+3	130	$1 \cdot 10^{15}$	Ar
Ar 2	Hel 77 2+3+4		160	$1 \cdot 10^{15}$	Ar
Ar 3	Hel 86 2+3+4+5		190	$1 \cdot 10^{15}$	Ar
Ar 4	Hel 87 1+2+3+4+5		220	$1 \cdot 10^{15}$	Ar
Xe 1	Hel 18 1+4	Hel 71 2	45	$1 \cdot 10^{15}$	Xe
Xe 2	Hel 88 2+3+4+5		55	$1 \cdot 10^{15}$	Xe
Xe 3	Hel 84 1+2+3+4+thicker		65	$1 \cdot 10^{15}$	Xe
Xe 4	Hel 90 MoS_2		100	$1 \cdot 10^{14}$	Xe
Xe 5	Hel 91 MoS_2		500	$1 \cdot 10^{14}$	Xe
Xe 6	Hel 92 MoS_2		1 k	$1 \cdot 10^{14}$	Xe
Xe 7	Hel 93 MoS_2		5 k	$1 \cdot 10^{14}$	Xe
Xe 8	Hel 94 MoS_2		10 k	$1 \cdot 10^{14}$	Xe
Xe 9	Hel 95 MoS_2		20 k	$1 \cdot 10^{14}$	Xe
Ne 1	Hel 74 2	Hel 80 3-5+thick	320	$1 \cdot 10^{14}$	Ne
Ne 2	Hel 89 1+2+3+4?		270	$1 \cdot 10^{14}$	Ne
Ne 3	Hel 78 1+2?+3	Hel 97 CVD 2	220	$1 \cdot 10^{14}$	Ne
Ne 4	Hel 98 CVD 2		170	$1 \cdot 10^{14}$	Ne

before the irradiation, heated again with 7.5 A, 240 W. The heating was turned on with this power during the implantation. The stopping voltage was 20.020 kV. The implantation took about one minute per sample. The dose is not exactly known due to sparks from the lens, which is connected to the Faraday cup, but it should be $2 - 5 \cdot 10^{14}$ $\frac{\text{ions}}{\text{cm}^2}$. The pressure during the irradiation varied from $1.8 - 1.5 \cdot 10^{-6}$ mbar.

Manganese (Mn, 25, 55 u)

The stopping voltage for manganese was 18.910 kV. The sample was heated for 1.25 hours at full power (520 W) and then 1.5 hours with at lower power (7 A, 200 W). Then, one a filament of a heating lamp broke and the irradiation took place half an hour later. The irradiation took around 16 minutes for each sample. Hel_Mn_#3 was probably irradiated twice, once with the parameters of Hel_Mn_#3 and once with the parameters of Hel_Mn_#4, that may not have been irradiated due to the fact that the sample holder was not fixed to the wall properly resulting in an ill-positioned sample. The pressure during the irradiation varied between $4.3 - 9 \cdot 10^{-7}$ mbar. After the irradiation, the sample holder was still at an elevated temperature, around 50 °C.

Nickel (Ni, 28, 59 u)

The sample was heated with 520 W for circa 1 hour and then cooled down. The following day it was heated for roughly 3 hours with a power of 115 W. Heating was turned off when starting the irradiation. During the irradiation of Hel_Ni_#3 the beam was lost after 4 % of the desired dose. It was regained afterwards but the irradiation took 54 minutes, in contrast to the first one, which took 23 minutes. During the third irradiation, there was a spark at approximately half the desired dose after which the current measurement could not be trusted anymore. The irradiation time up to that point was used to roughly estimate when the desired dose was reached. The stopping voltage was found to be 20.023 kV. The pressure during the irradiation was in the order of $2 \cdot 10^{-6}$ mbar.

Tin (Sn, 50, 119 u)

The stopping voltage was found to be 20.018 kV. Sample 3 fell out of the mounting system but was found again. The samples were heated three times with 520 W for more than half an hour and were exposed to air between. After the first time, the sample holder was unable to rotate. After the second time, the heating system broke, which meant that the desired temperature could not be reached. After the third heating cycle at 520 W with 30 minutes, the irradiation started. The beam consisted of three peaks, which means that three different isotopes were used for implantation. The abundance ratio was not as expected and also the current of the selection magnet was off, thus we can not be certain about the implanted species being the desired one. The pressure during the irradiation ranged from $1.1 - 1.7 \cdot 10^{-6}$ mbar.

Argon (Ar, 18, 40 u)

The samples were heated for one hour with a power of 520 W after which the irradiation chamber was pumped over night. The following day the samples were heated again for half an hour at 520 W after which the irradiation was carried out. The pressure ranged from $3.5 - 4 \cdot 10^{-7}$ mbar.

The stopping voltage was estimated to be 20.013 kV. The current during the irradiation was 1.8μA, the irradiation took approximately 3 minutes for each set of samples.

Xenon (Xe, 54, 131 u)

The stopping voltage for Xe was 20.008 kV. The beam current measured with the Faraday cup before the deceleration lens varied for different stopping voltages. For a stopping voltage of 18 kV the current was 0.6 μA, whereas it was 0.94 μA at 20 kV deceleration. Thus we assume that the dose at the sample was just two thirds of the one measured. The pressure during the irradiation ranged from $4.9 - 9.5 \cdot 10^{-7}$ mbar. Irradiation of one sample took approximately 5 minutes. For the irradiation of the CVD grown MoS_2 monolayers, an isotope with a lower abundance was chosen so that the flux was lower. Here, the current was only 0.2μA and did not change with the stopping voltage. The samples were baked for one hour, then stayed in vacuum over night and were baked again for one hour at maximum power. During the irradiation, the heating was turned off. The sample holder was still hot when taken out of the chamber.

Neon (Ne, 10, 20 u)

Before the neon irradiation, the implantation chamber was wiped with ethanol and baked. The stopping voltage was chosen before calibration as 20.023 kV. The beam current was 40 μA, which is extremely high when compared to others. The implantation took less than one minute for each sample. The pressure during the implantation was $1.2 \cdot 10^{-6}$ mbar. After the implantation, the stopping voltage was calibrated and found to be 19.993 kV. Thus, the implantation energies were 30 eV higher than originally expected, table 4.3 shows the correct, i.e. higher, values.

Manganese II (Mn, 25, 55 u)

The stopping voltage for Mn was tested again since in the first implantation experiment it was a lot lower than for all other experiments. This time, it was found to be 20.058 kV. However, during the test we were uncertain that the beam was actually Mn. The peak next to the one tested also had the same stopping voltage. Most likely one of the two peaks was Mn, the other one iron. Still this measurement implies that the energies during the irradiation were off by roughly 1150 eV.

Silver (Ag, 47, 108 u)

The plan was to also irradiate some samples with silver during the stay in Helsinki. However, due to a gas alarm during the experiment this was not possible. It is noteworthy however, that the stopping voltage was measured and found to be 20.018 kV, which is different than for the first and second irradiation experiments. The heating was on for 15 hours at maximum power.

4.2 Samples irradiated with argon at 50 - 200 eV

For samples irradiated with argon, the microscopic analysis did not result in conclusive results. The images in figure 4.1 show ADF images of, presumably, 50 eV Ar^+ irradiated samples. (a) to (c) show a zoom series, images taken at the same position but with different field of views of the sample Helsinki 28, a CVD double layer sample. Looking at the hexagonal lattice, it is obvious that this is a monolayer, as for double-layer samples some kind of moiré would be visible. (a) shows a monolayer with hetero atoms substituting some carbon atoms. They are brighter, due to their higher atomic mass and thus larger scattering cross section. In (b) some holes in the lattice are visible. In panel (c) it is seen, that most of the surface of the sample is covered in contamination and only small areas of the sample show the uncontaminated structure.

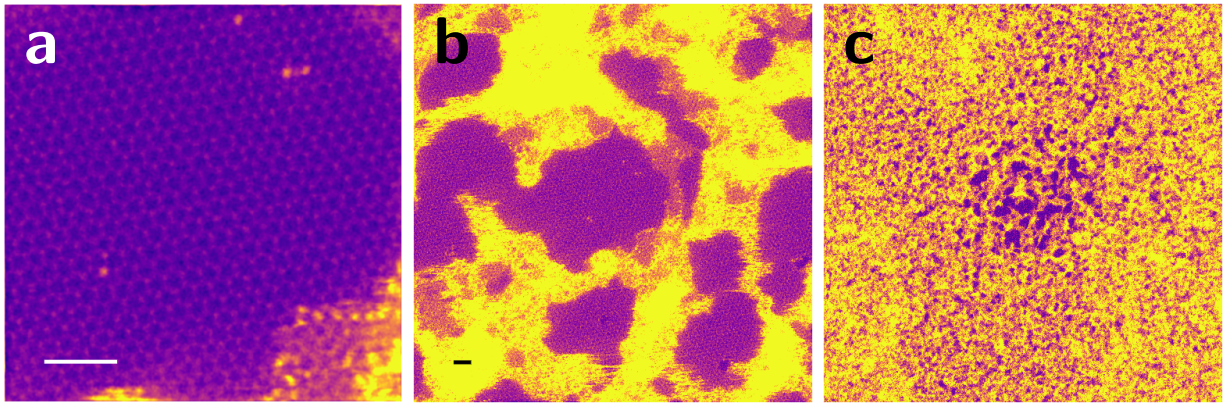

Figure 4.1: Filtered MAADF STEM images of FLG irradiated with 50 eV Ar^+ at a dose of 10^{15} $\frac{\text{ions}}{\text{cm}^2}$, scale bar (a) & (b): 1 nm. FOV (c): 250x250 nm. The images show a zoom series on Helsinki 28. The hexagonal structure visible in the images is graphene, the bright areas covering it are contamination, most likely amorphous hydrocarbon. Some atoms in the graphene structure appear brighter than others indicating hetero-atoms substituting carbon in the structure.

On samples irradiated with 100 eV Ar^+ at a dose of 10^{15} $\frac{\text{ions}}{\text{cm}^2}$, it appeared that a higher density of hetero-atoms could be observed than in non-irradiated samples. Some of these hetero-atoms disappear during imaging while others move. Whenever we were able to collect EELS signal from the hetero-atoms, they were silicon. The analysis of the samples irradiated with argon during Helsinki I was not only done using the Nion UltraSTEM 100 in Vienna, but also some samples were taken to Nottingham to look at them in a TEM and perform EDX there. Samples Hel 12, 100 eV Ar^+, $10^{15}\,\frac{\text{ions}}{\text{cm}^2}$, and Hel 10, 200 eV Ar^+, $10^{14}\,\frac{\text{ions}}{\text{cm}^2}$, were investigated. Both samples were quite dirty and no argon was detected in bilayer regions. However, in sample Helsinki 10, in a much thicker flake next to the one transferred, Ar peaks seemed to appear.

4.3 Samples irradiated with krypton at 50 – 300 eV

4.3.1 Effects of 300 eV krypton irradiation on FLG

Figure 4.2 shows the effect of 300 eV Kr^+ irradiation on few layer graphene with varying thicknesses. In thicker regions no interesting effects were visible so no lattice resolution images were taken. Figure 4.2 (a) shows the difference in effect of the 300 eV irradiation for different thicknesses. In the monolayer region, left, many holes can be observed, whereas in the thicker region, right, there are none. Panel (b) shows an image of two regions with different thicknesses at a higher magnification. Panel (c) shows a high magnification image of the structure of a monolayer after the 300 eV irradiation with a field of view of 16×16 nm. Under the optical microscope one could see that next to the monolayer there were a 5-layer and a bilayer region. A line profile was drawn from the area with holes, which was monolayer, to the thicker region. With the vacuum level subtracted, the intensity of the thick region was roughly 1.3 times higher than that of the holey monolayer region. Therefore, we suspect the thicker region to be a bilayer.

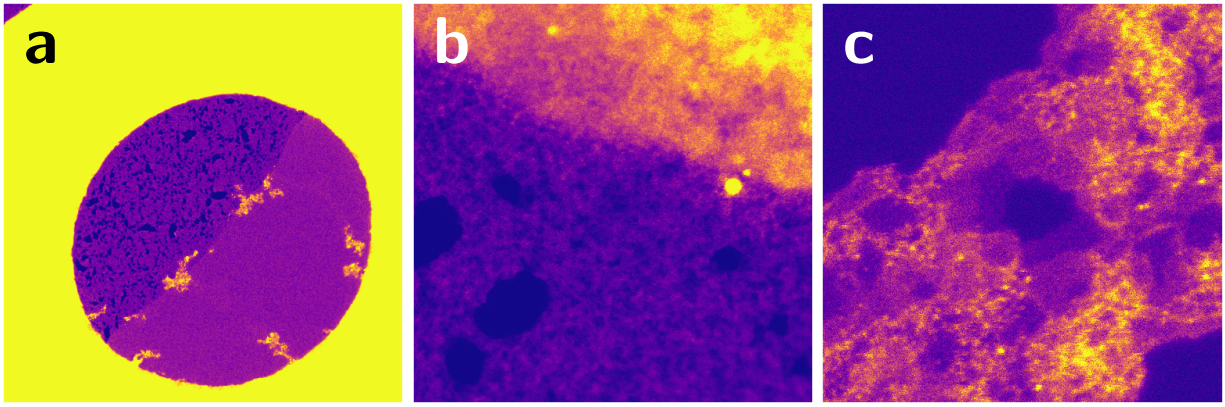

Figure 4.2: Filtered MAADF STEM images of FLG irradiated with 300 eV Kr^+ at a dose of 10^{15} $\frac{\text{ions}}{\text{cm}^2}$, FOV: (a) 2x2 μm, (b) 100x100 nm, (c) 16x16 nm. The images were taken form the sample Hel 48.

4.3.2 Effects of 50 eV krypton irradiation on FLG

One bilayer sample irradiated with 50 eV krypton was checked. However, the transfer of the flakes had been unsuccessful. In a flake of unknown thickness there were no signs of implantation.

4.3.3 Effects of 100 eV krypton irradiation on bilayers, trilayers and double layers

Figure 4.3 shows images taken from sample Hel 41, which is mostly three layers thick with some thinner regions. In the exfoliated sample, few defects were found as illustrated in the high resolution images of figure 4.3 (a) & (b). The sample seems relatively clean as can be seen in

figure 4.3 (d) & (e). Also in thicker regions, such as as the one folded in figure 4.3 (f) there are no signs of implanted krypton.

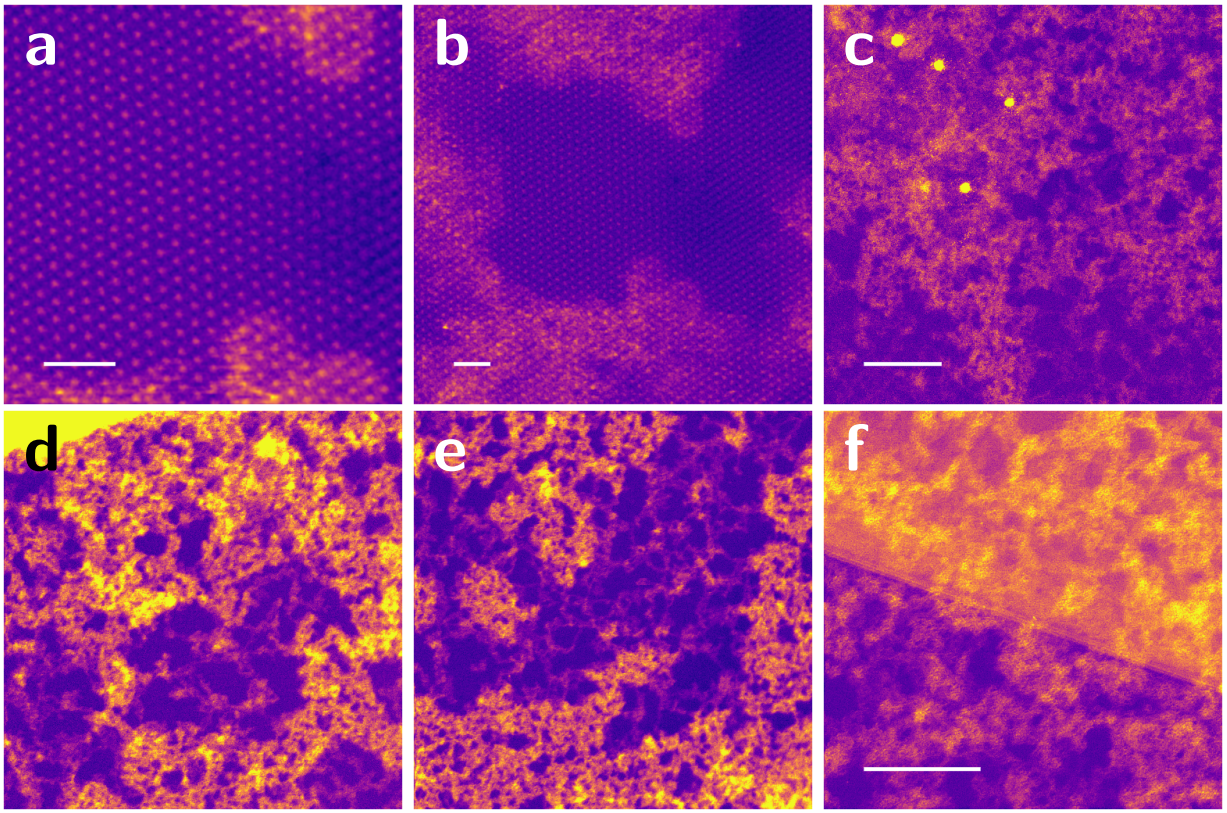

Figure 4.3: Filtered MAADF STEM images of FLG irradiated with 100 eV Kr^+ at a dose of 10^{15} $\frac{\text{ions}}{\text{cm}^2}$, scale bars: (a) 1 nm, (b) 1 nm, (c) 10 nm, (f) 10 nm. FOV (d) & (e): 128x128 nm. (d) & (f) are unfiltered images. The images were taken from sample Hel 41.

Figure 4.4 (a)-(c) show images taken from sample Hel 55, a CVD double layer on a SiN chip.Many hetero-atoms can be observed in the structures. A thicker region where the graphene was folded, shown in (c), shows no obvious sign of krypton implantation.

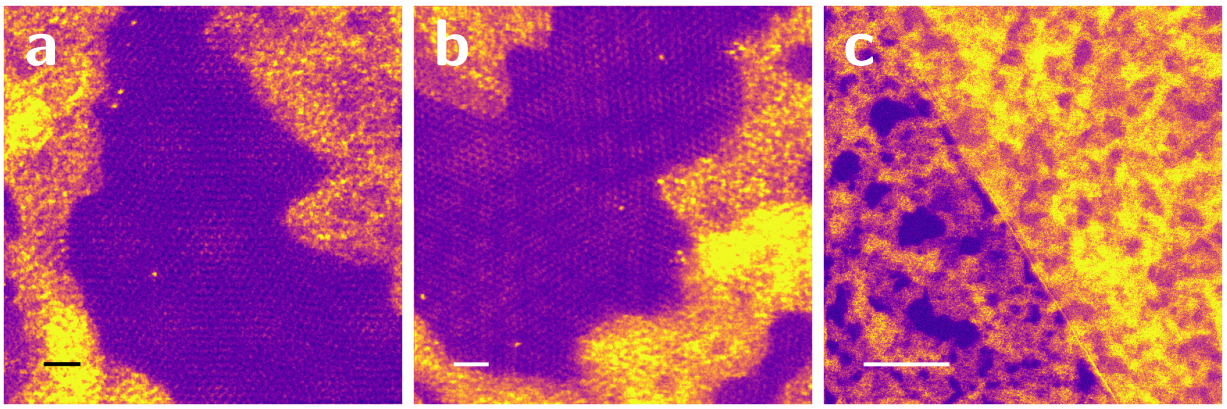

Figure 4.4: Filtered MAADF STEM images of FLG irradiated with 100 eV Kr^+ at a dose of 10^{15} $\frac{\text{ions}}{\text{cm}^2}$, Scale bars: (a) 1 nm, (b) 1 nm, (c) 10 nm. (c) A folded area where the sample is thicker (unfiltered). The images were taken from sample Hel 55.

Figure 4.5 shows sample Hel 37 – a sample irradiated with 100 eV krypton. These images were taken from a bilayer region. Figure 4.5 (a) shows a structure of unknown origin. It rotated over

time but remained otherwise stable under the 60 kV electron beam. The hetero-atom that can be seen above it changed position during the image series. Figures 4.5 (b) – (c) and (f) are larger field of view images of (a); (f) shows the entire hole. In figure 4.5 (d) and (e) it can be seen, that the observed areas in sample Hel 37 were slightly more contaminated than the ones in Hel 55. The hole on the right in panel (f) was covered with a bilayer of graphene, the hole on the bottom left corner was covered with a five layer thick graphene membrane.

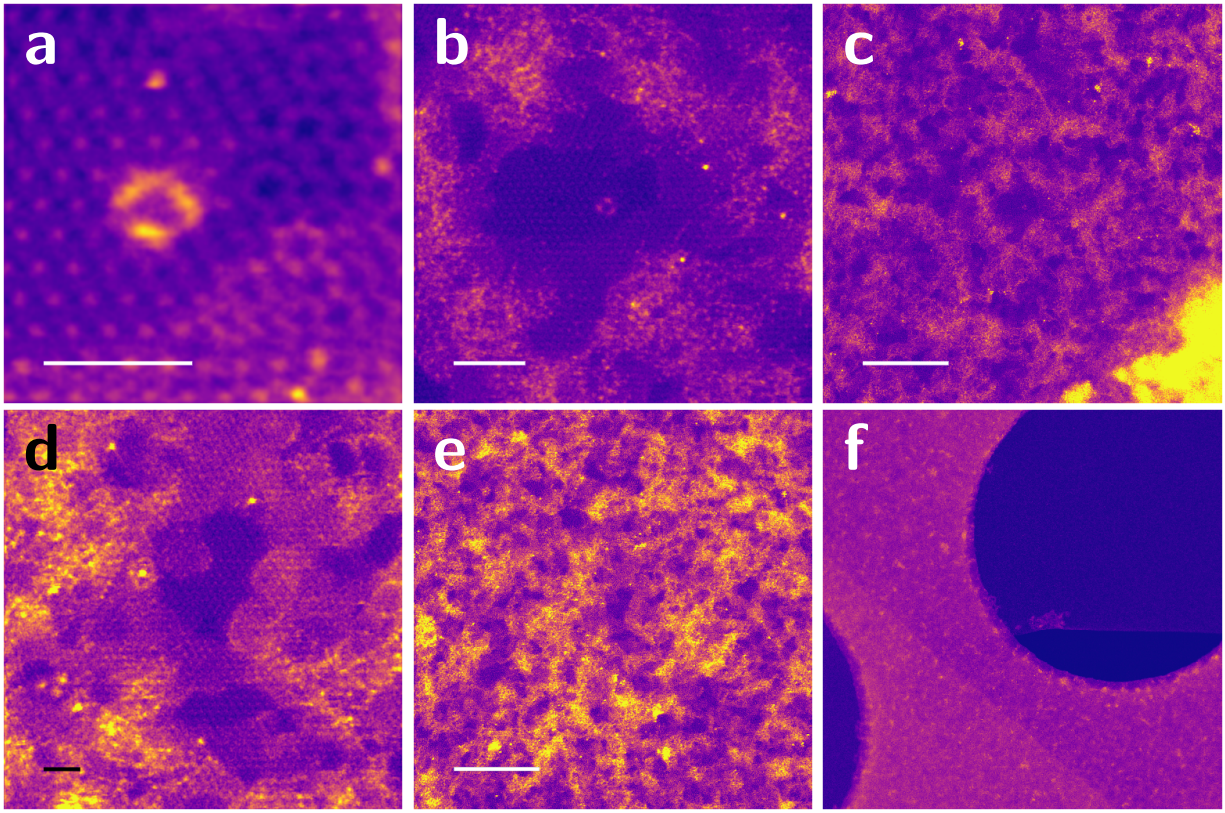

Figure 4.5: Filtered MAADF STEM images of FLG irradiated with 100 eV Kr^+ at a dose of 10^{15} $\frac{\text{ions}}{\text{cm}^2}$, scale bars: (a) 1 nm, (b) 2 nm, (c), 10 nm, (d) 10 nm, (f) 2x2 μm FOV. Images were taken in a bilayer region from Hel 37.

4.3.4 Effects of 100 eV krypton irradiation on 5- and 6-layer graphene

Figure 4.6 shows a thicker region, either 5 or 6 layers, of sample Hel 37. At a large field of view, figure 4.6 (a) & (b), it looks similar to a bilayer of contaminated graphene. Higher magnification images reveal an intrinsic structure of the bright areas. Patterns of regularly spaced dots can be observed, as in panels (c) & (d). These dots are individual atoms or atomic columns forming crystalline structures. The crystallites are close to each other but do not touch. In panel (d), two crystallites have been highlighted in black. The distance between crystallite clusters seems to be characteristic for the system since it can be found in all images taken from these structures. In the central crystal in panel (d) it can be observed, that some of the atoms are brighter and smaller than others which appear larger and dimmer.

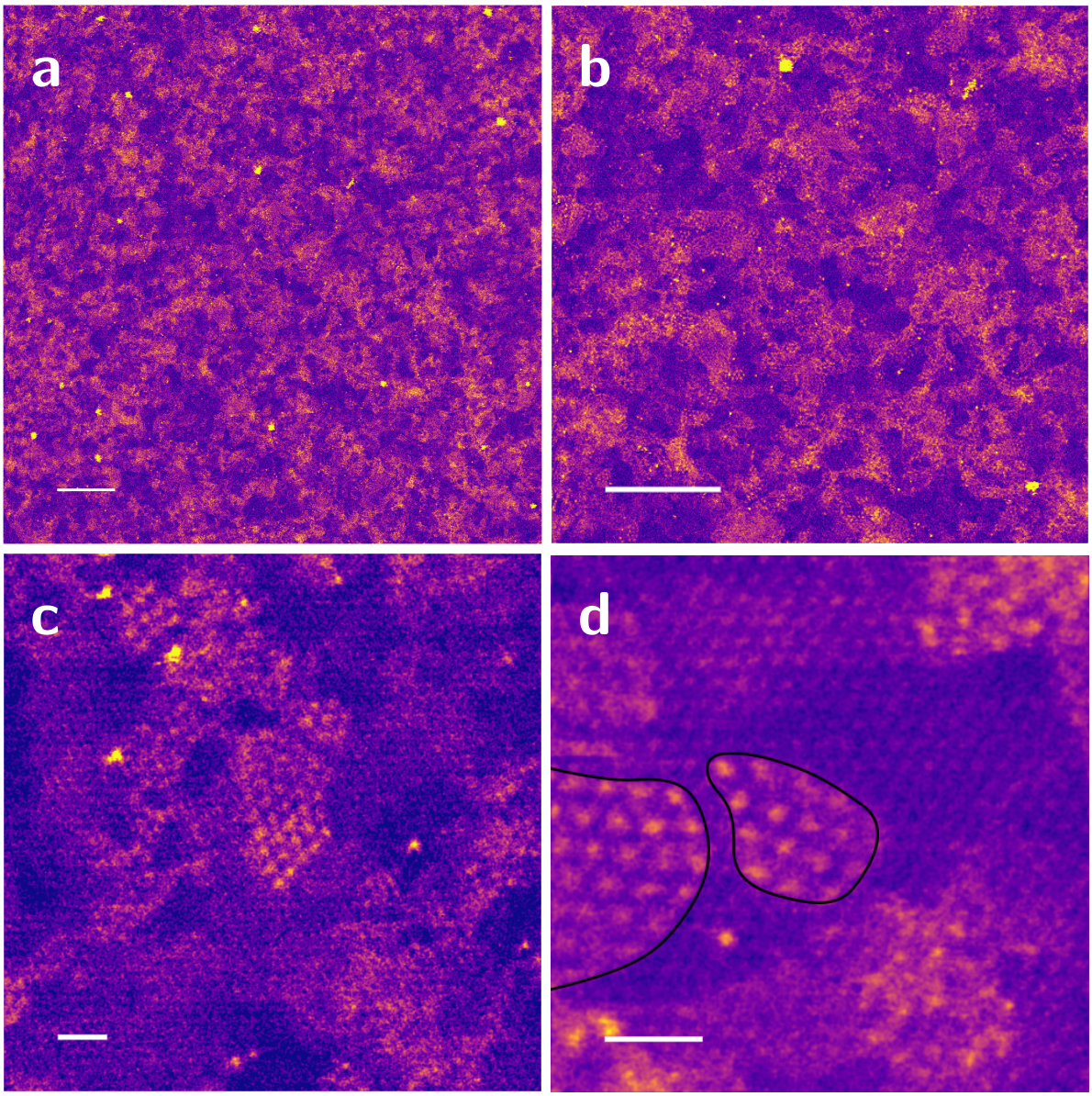

Figure 4.6: Filtered MAADF (a,b,d) & HAADF (c) STEM images of FLG irradiated with 100 eV Kr^+ at a dose of 10^{15} $\frac{\text{ions}}{\text{cm}^2}$, scale bars: (a) 10 nm, (b) 10 nm, (c), 1 nm, (d) 1 nm. All images were taken in a 5- or 6-layer thick region of Hel 37. (b) A zoom-in of (a). In panel (d), two crystallites are highlighted in black to illustrate that they do not have straight edges.

4.3.5 Interatomic distance in a cluster

To estimate the bond length of the atoms in the crystallites, the distances between nearest neighbours were measured in a few crystals. For the first estimation, images with a small field of view were analysed. A line profile, as described in the methods, was used for measuring the lattice parameters of the crystallites as shown in figure 4.7. The interatomic spacings were measured for the big crystallite in figure 4.7 (a) and all the clusters marked by numbers in panel (b) – (d). The distances were measured in all directions for these clusters. Figure 4.7 (g) displays the measured distances in a histogram. The thus found distance is

$$d_{interatom} = (375 \pm 42)\ \text{pm}, \tag{4.1}$$

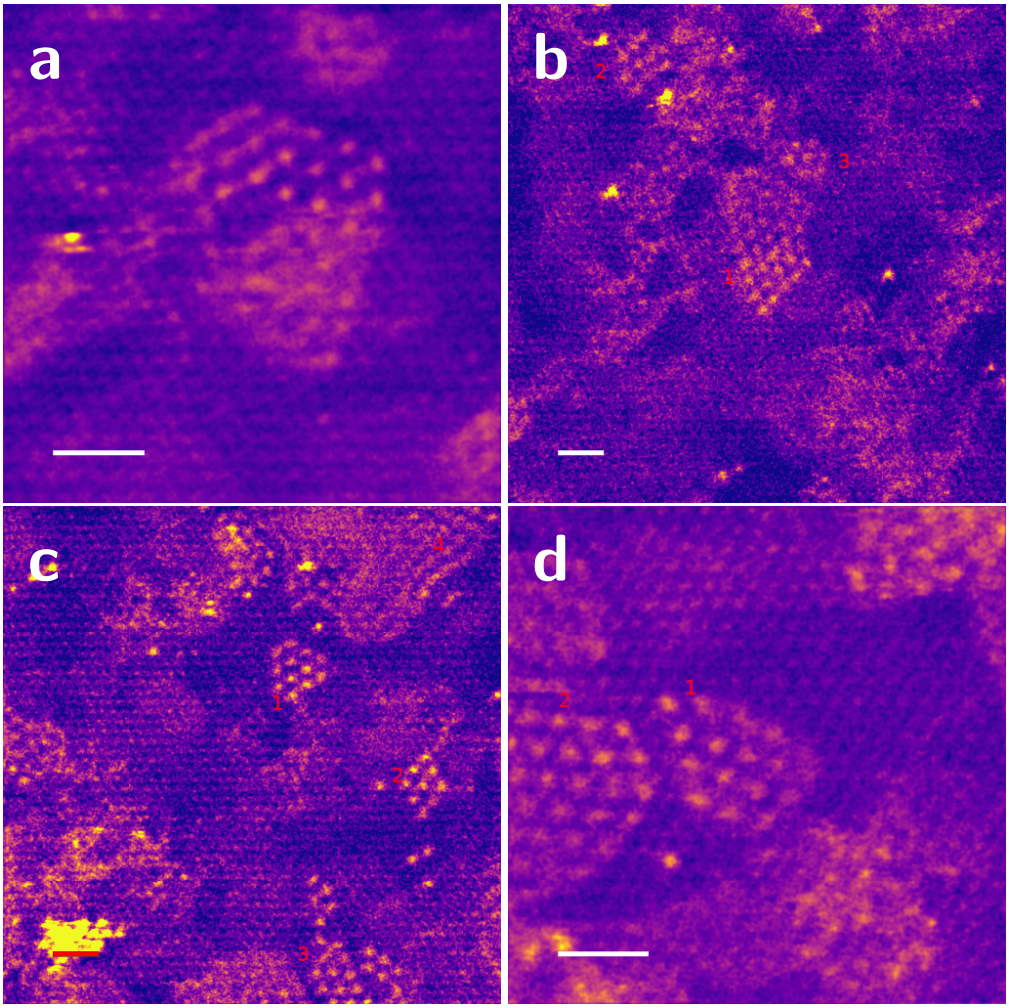

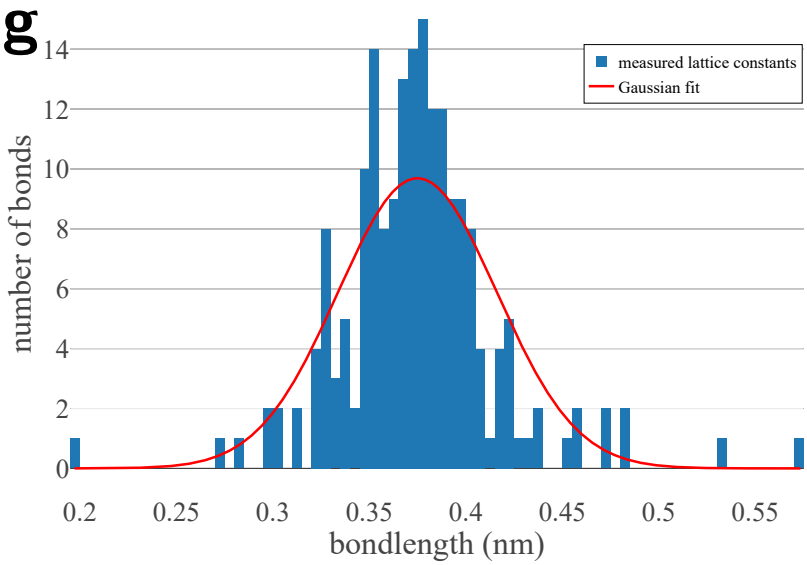

Figure 4.7: Filtered MAADF (a) & (d) & HAADF (b) & (c) STEM images of FLG irradiated with 100 eV Kr^+ at a dose of 10^{15} $\frac{\text{ions}}{\text{cm}^2}$, scale bars: 1 nm. All images were taken in a 5- or 6-layer thick region oh Hel 37. (g) Histogram showing the distribution of clustersizes in 100 eV Kr irradiated samples.

where the mean was chosen as the average distance and the uncertainty is given by the standard deviation. A total of 191 interatomic distances were used for the calculation 4.1.

4.3.6 Implantation efficiency and cluster size

The implantation efficiency was estimated by counting individual atoms in the images. As shown above, not all atoms are clearly distinguishable. While the clusters are at times in a solid phase and atoms are visible as clear dots, sometimes they are in a liquid phase and can not be resolved individually. Sometimes half a cluster is solid and half the cluster is liquid, sometimes a cluster changes phase while being imaged. Therefore determining the actual cluster sizes and counting the number of implanted atoms can not be very accurate. The presented data is thus more of an estimation than an accurate measurement. Table 4.4 displays the number of counted clusters and their sizes for five different images (not displayed here). When estimating the size of the clusters, only the atoms which could be clearly identified were counted for the cluster size. Thus the actual number of implanted atoms is higher than estimated here. One image was analysed twice where two different numbers of clusters and, thus, differing implantation efficiencies were estimated. Because of the inaccuracy of this measurement, the values do not correspond to actual implantation efficiencies but rather approximate minimum efficiencies which could be around twice as high.

Table 4.4: **Implantation efficiency of 100 eV Kr irradiated FLG samples.** Values obtained by counting atoms in images. Image 3 was analysed twice resulting in different numbers of clusters and also a different implantation efficiency. This happens due to the slightly arbitrary way of counting atoms and clusters.

Image	area [nm^2]	# clusters	# partly liquid	# atoms	imp. efficiency	thickness
1	2216	44	20	231	10.9 %	6
2	2216	41	20	577	27.2 %	5
3	2216	38	21	305	12.4 %	5
3	2216	40	18	393	13.8 %	5
4	2216	39	23	274	12.9 %	5
5	520	18	9	92	17.7 %	5

The implantation efficiency varies between 12 and 27 %. Image five was smaller than the other images and the implantation efficiency lies in the same order of magnitude. Approximately half the clusters are in part liquid. Figure 4.8 shows the distribution of cluster sizes in these five images. Here it is important to note that only the clusters without additional liquid phases were counted. So approximately half the clusters are not displayed in this histogram, since especially large clusters are more often in liquid and solid phases at the same time.

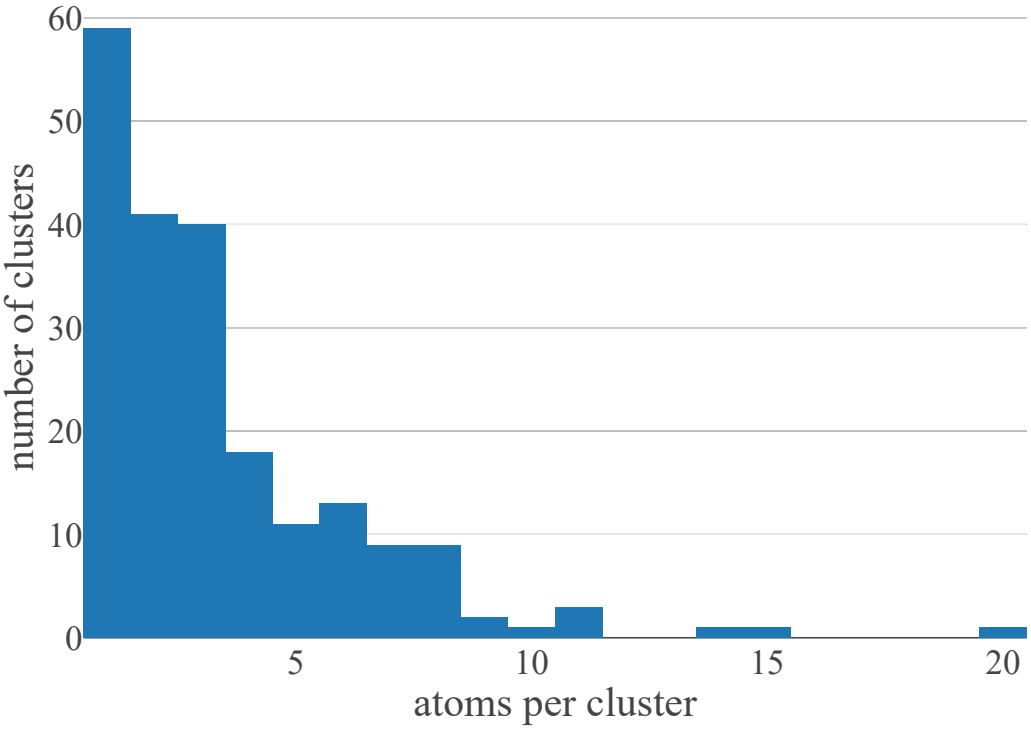

Figure 4.8: Distribution of cluster sizes in 100 eV Kr irradiated sample Hel 37.

4.3.7 Dynamics in the observed systems

Figure 4.9 shows the evolution of the imaged area under electron irradiation over a time of ca. 7.5 minutes. Images (a) – (e) are taken at the same position, whereas in (f) – (j) the field of view is slightly shifted downwards.

There are three crystals of interest. Crystal 1 is slightly above the centre. In the first two frames the atomic positions are very distinct and sharp. In the third image it moves to the right and is afterwards not as stable and solid as it was in the beginning.

Crystal 2 is in the middle of the right side. Also here the crystal stays very much in place. However its structure changes over time. First there is a crystallite consisting of 9 atoms and an individual atom on the left side of it. From panel (e) to panel (f) the atoms in the crystal become more mobile. In panel (i) there is again a cluster of 9 atoms, bent around an individual atom on the right side of the cluster.

Crystal 3 at the bottom right exhibits a, for this system, very typical behaviour. One can see a crystalline cluster with very sharp atomic positions framed by a cluster where the atoms are not confined in all images. In panels (b) & (c) the left cluster has crystalline structure,whereas it appears more liquid like in the rest of the images. Thus we can be relatively certain, that the encapsulating cluster consists of krypton atoms. In panel (i), it is clearly visible that two clusters with very sharp atomic positions are framed by one big cluster which appears to be in a liquid phase. This behaviour can be seen in many images and seems to be characteristic for this system.

Bending edges, as described before, can also be observed here. Atomic movements are orders of magnitude faster than the imaging process, which takes around second per image. This implies that all of the observed dynamics have to be at least semi-stable states.

This time series was recoded while trying to confirm the atomic species via EELS. Thus some of the dynamics and phase changes seen in these images were probably activated by putting the electron beam on the individual clusters.

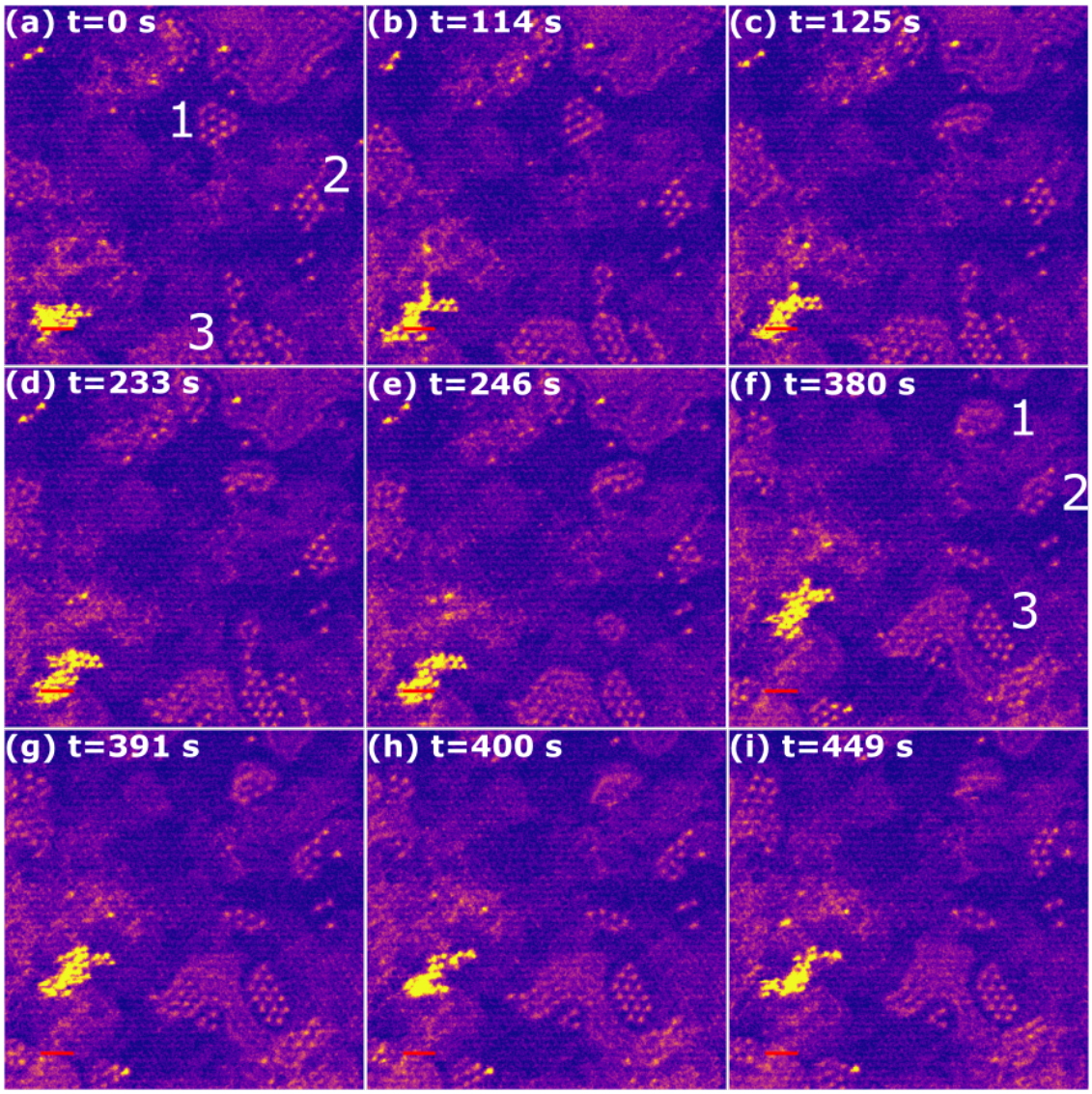

Figure 4.9: Filtered HAADF STEM images of FLG irradiated with 100 eV Kr^+ at a dose of 10^{15} $\frac{\text{ions}}{\text{cm}^2}$, scale bars: 1 nm. Images were taken at the same positions at different times. There is a slight change in the field of view between panels (a)-(e) and panels (f)-(i).

4.3.8 Characteristic inter-cluster distance

Often crystallites do not have straight edges, but are slightly bent towards each other with a gap in between. This gap was observed im many images. To see whether the distance is characteristic, it was measured using two methods. First a line profile was drawn from atoms from one cluster to atoms of another. In practice this is not as easy as measuring the interatomic spacing in images.

Figure 4.10 shows a histogram of 27 measured inter-cluster distances, the distance between the closest atoms from two neighbouring clusters.

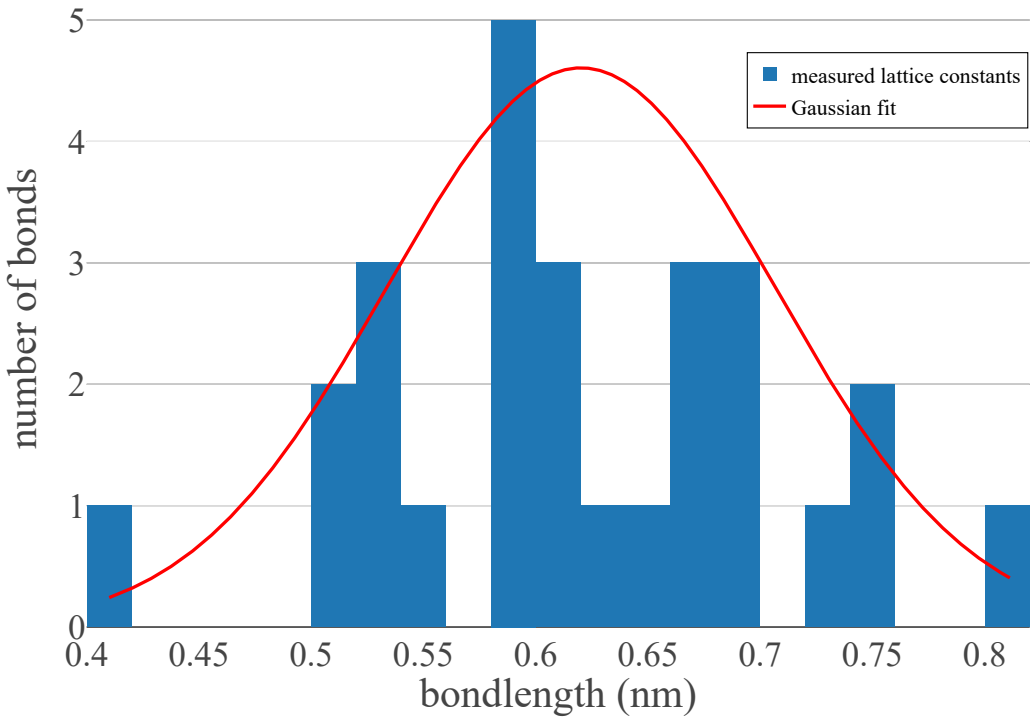

Figure 4.10: Histograms of the measured characteristic distances.

The resulting inter-cluster distance from the Gaussian fit is

$$d_{intercluster-1} = (620 \pm 87)\ \text{pm} \tag{4.2}$$

which becomes

$$d_{gap-1} = (245 \pm 129)\ \text{pm} \tag{4.3}$$

when the interatomic distance is subtracted. This method only works for well defined crystals next to each other which is not the case for many of the images we have obtained which is why there are so few data points. Most distinct clusters are next to clusters in a semi-liquid state.

4.3.9 EELS fingerprint of krypton

An EELS spectrum was tried to be obtained to verify that the implanted atoms were indeed krypton. Figure 4.11 shows a a microscopy image with two spots where spectra were obtained (a) as well as the two normalized spectra and their difference(b). A very faint signal can be observed which resembles the krypton $M_{4,\,5}$ edge. It was impossible to obtain a stronger signal from the small clusters.

For cleaning purposes, sample Hel 37 (the only sample where krypton crystals were observed)

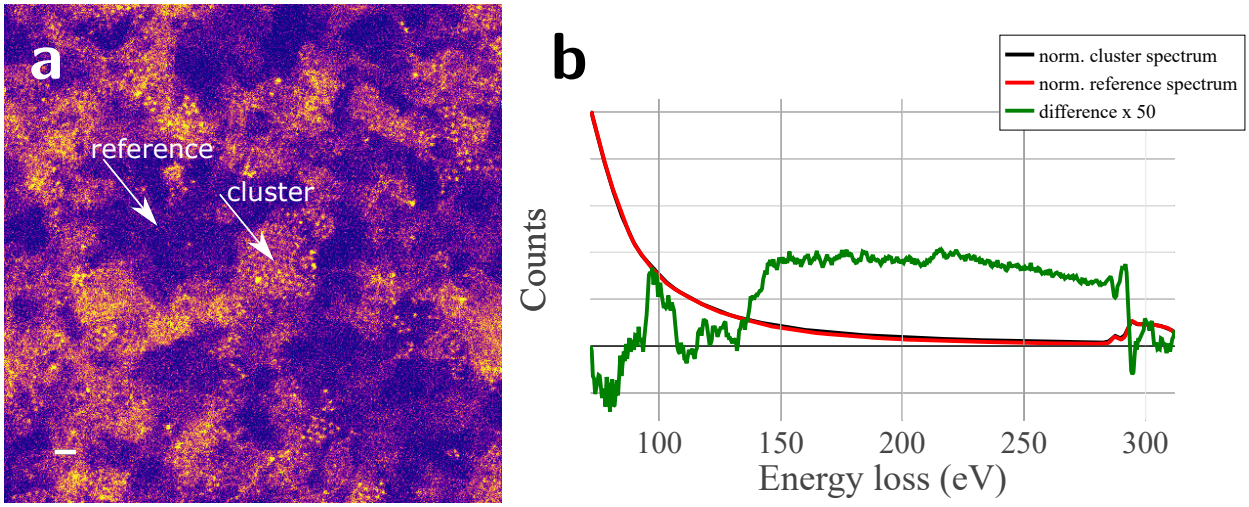

Figure 4.11: (a) Filtered HAADF STEM images of Hel 37 witz positions of cluster and reference spectrum marked, FLG irradiated with 100 eV Kr^+ at a dose of 10^{15} $\frac{\text{ions}}{\text{cm}^2}$. Scale bar: 1 nm., (b) EELS spectrum: cluster signal in black, reference signal in red, subtracted signal in green. Note that the signal is multiplied by 50.

was lasered. Figure 4.12 shows the sample after the laser treatment. Lasering thinned the membrane so much that it did not provide a stable imaging substrate afterwards. Therefore, no high resolution images could be obtained from those positions, where images shown in figures 4.9, 4.7, 4.6 and 4.5 were recorded. Figure 4.12 (a) shows the region where all atomic resolution images presented before were made, panel (b) shows the bilayer region where no implanted krypton could be found and panel (c) shows a hole, which was partly covered by a bilayer and partly by a thicker piece. As can be seen in the thicker areas, new bright pockets are visible. The image in panel (a) shows the positions where the two EELS spectra displayed in panel (d) were obtained. The normalized signal from the pocket is shown in black, the normalized reference spectrum from next to the pocket is shown in red, and the difference is shown in green. The edge clearly corresponds to the $M_{4,\,5}$ edge of krypton which starts at 89 eV, which proves that we indeed implanted krypton into the sample. We assume it collected into bubbles between the layers after the laser treatment due to thermal diffusion. Additional spectra were taken from most bright spots displayed in these images. In all of these spectra the same edge as displayed in panel (d) was detected.

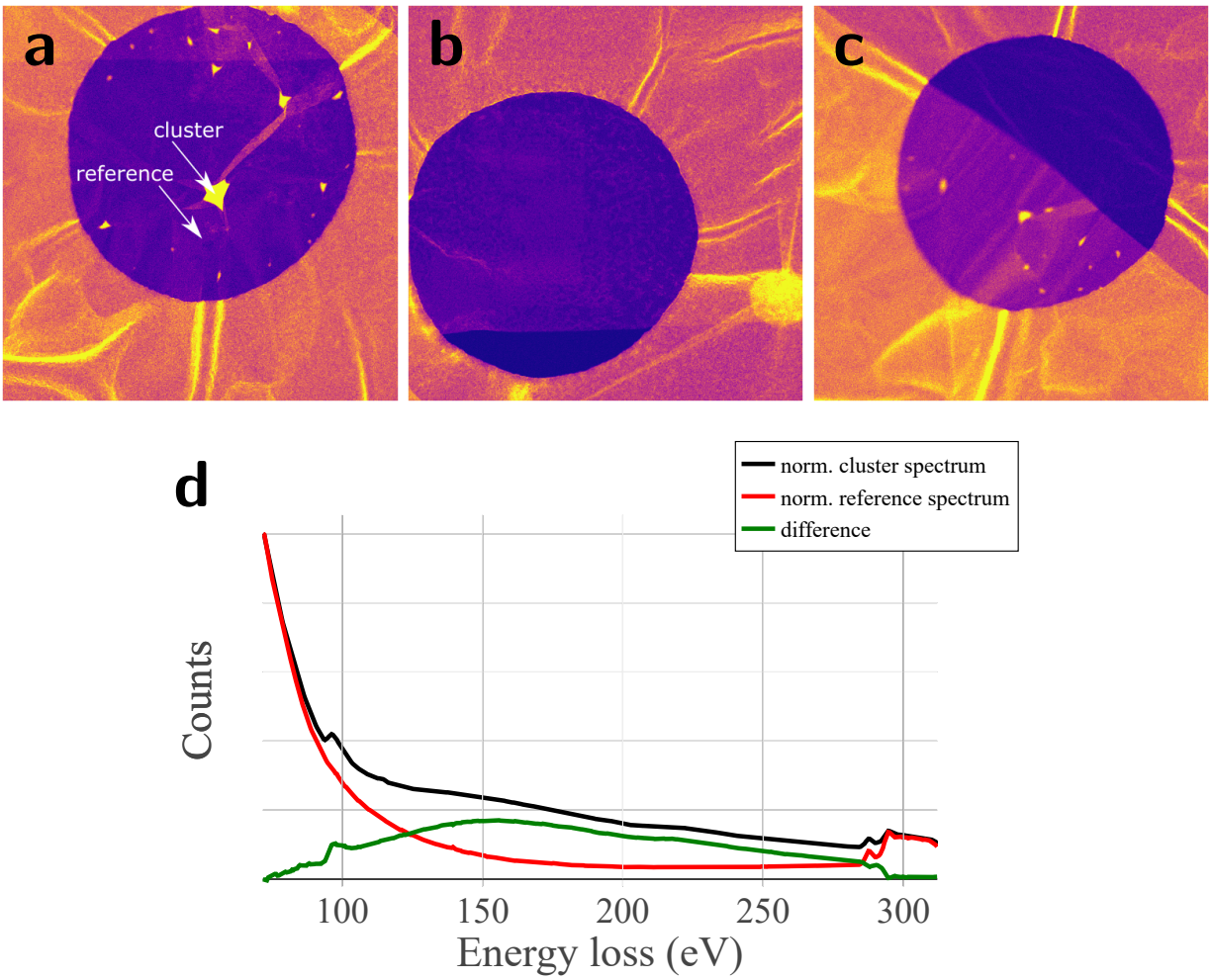

Figure 4.12: (a)-(c) Filtered MAADF STEM images of Hel 37, FLG irradiated with 100 eV Kr^+ at a dose of 10^{15} $\frac{\text{ions}}{\text{cm}^2}$ after laser treatment. FOV: 2x2 μm, (d) EELS spectrum: cluster signal in black, reference signal in red, subtracted signal in green.

4.3.10 Structure after cleaning/destruction

Since the sample was very unstable after laser treatment, it was difficult to take more images from this sample. We were, however, able to take some images at the point locally furthest away from the laser impact. Figure 4.13 shows a selection of those obtained images. Individual atoms are rarely visible for bigger clusters implying that they are in a liquid state. In panels (b) & (f), individual atoms can be seen surrounded by bright areas. Panels (a), (c) & (d) show the edges of bubbles in a liquid phase. Panel (e) shows liquid bubbles and crystals at the same time.

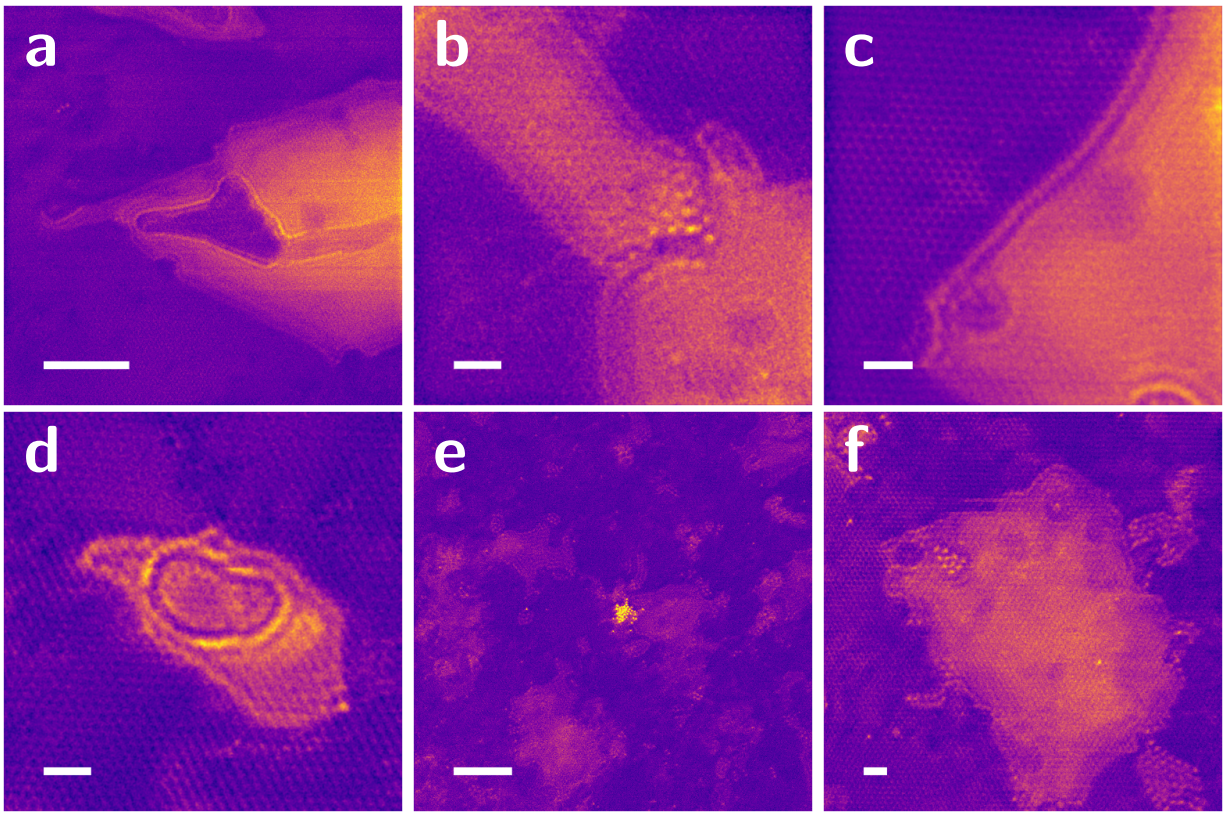

Figure 4.13: Filtered MAADF STEM images of FLG irradiated with 100 eV Kr^+ at a dose of 10^{15} $\frac{\text{ions}}{\text{cm}^2}$, Scale bars: (a), (e)= 5 nm, (b)-(d),(f)= 1 nm. All images were taken in a 5-6 layer thick region.

Figure 4.14 shows a large field of view of a 6-layer thick graphene region irradiated with krypton. The sample has been hit with a laser several micrometers away. The image is extremely rich in detail and many typical features seen in other images can also be observed here. It can be observed, that larger bubbles do not exhibit crystal like features any more. To show this in more detail, some bubbles are shown larger in figure 4.15. Also some characteristic distances, described above, can be seen in figure 4.14, and in figure 4.16. Interestingly many round shapes can be observed in figure 4.14, with but also without central atoms. Some of these shapes are shown again in figure 4.17.

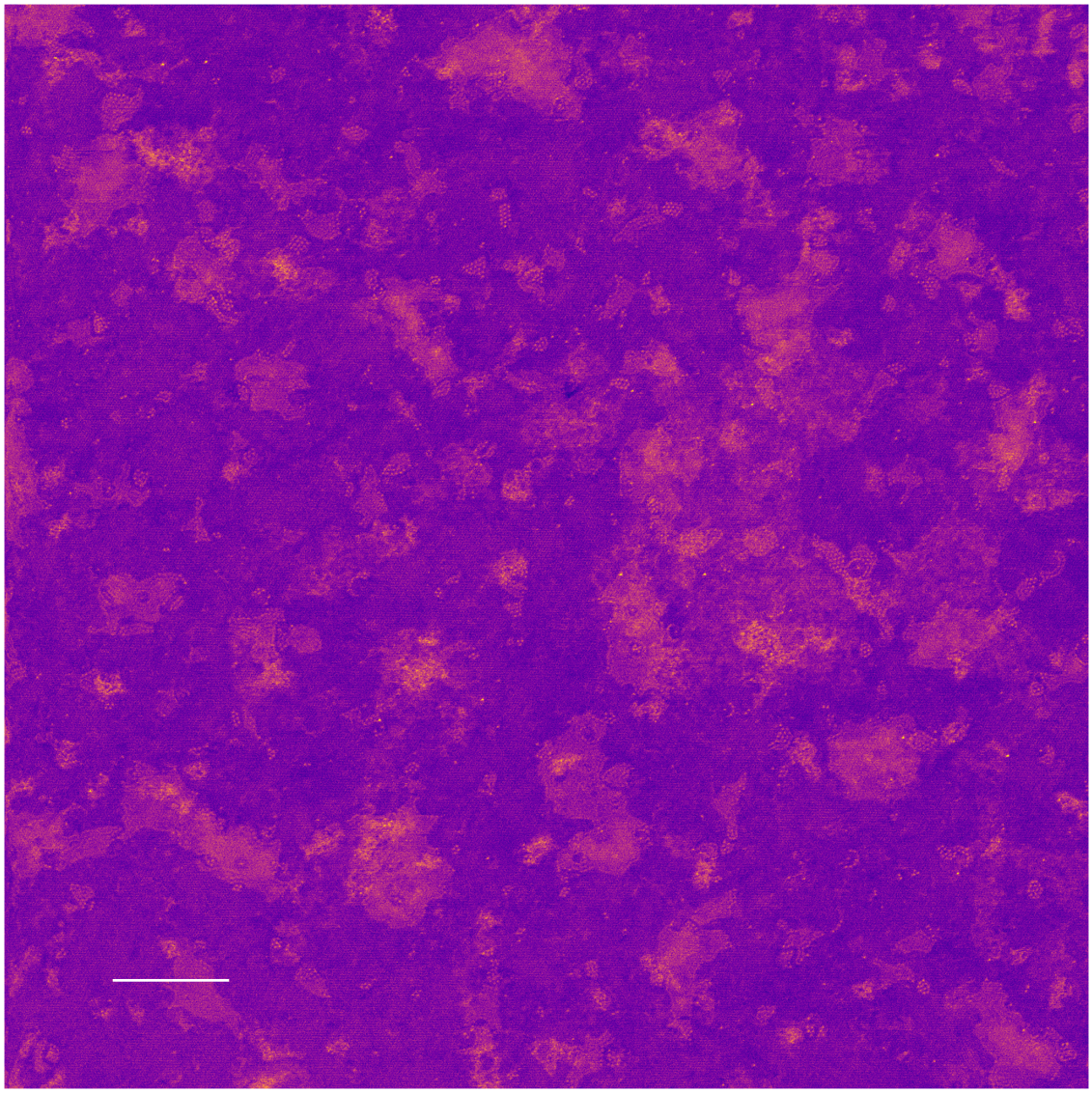

Figure 4.14: (a) Filtered MAADF STEM image of Hel 37, FLG irradiated with 100 eV Kr^+ at a dose of 10^{15} $\frac{\text{ions}}{\text{cm}^2}$, scale bar: 10 nm. Sample Hel 37.

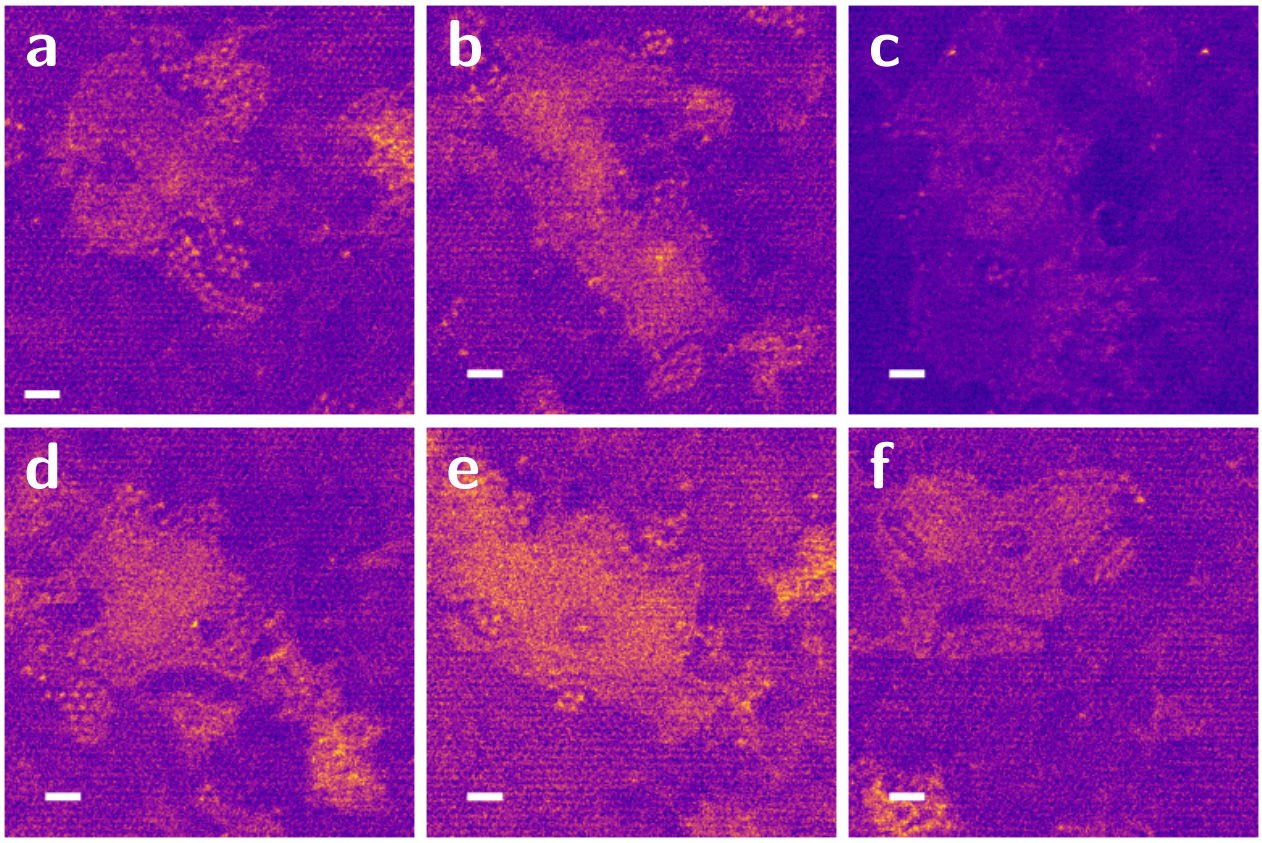

Figure 4.15: (a) Filtered MAADF STEM image of Hel 37, FLG irradiated with 100 eV Kr^+ at a dose of 10^{15} $\frac{\text{ions}}{\text{cm}^2}$, scale bar: 10 nm. Sample Hel 37.

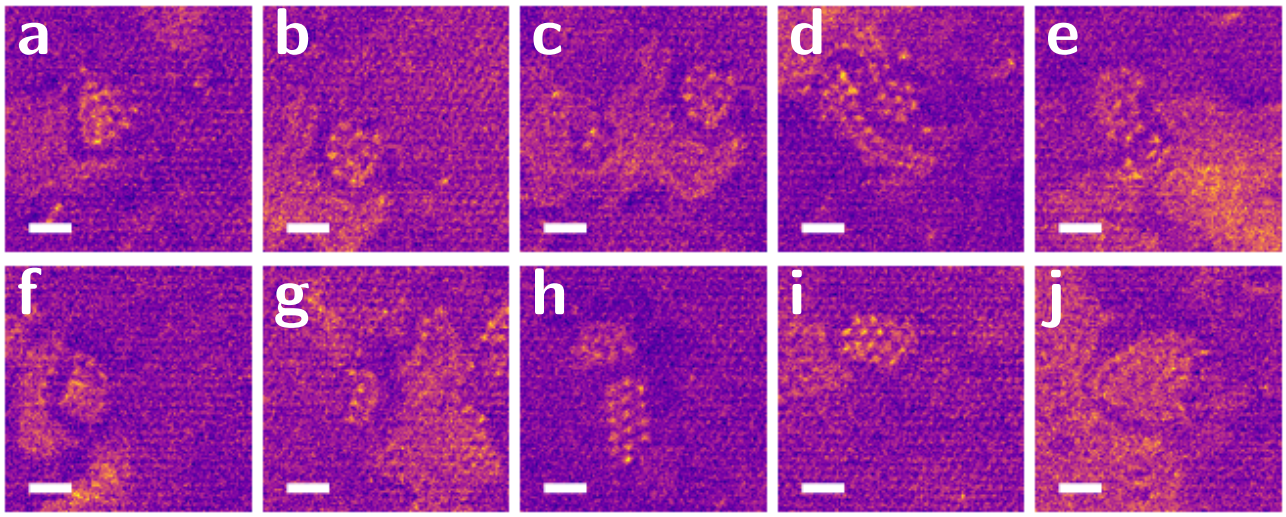

Figure 4.16: (a) Filtered MAADF STEM image of Hel 37, FLG irradiated with 100 eV Kr^+ at a dose of 10^{15} $\frac{\text{ions}}{\text{cm}^2}$, scale bar: 10 nm. Sample Hel 37.

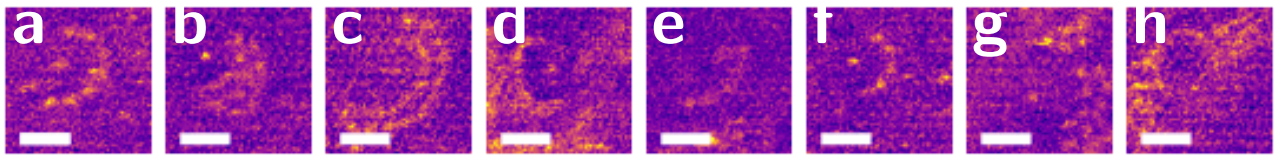

Figure 4.17: (a) Filtered MAADF STEM image of Hel 37, FLG irradiated with 100 eV Kr^+ at a dose of 10^{15} $\frac{\text{ions}}{\text{cm}^2}$, scale bar: 10 nm. Sample Hel 37.

4.4 Comparison of simulated images and visualisation of bond length

Figure 4.18 shows simulated STEM images as well as the structure that was simulated. Panel (a) visualizes the structure of the system consisting of 6 layers of AB stacked graphene with seven krypton atoms with the above measured bond length (3.73 Å). Panels (c) – (f) show simulated images from that structure. Panels (c) & (d) are simulated MAADF images plotted with different contrast. Images (e) & (f) are are simulated HAADF images plotted with different contrast settings.

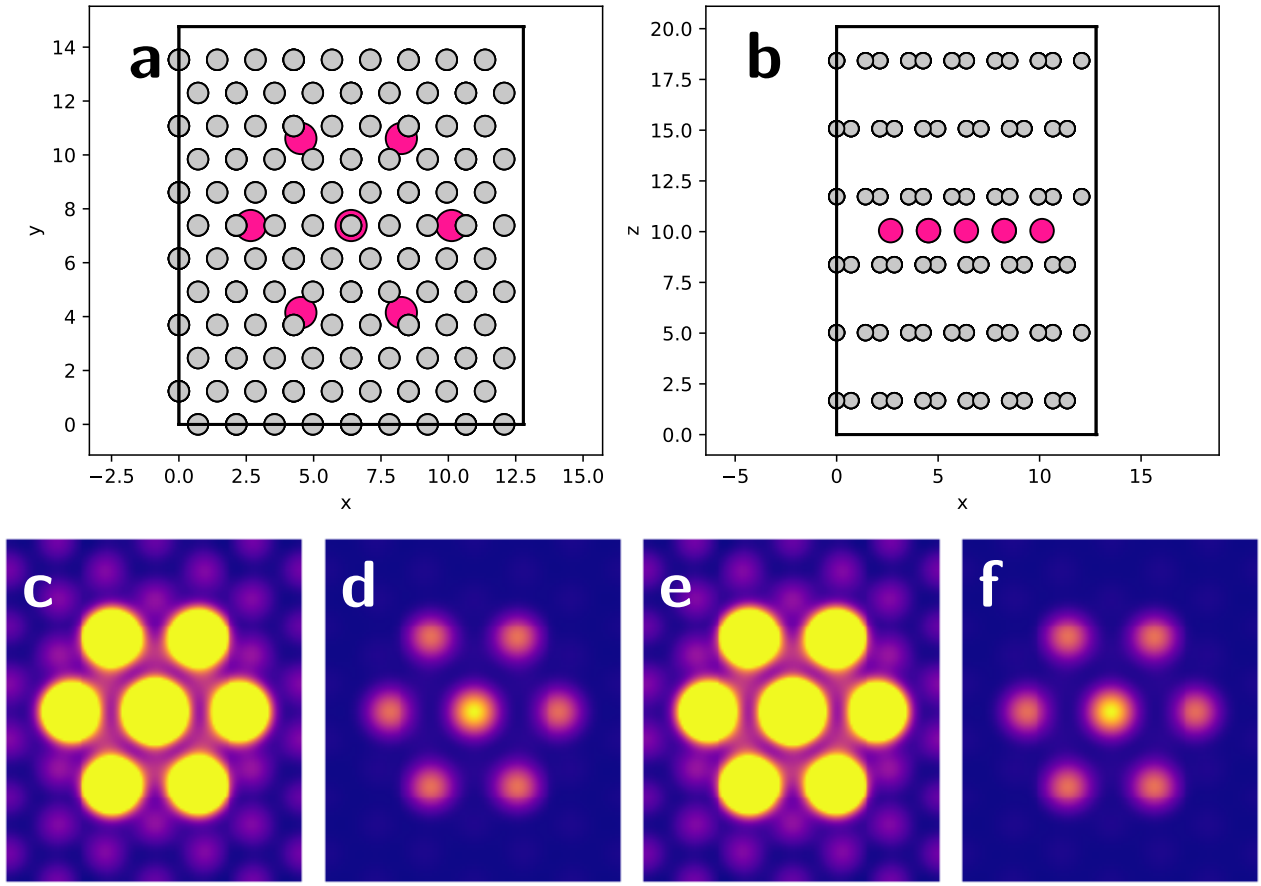

Figure 4.18: (a) & (b) Visualisation of structure. Comparison of the lattice parameters and the krypton atoms can be observed here quite well. (c) & (d) Simulated MAADF STEM images with varying contrast settings. (e) & (f) Simulated HAADF STEM images with varying contrast settings.

In simulated images, Kr atoms appear brighter in comparison to carbon than in the actual microscopy images. As the noise level and the sensitivity of the detectors in the microscope are unknown three different values need to be compared to each other. Figure 4.19 shows the line profiles that were used for comparing the intensities in the simulated images. The MAADF images and profiles are shown, however the same analysis was done for the HAADF images.

In the simulated images, there are 3 different peak intensities. 3 Carbon atoms on top of each other, 6 carbon atoms on top of each other and one krypton atom on top of the background.

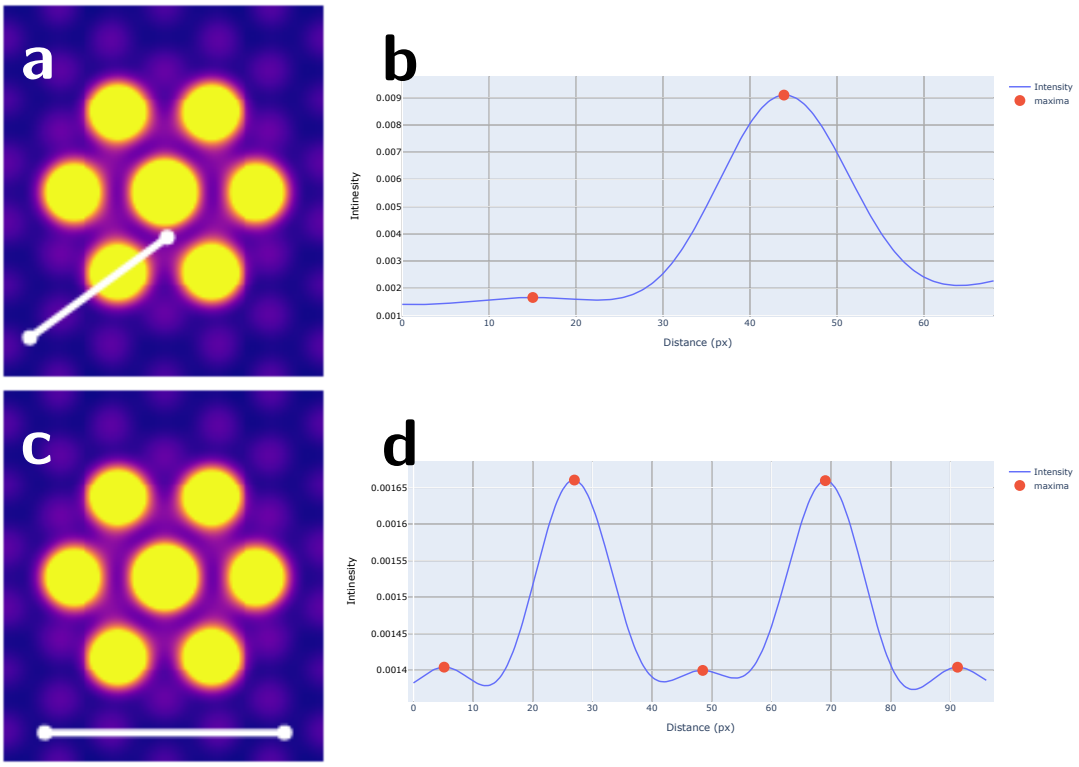

Figure 4.19: (a) & (c) Simulated MAADF STEM images with line profiles. (b) & (d) Intensities along these line profiles.

The ratios in MAADF mode between the intensities are

$$ratio_{sim-MAADF} = 0.89 : 1 : 4.33. \tag{4.4}$$

from the 3 carbon atom column to the 6 carbon atom column to the krypton atom. The line profiles were drawn with a width of 3 px. In HAADF the ratios are given by

$$ratio_{sim-HAADF} = 0.85 : 1 : 5.47. \tag{4.5}$$

To estimate the noise level of the MAADF detector a line profile was drawn in the vacuum part of figure 4.5 (f). The average noise value was 0.00133 at a dwell time (exposure time of one picel to the beam) of 16 μs which is the same as in figure 4.20 (a). After subtracting the background from both peak intensities the ratio between the 3 carbon atom column, the 6 carbon atom column and the Kr atom is given by

$$ratio_{exp-MAADF} = 0.692 : 1 : 2.6. \tag{4.6}$$

The image was filtered before the background subtraction and that already reduced the noise in the image as can be seen in figure 3.11 in the methods. Thus the ratios might be overestimated. On the other side contamination is not taken into account here. These membranes are not atomically clean but are rather covered in amorphous contamination on both sides. This leads to an underestimation of the ratios.

For HAADF the comparison of the intensities of atomic columns is not as straightforward since the atomic columns consisting of 3 carbon atoms are not resolved in the images that were analysed. Also subtracting the background is not as easy as during the session only one image of vacuum was taken, figure 4.12 (b). However, the background level in this image is negative and therefore it was not used for background subtraction. Here we assume that filtering the image reduced the background subtraction enough to just compare the ratios of the intensities of a 6 carbon atom column and a krypton atom. The ratio between the carbon intensities and the krypton intensity varies between

$$ratio_{exp-HAADF} = 1 : 3.74 \text{ and } 1 : 4.16 \tag{4.7}$$

depending on the peak that is used for the intensity of the carbon column which is quite close to the simulated values. Here no background subtraction was done. Also contamination is not taken into account which leads to an underestimation of the ratio. Also whether or not the krypton atoms are on top of an atomic column of carbon or not is not taken into account in any of these comparisons. The contrast between carbon and krypton in the images is lower than what would be expected from the simulations. This could be caused by contamination, which decreases the ratio, or thermal vibration of the krypton atoms as they would not be in a solid phase if it were not for the pressure exerted by the graphene layers.

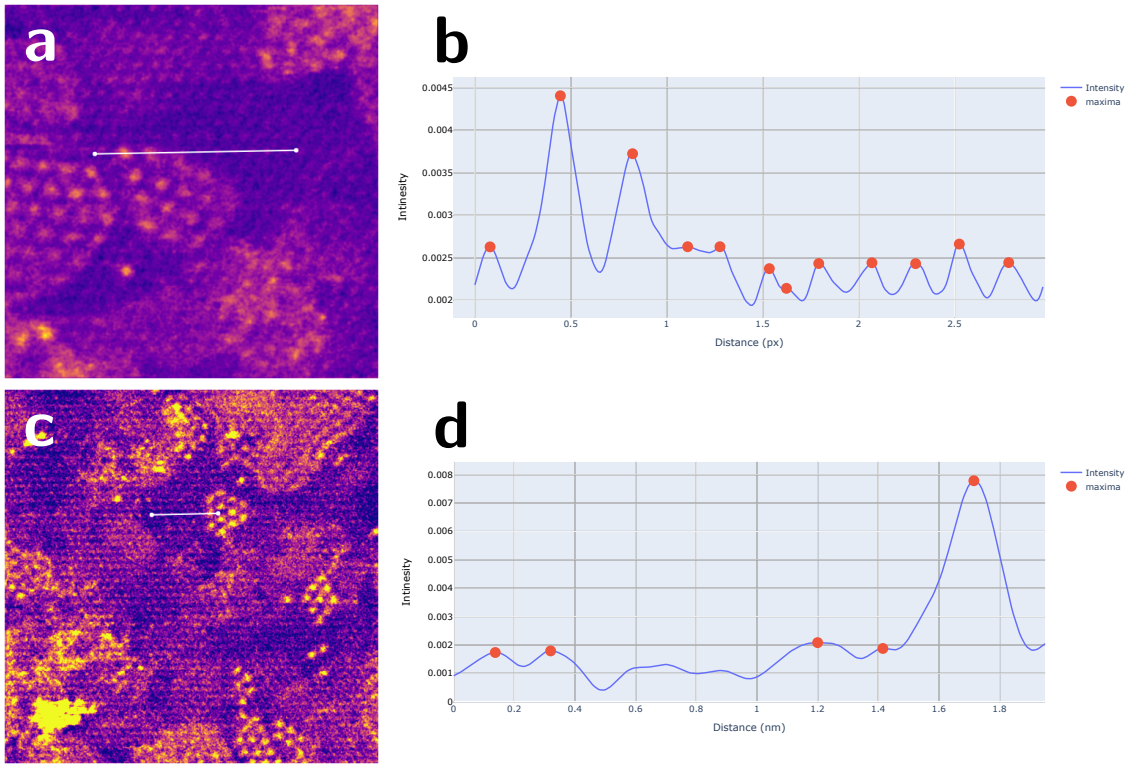

Figure 4.20: (a) & (c) filtered MAADF & HAADF images (with line profiles) used for estimating the intensity ratio between carbon and Krypton, (c) & (d) Intensities along these line profiles.

4.5 Estimation of implantation depth

For understanding the implantation process, SRIM simulations were carried out. The projected range of xenon, krypton and argon and was estimated using the "Stopping/Range Tables" module. The result of these ions impinging into graphite, AB stacked graphene, can be seen in figure 4.21. The projected range, or implantation depth, is plotted against the ion energy. If ions are to be stopped in a sample of less than 5-layers thickness, energies lower than approximately 400 eV should be used.

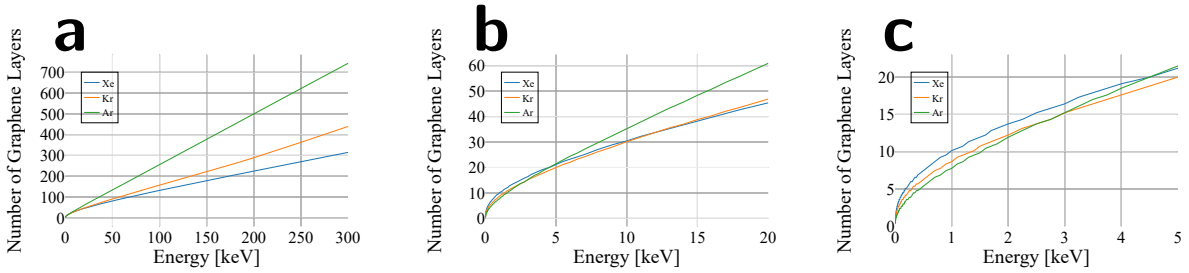

Figure 4.21: Projected range of Xe, Kr and Ar in Graphite. The implantation depth is displayed as a function of energy. The values were calculated using the "Stopping/Range Tables" module of SRIM.

However, these results are not very accurate as explained in the methods. For the comparison to experiments, a more accurate implantation simulation was carried out using the TRIM (transport of ions in matter) module. This program was written for estimating implantation depths for bulk samples and therefore the program cannot directly be used for 2D systems. However, the results can still be useful.

100 eV Kr^+ was irradiated onto graphite of varying thickness. The parameters used in the simulation were as follows: carbon with an atomic mass of 12.01 amu was used as the target. The density of graphite was 2.26 g/cm^3 and the structure had a compound correction factor of 0.8684006. The displacement energy of the carbon atoms was 28 eV, the lattice binding energy was 3 eV and the surface binding energy 7.41 eV. Single charged Kr with an atomic number 36 and a mass of 83.912 amu was used.

One layer of graphite has a thickness of 6.7 Å. The irradiation was simulated for a thickness of 14 Å(corresponding to four graphene layers) 21 Å(corresponding to three graphite or six graphene layers) and 41 Å(corresponding to six graphite or twelve graphene layers). The damage mode used for the calculation was "Surface Sputtering / Monolayer Collision Steps" as recommended by the program, which provides the most reliable results. A total of 10,000 impinging ions were calculated for all three cases. The stopping power version was SRIM-2008. Figure 4.22 (a) – (c) show the ion tracks in the material. Every red dot corresponds to a vacancy created by the impinging ions, the green dots correspond to vacancies caused by recoiling carbon atoms. Panels (d) – (f) show the number of implanted atoms. As can be seen, in a 4-layer thick graphene flake, no ions are implanted, whereas in the 6 layer thick flake, a large part of the distribution is implanted. For the 12-layer thick graphene, all ions are implanted. The results also show that

not all ions are stopped between the same layers.

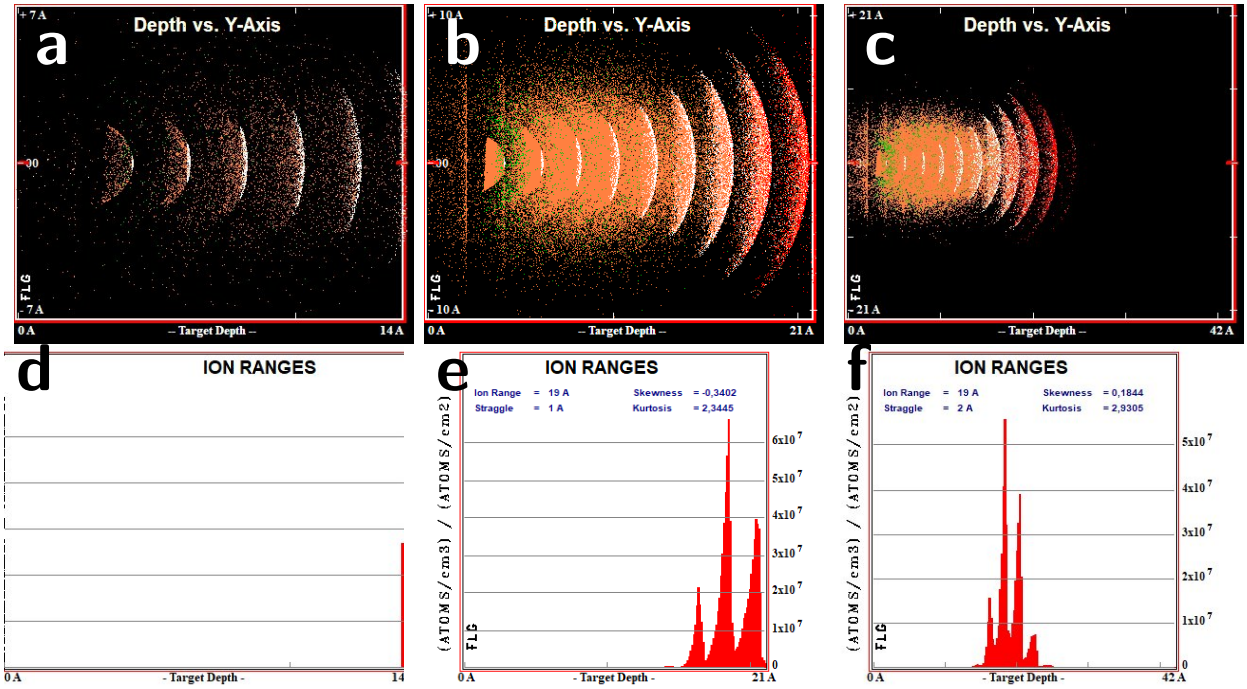

Figure 4.22: (a)-(c) shows a two dimensional projection of the collision cascade of the impinging particles. Every time there is a vacancy created due to a collision there is a red dot. (d)-(f) Shows the ion distribution in the materials. When multiplied with a dose in atoms/cm^2 the implanted atoms can be directly calculated. (a) & (d) show the results for a thin piece of graphite (4 layers, 14 Å). (b) & (e) show the results for a piece of graphite roughly the same thickness as sample Hel 37 (6 layers, 21 Å). (c) % (f) show the results for a thicker piece of graphite (12 layers, 42 Å)

4.6 Other implantations

Although many more samples were irradiated than the ones shown also he results of these irradiations will be mentioned very briefly as they are not the topic of this thesis. Silver clusters were found on the silver irradiated samples from Helsinki I & II. Gold clusters were found in Pt irradiated samples from Helsinki II. The gold atoms were most likely sputtered from the gold TEM sample holder during the irradiation. Most samples from Helsinki III have not yet been analysed.

Chapter 5

Discussion

Up until now the scientific background, the experiments conducted, the analysis and the results have been discussed. In this chapter the results are to be interpreted and put into perspective. At the end, future research will be proposed.

5.1 Choice of few layer graphene samples

Two kinds of TEM grids were used, Holey Carbon Quantifoil Gold Grids, referred to as standard TEM grids, and SiN grids. SiN grids are more expensive with the advantage of being more stable, so shooting the sample with a laser does not affect it as much, and the disadvantage that tuning the microscope with them is harder. However, exfoliated samples can only be transferred onto standard TEM grids with the methods used. Since exfoliated samples have the advantage of varying thicknesses, which was the key element for the success of the implantation, exfoliated samples on standard TEM grids were the samples of choice for this study with the disadvantage of the sample area being relatively small compared to CVD samples.

Most irradiated samples were exfoliated FLG flakes with the addition of some custom-made double-layers on standard TEM or SiN grids. Having samples of varying thickness was crucial for the success of this work since the exact implantation energy window for free-standing bilayers is still unknown for all ions. Determining this will be a task for the future if structures are to be created more systematically in a more controlled manner. It is obvious that if a sample's thickness varies from one to six layers, the chance of finding implanted atoms is significantly higher. When analysing the irradiated samples from Helsinki I, this was realised when argon was detected in thicker FLG flakes using EDX. Also, one can learn about the implantation process itself by analysing the presence of vacancies and implanted atoms as a function of thickness, which is something that could be done in the future.

5.2 Ion implantation set-up

In the methods chapter the implantation set-up for our experiments is described in detail. However, it proved to be far from optimal. Although being developed and built for energies ranging from 20 kV to 500 kV, we used the implanter for much lower energies, down to 20 eV. For these energies the dose as well as the energy of the implantation is not very well set. Combined with the small size of the samples, this introduced many uncertainties to our experiments. We tried to take this into account by conducting the experiments with as much care as possible and collecting as much information as we could to increase the reproducibility. The reasons for uncertainty we identified will be discussed in the following.

5.2.1 Dose

The dose for noble gas irradiation was chosen to be be approximately $10^{15}\frac{\text{ions}}{\text{cm}^2}$ since for the samples with lower doses almost no effect was observed. Assuming that at this dose all ions are implanted this would result in 10 ions per nm^2 – a number definitely observable under the microscope – compared to roughly 38 atoms per nm^2 in a monolayer of graphene. Even if half of the ions passed through the material, the effect would still be observable. Actually, if the implantation window is to be found more accurately the dose should be decreased, at least for krypton, due to the high lattice constant if one wants to observe crystalline phases, as the clusters tended to be more and more liquid like with increasing size.

5.2.2 Vacuum in the target chamber

The pressure during the implantation should be as low as possible because:

- The ion beam should not pin down atoms and molecules from within the vacuum onto the sample.
- With energies in the order of few eV, the ion beam interacts elastically and inelastically with the residual atoms and ions in the chamber and might get stopped along the way.
- As the deceleration lens is at a potential of 20 kV, the number of sparks decreases with the quality of the vacuum, which provides a more stable experimental set-up.

As most of the samples were not a lot dirtier than non irradiated samples, the vacuum during the experiments the vacuum was apparently good enough to not have made a significant difference in the irradiation.

5.2.3 Specifics of the samples irradiated during IRR3

Since we wanted to obtain cleaner samples for the microscopic analysis, the heating system was used during the irradiation. This became the major bottleneck in the irradiation experiments, as it required the Faraday cup behind the target chamber to be replaced by an electrical feedthrough for the lamps. This meant that for every irradiation, first the ion beam had to be created, focused and aimed at the last Faraday cup, then the stopping voltage had to be calibrated, after that the feedthrough had to be changed, which meant changing parts in the irradiation chamber, and then the samples had to be heated for long enough so that the vacuum would be adequate with the temperature still being as high as possible. This process took at least one day per sample leaving out failures of different parts, which slowed down the overall progress even more.

The heating time was kept around one hour for most samples, thus the maximum temperature our samples were baked at with was most likely below 400 °C. Measuring the temperature during the irradiation was not possible in this set-up. Heat loss via the sample holder was immense as the entire chamber heated up to almost 100 degrees. The sample holder was made from aluminium and the lamps were not very well collimated and focused which limited the maximum temperature that could be reached. The outside of the implantation chamber was at roughly 90 °C after one hour of heating.

5.2.4 Deceleration lens and stopping voltage

The stopping voltages for the different ion irradiation experiments were given in the results section and are summarized in figure 5.1, where they have been plotted against the atomic mass of the most abundant isotope. It is surprising that the stopping voltages differ for different ions since all the ions are accelerated to the same energy, 20 keV. A systematic difference between the two ion sources, gases and metals, would be explainable. However, in principle, the beam should have the same energy for all ions as they get extracted by the same voltage. We were not able to find an explanation for the differences, though when the irradiations were carried out with the most steps and the most accurate documentation, i.e. during the last experiments, the stopping voltages were all pretty much the same. This could imply that the experiments where the stopping voltage differed from 20 kV were wrong as they were not carried out as cautiously. However, the stopping voltage for Ag was consistently 20.172 kV for IRR1 & IRR2. The stopping voltage for Ag during IRR3 was 20.018 kV. If we assume the third calibration of the deceleration lens to be correct, then any energy below 150 eV from the first two experiments should not have been able to reach the sample. However, we did find Ag on samples irradiated at 60 eV. Thus, nothing conclusive can be said about the energies of the first two rounds of implantation experiments.

The stopping voltage during the third irradiation was consistently around 20 kV for all elements, except for manganese, where only on the 2nd try the stopping voltage was around 20 kV. The stopping voltages during the first and second irradiations show more variation. The lens was the same for all implantation experiments. However, the contacts had to be changed between

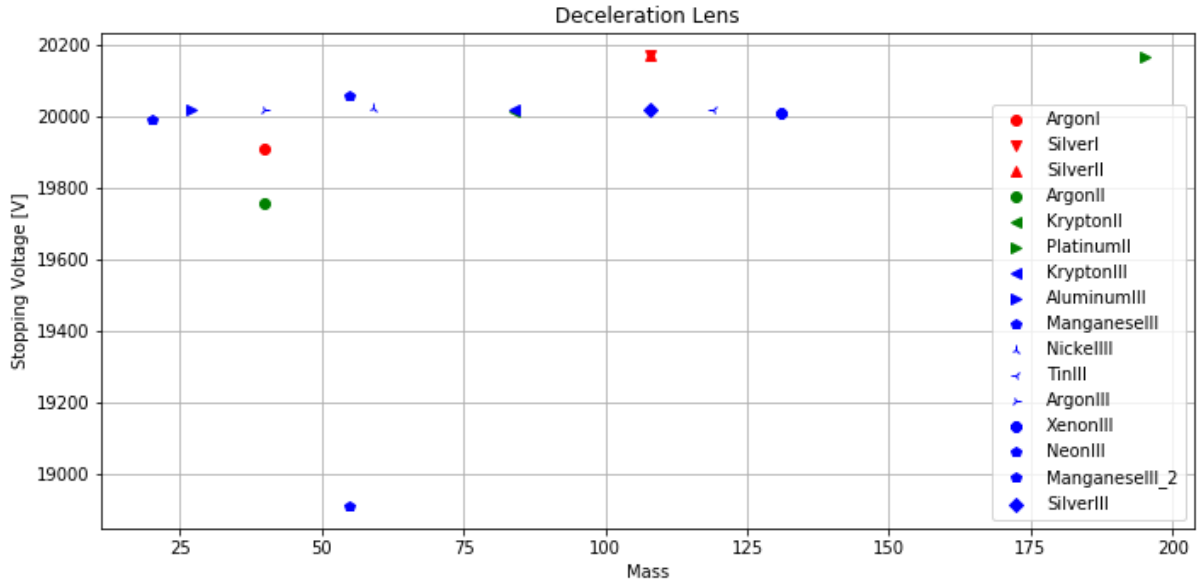

Figure 5.1: Stopping voltage as a function of the mass of different ions. Data from IRR1 is plotted in red, IRR2 is plotted in green and IRR3 is plotted in blue.

IRR2 & IRR3 as they melted during the first heating tests. This should not have resulted in a change of the stopping voltage. What we can say is that the lens exhibits voltage steps of 5 V, which appears to be the step size of the power supply.

5.2.5 Inhomogeneity of the irradiation on the sample

In one Al irradiated CVD sample, a high variation of deposition of material was noticed over the sample. The deposited material was not confirmed to be Al. However, if it had been confirmed this would have implied an inhomogeneous irradiation of the samples over one TEM grid. This would be highly problematic given that most implantations are conducted using exfoliated samples, which are very small compared to the entire grid. However, since KIIA does not have precise enough electronics to form a very sharp probe and since this has not been noticed in other experiments so far, we assume the irradiation to be homogenous across the sample. The material deposited on parts of the Al irradiated sample could have gotten there in various ways.

5.2.6 Sparks from the deceleration lens

Sparks between the deceleration lens and the target chamber change the stopping voltage and thus the energy of the ion beam hitting the sample. This change in bias only lasts for a very short time, and thus only few ions with higher energy should be able to reach the sample. Still, we wanted the set-up to be as stable as possible during the experiment. Also very few high energy ions can still cause high damage to the sample and destroy an experiment. Under normal conditions there were very few sparks, less than one per irradiation. However, when the lamps of the heating system were turned on, there were significantly more sparks, independently of

the vacuum level inside the chamber. We could not find a conclusive answer as for why, but a possible explanation is, that electrons were emitted from the lamp filaments. The electrons then got accelerated towards the high potential at the sample holder and lens and thus caused sparks. This would be consistent with the observation of more sparks at higher currents through the lamps.

5.2.7 Destruction of the deceleration lens

After the third set of irradiations, the deceleration lens was found to be heavily damaged, see figure 5.2. Hopefully, the damage occurred during the last experiment, where the heating system was turned on for almost 12 hours, compared to the normal 30 – 90 minutes, due to a CO_2 alarm in the lab. If the damage occurred before the last irradiation, this would imply that more irradiations done during IRR3 could show a systematic error due to the lens being slightly off-axis caused by the melted parts. This is hard to judge as most samples irradiated during that time have not been analysed yet. However no damage to the lens was noted before the last night.

Figure 5.2: Photographs of melted ceramic pieces in the deceleration lens taken in October 2019.

5.3 Self written code

Developing the tools for analysis yourself has advantages and disadvantages. The biggest advantage is, that one knows accurately what is happening to the data. The understanding of what the implemented filters actually do came with implementing and testing them on different images. Another advantage is that the tools are customized to the problem and can easily be developed further. On the other side they are not very universal and one has to think about everything and compare the results to standard software. At the end of the day the hope is, that the time for processing images, mostly laborious, boring and annoying, decreases so much that in the end it was more time efficient. If that is not the case, then at least writing code is entertaining[1]. Also one does not need to look for workarounds if some programs do not work on some computers, since, if Python is used, the same environment can be created easily on different platforms. The start of the development was actually when the double Gaussian filter plugin did not work on

[1]At least more entertaining than writing a thesis.

the device used for the data analysis. Overall, fixing the bug and doing the analysis by hand in imageJ[2] would have probably costed less time, but hopefully, over a longer period of time, writing the code will pay off. In the very least, the author learned a lot about plotting data and writing code that fulfils it's purpose. The most difficult thing about doing data analysis with self-written code is the question on when to stop optimizing the code and when to actually start doing data analysis. *"An artist never completes a work - they merely let it go."* [85] This also applies to writing a masters thesis.

5.4 Discussion of the microscopic analysis of the irradiated samples

The selection of irradiation energies was based on a more or less educated guess. In retrospect, a more thorough literature research should have been conducted. Studying the irradiation effect of metals is somewhat easier than that of noble gases since metals form bonds and stick to a sample and the contamination. Inert gases do not since they are chemically inert and – unless trapped between the layers – do not stay with the sample. From the samples irradiated during IRR1 silver clusters were found on the irradiated samples. We assume we deposited them on the surface and they then migrated until forming clusters.

A mistake made during the first experiments was to only transfer and use bilayer samples, or at least to only note their positions on the TEM grids. The main reason for success with krypton implantation was that we had a multi-layer sample with thickness up to six layers.

5.4.1 Implantation of argon during IRR1 and consequences

When looking for argon in the irradiated samples of IRR1, we were not very successful. Some bright atoms, which were moving, were found in the sample but we were unable to get a proper EELS signal from them and also the resolution of the images was too low for proper analysis. Judging the atomic species using the contrast is not straightforward as the samples were mostly bilayer and sometimes not AB stacked. As explained in the methods section, the difference in contrast is given by the difference in the atomic number or number of protons in the nucleus. Most bright atoms in FLG samples are known to be silicon. The atomic numbers of silicon and argon are $Z_{Si} = 14$ and $Z_{Ar} = 18$, which would be easy to tell apart as argon would be around twice as bright as silicon. Taking into account that implanted krypton shows a lower contrast to the background in real microscopy images compared to simulated ones the same is expected for implanted argon. One explanation for the lower than expected intensity of krypton could be thermal vibrations. As Kr has a higher melting temperature than Ar it could be more stable in a graphene sandwich and thus the intensity of argon could be even lower, relative to the FLG. Thus

[2] https://imagej.nih.gov/ij/

we expect argon to be harder to detect than krypton, however similar patterns as for krypton should form. Summarized, we are convinced, that we did not manage to implant argon into the thin flakes we checked. However, when using EDX, argon was detected in a thicker flake in Nottingham. This lead to the idea that exfoliated samples with varying thicknesses should be used to see whether we shoot through a bilayer but not through a trilayer and so on. Also we decided to use krypton since it has a higher nuclear charge, which should make it easier to detect in the microscope. Also it was decided, after destroying a sample with a laser, that some CVD samples should be on SiN sample holders as they can be cleaned more easily without making the sample unusable.

Since graphene is very stable, the density of hetero-atoms is usually very low, especially in exfoliated graphene. It has been shown, that if some atoms are ejected from the lattice, the vacancies sometimes get filled by other atoms [86]. Thus hetero-atoms are an indication for irradiation damage occurring to the sample. Figure 4.1 on page 54 shows images of monolayers with hetero atoms in the lattice. These are examples of the images with showing irradiation damage, only covering a very small area of the sample. Therefore, drawing a conclusion from these images is hardly possible. The stopping voltage for this experiment was 19908 kV, which is 100 eV lower than what would be expected. If there was a problem with the calibration this would mean that the energy of the argon ions could have been around 150 eV – which we expect to be too high for implantation.

5.4.2 Observed krypton structures

In the images shown in section 4.3 krypton clusters can be found quite easily, which strengthens our believe, that we did not find argon in the previously implanted samples. First the distance between krypton atoms in the newly found structures was estimated to be around 373 pm, which is shorter than double the van der Waals radius of krypton atoms, 202 pm, but longer than the lattice constant of graphene, i.e. the distance between two hexagons, being 246 pm. We thus believe that the atomic surrounding does not play as important a role as the pressure exerted between the layers. To get an idea about the stability, some simulations were done by a colleague. The result was that krypton is not held in place by vacancies but rather the energetically best place is the middle of the hexagon. In reference [21] thermal diffusion is described to be frustrated by the strain field of the encapsulating graphene layers until the temperature of the sample is elevated to 873 K. In our images we did se some dynamical behaviour but we assume it to have been triggered by the electron irradiation.

The time series displayed in figure 4.9 was not entirely taken on purpose. The times between the images vary so much due to the fact that between the images we tried to obtain EELS spectra of the crystals. The signal obtained from the small clusters was very weak, however figure 4.11 shows an EELS spectrum of a krypton crystallite where, after subtracting a reference spectrum, a faint $M_{4,\,5}$ edge is visible. After lasering the sample krypton diffused into large pockets where a clear EELS spectrum could be obtained which confirms the successful implantation of krypton

into graphene.

As for the structure it can be seen in most images that for smaller clusters the atoms are quite stationary/very distinct whereas in bigger crystallites they appear blurred out, and are thus more mobile, see figures 4.13 and 4.15. The crystallites appear to not be crystalline any more after reaching a certain size. Also the edges of the bubbles look very distinct, invoking the idea of a row of atoms forming the edge of the bubble. These features are visible in figures 4.13 and 4.15. Also the crystallites sometimes appear in strange circular forms as shown in figure 4.17. In all images a characteristic gap appears between some crystals, figure 4.16 shows some of them. We expect this gap to occur due to the fact that krypton atoms are stuck between different layers being pushed together by the van der Waals pressure and stabilizing each other. This is schematically illustrated in figure 5.3 and fits the measured distance in the results. There could also be two characteristic distances, for clusters with two layers in between, however estimating the exact distance is difficult and statistics are not good enough to conclude something.

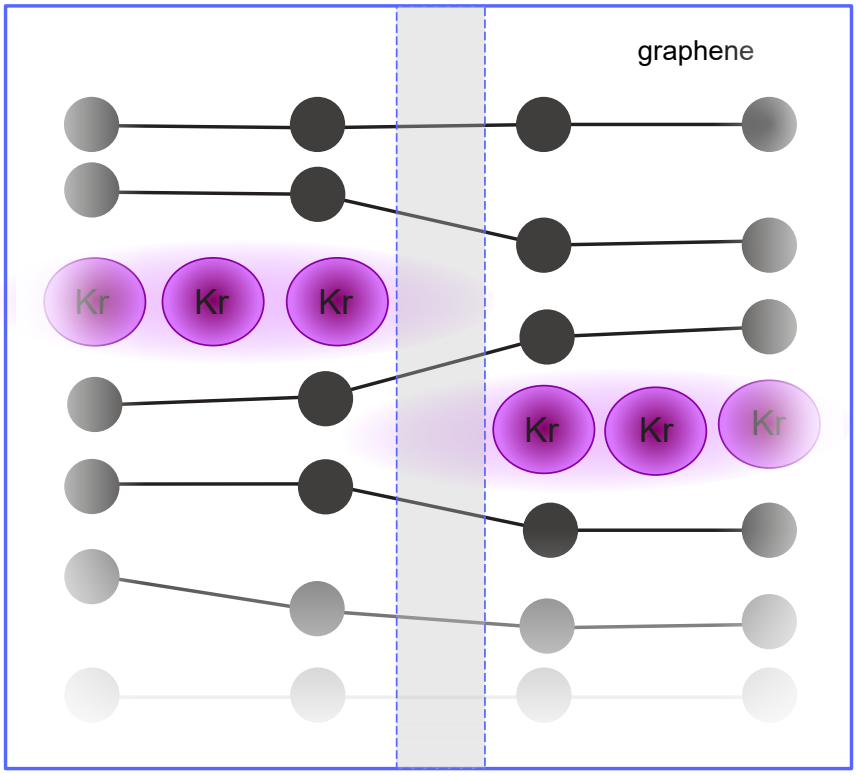

Figure 5.3: Schematic illustration of characteristic gap between two Kr crystallites stuck between different layers. Note that none of the distances between atoms are to scale. Illustration: Alberto Trentino, adapted by the author.

Judging from the intensities of the implanted hetero-atoms alone we can not say that the implanted species are krypton, as the method has various obstacles to being accurate, but combined with the mentioned spectra from an individual cluster as well as from the pockets after lasering and combined with the matching lattice constant we can be certain to have implanted krypton in FLG and we can be certain that the observed structures are indeed formed by implanted krypton. What we can tell, however, is that the intensity for the observed clusters is to low to originate from more than one layer of atoms which indeed proves the successful creation of a two-dimensional

noble gas.

5.5 Summary and plans for the future

The overall goal of this work was to study the structure of implanted noble gas bubbles into layered host materials and thus create two dimensional noble gases. For that, creating these structures in a controlled way is necessary. The energy window for krypton implantation into five and six layers thick graphene has been found in this study. The next step will be to narrow down the implantation window for krypton, and other noble gasses, into bilayer graphene as these samples will be easier to analyse and the structures can be controlled more easily. It is unknown if the implantation into double layers (stacked CVD samples) is possible. This is one of the questions that should be answered in future work. Also the implantation windows for other noble gases like Ne, Ar and Xe into the systems described above are to be found. It would be extremely interesting to see whether it is possible to implant and image helium, as it would be the lightest atom ever imaged in an electron microscope. Currently, we have samples where we tried to implant Ne, Ar, and Xe into FLG. These samples will be analysed in the near future. Implanting inert gases into nanotubes is also one possibility that can be looked into.

We observed the formation of two-dimensional clusters whose stability strongly depend on the local surrounding of each cluster but which are stable enough to be imaged using 60 keV electrons. We assume the interactions of these crystallites to be purely van der Waals which is supported by the long lattice constant. We conclude that our approach worked and that we created two-dimensional noble gas crystals, which are stable at room temperature under the electron beam. To our knowledge, it has so far not been possible to directly image such noble gas crystals in an electron microscope. Thus, in the presence of graphene encapsulation, these at room temperature inert atoms create structures with a remarkable stability under the 60 keV electron irradiation inside the microscope vacuum. Even individual krypton atoms can be resolved as shown in various images in the previous chapter. The krypton crystallites appear in solid and liquid phases.

This system still has many open questions to answer. Both, the effect the irradiation has on graphene, and the newly found van der Waals crystals should be studied to get a deeper understanding of the implantation process and of the physical environment the crystals are in. The next goal is to understand the formation dynamics of the newly observed crystals. For that additional analysis of the existing structures is required. If the images are good enough, the deformation of crystal structure around the bubbles will be investigated as well as the dependence of the orientation of the Kr crystals on the graphene/graphite lattice. The characteristic gap between crystallites will also be investigated more thoroughly. It should be quantified why some Kr atoms appear brighter than others in the same cluster, as well as the critical size clusters need to reach to loose their two dimensional structure. The number of atoms in a liquid can be determined using Fourier filters to remove the graphene lattice and knowing the intensity

of individual krypton atoms. The interatomic distance of krypton atoms in clusters should be measured dependent on the cluster size to see whether there is a systematic behaviour.

One long term goal is to observe the dynamics of the system and find the diffusion barriers of individual atoms between the layers. For that, heatable sample holders are one possibility. Another thing that should be done is to check whether there are interesting electronic excitations in the 2D noble gas clusters. For that, a collaboration with Oakridge National Laboratory or the Humbold Universität Berlin would be interesting as they have the means to do monochromated EELS, which can be used for probing these excitations.

Another set of experiments that could be carried out is to check how much material can be implanted into a bilayer. Private companies are currently building satellites with electric propulsion systems, which use krypton ions as propellants. Since lithium between bilayer graphene has a very dense stacking and the distance between the krypton atoms in our 2D crystal also appears to be shorter than in normal van der Waals crystals, we could try to find out how much krypton we can pack between the layers before the structure breaks. That way, an ultra-light krypton tank could be built. Of course, it remains an open question whether the krypton could be extracted at some point, but it would be an extremely light tank with very high fuel density, which are both important features for space technology.

This thesis was not able to answer all questions arising from this new form of inert gas crystals, but it showed its interesting and unexpected properties. We provided a comprehensive description of the structure, growth and stability of 2D noble gas crystals. It is a key step forward in the aim of implanting hetero atoms into graphene-like systems and provides many new venues for future research.

Appendix A

data_analysis_file

data_analysis_file_appendix

June 24, 2020

In [ ]:
```
from __future__ import print_function
from ipywidgets import interact, interactive, fixed, interact_manual
from PIL import Image
import numpy as np
from plotly import graph_objs as go
from imageanalysis import plotimage_contrast, plotimage, plotline, tripleplot, triplep
from scipy.signal import find_peaks
from scipy import fftpack, ndimage
import os
import ipywidgets as widgets
from PIL.TiffTags import TAGS
from collections import OrderedDict

import re
```

In [ ]:
```
# defines the functions for the drop down menu
source="./images/Krypton/"
def get_options():
    opts = os.listdir(source)
    return opts

def get_options2():
    opts = os.listdir(source+select_folder.value)
    return opts
```

In [ ]:
```
#opens a drop-doun menu to select the folder
select_folder = widgets.Select(options = get_options(), description = 'Please select f
display(select_folder) #display the drop-drown menu
```

In [ ]:
```
select_image = widgets.Select(options = get_options2(), description = 'Please select i
display(select_image) #display the drop-drown menu
```

1 the image selected in the drop-down is imported

In [ ]:
```
im = Image.open(source+select_folder.value+"/"+select_image.value)
```

```
        #rotates the image, so that it is the same as in fiji
        im_array_rot = np.array(im)
        x,y = im_array_rot.shape
        im_array=np.zeros((x,y))
        for i in range(x):
            for j in range(y):
                im_array[i,j] = im_array_rot[x-i-1,j]
                im_array = im_array[0:x,0:y]
```

2 rebins the image to reduce the time

```
In [ ]: print(len(im_array))
        #im_array=rebin(im_array,(512,512))
```

3 reads out the scale, the time the image was taken and the detector

```
In [ ]: with im as img:
            meta_dict = {}
            for key in img.tag:      # don't really need iterkeys in this context
                meta_dict[TAGS.get(key,'missing')] = img.tag[key]
        metadata=(meta_dict["ImageDescription"])
        x=str(metadata)
        metadata_split=x.split(", ")

        #print(x)
        print(metadata_split[4],metadata_split[5])
        detectorstamp=metadata_split[63]
        detector=(detectorstamp[17:22])

        #print(metadata_split[-1])
        timestamp=metadata_split[-1]


        a=re.findall(r'\b\d+\b', timestamp)
        time=int(a[0])+int(a[1])*10**(-len(a[1]))
        y=(a[1])

        print("detector",detector)
        print(timestamp)
        print("time",time)


        #for i in range(len(metadata_split)):
        #    print(i,metadata_split[i])
```

4 show the unfiltered image

```
In [ ]: minval=0.0000 #0.0044
        maxval=0.0190 #0.0096
        #fig=plotimage_contrast(im_array,maxval,minval, "Plasma" ) #Plasma and gray are usable
        fig=plotimage(im_array,len(im_array),"Plasma")
        #print(type(fig))
        fig.show()
```

5 here the image can be scaled

5.1 the fft is calculated, plotted and an array is selected

```
In [ ]: fft_im_array = fftpack.fftshift(fftpack.fft2(im_array))
        abs_fft=np.abs(fft_im_array)

In [ ]: figfft=plotfft(abs_fft)#, maxval, minval) #Plasma and gray are useable
        figfft.show()
```

5.2 now the maxfinder function if used to find peaks in the 2D array

```
In [ ]: neighborhood_size = 50
        threshold = 10
        maxwert=maxfinder(abs_fft,neighborhood_size,threshold)
        y=np.array(maxwert[0])
        x=np.array(maxwert[1])
        print(x,y)
        print(len(x))
```

5.3 the peaks can also be put into the image to control the outcome

```
In [ ]: figfft.add_trace(go.Scatter(mode = 'markers',
                                    x = y,
                                    y = x,
                                    marker = {'symbol': 'circle',
                                          #     'color': 'blue',
        #                                       'size': 10,
                                              'opacity': 1},
                                   # name="identified spots"
                                   ))
```

5.4 do the scaling

```
In [ ]: # calculates the radius in pixel
        maxpos=np.array([len(abs_fft)/2,len(abs_fft)/2])
        r=np.zeros(len(x))
        for i in range(len(x)):
            r[i]=np.sqrt(np.square(maxpos[0]-x[i])+np.square(maxpos[1]-y[i]))
```

```
# remove the 0
r=r[r !=0]

# calculate the radius in pixel over cycle
r_poc=len(im_array)/r

#print(r)
#print(r_poc)

#sort the radius in pixel over cycle
r_sort=np.sort(r_poc)

print(r_sort)
```

5.4.1 deleting of wrong identified diffraction spots

In [ ]:
```
r_sort[-2]=0
print(r_sort)
```

In [ ]:
```
r_sort=np.sort(r_sort)
print(r_sort)
```

5.4.2 the image is scaled by setting the number of inner and outer diffraction spots

In [ ]:
```
#takes the most inner 6 spots and calculates an average distance
#of spots
inner=6

r_first=r_sort[-inner:]
print(r_first)
r_first_average=np.average(r_first)

outer=6

#takes the second most inner 6 spots and calculates the average distance
r_second=r_sort[-(inner+outer):-inner]
print(r_second)
r_second_average=np.average(r_second)
```

In [ ]:
```
#diffraction spot close to the centre, r_close, that has a bigger value in r_poc
#it is set equal to lattice constant * sin(60ř)

gitterkonstante=0.246 # in nm

a_close=gitterkonstante*np.sin(60*np.pi/180)
px1=r_first_average/a_close
print(px1)
```

```
        # the diffraction spots further away are ste equal to lattice constant half
        a_far=gitterkonstante/2
        px2=r_second_average/a_far
        print(px2)
```

In [ ]:
```
        r_inner=(len(im_array)/np.max(r_first))
        if outer== 0:
            r_outer=len(im_array)/(px1*a_far)
        else:
            r_outer=(len(im_array)/np.min(r_second))


        print(r_inner)
        print(r_outer)
        #r_inner=12.04
        #r_outer=462
```

thus 1 nm corresponds to px1 und px2 pixel

6 now we apply a dobble gaussian filter

In [ ]:
```
        tolerace_inner=0.6 #optimized for graphene
        tolerace_inner=0.15 # optimized for krypton crystals
        tolerace_outer=1.3 # optimized for graphene
        weight=0.6 # optimized

        fim_array, fft, filter, filtered_fft = doublegaussian(im_array, r_outer*tolerace_outer
```

In [ ]:
```
        tripple=tripleplot2(fft, filter, filtered_fft)
        tripple.show()
```

In [ ]:
```
        # saves trippleplot
        #tripple.write_image("./images/Argon/Analysis-20190117-Hel-28-Ar+-50eV-dose15/exported,
```

In [ ]:
```
        # lattice impurities2 - minval 0.0, maxval 0.01 - images were made as
```

6.1 the image is plotted with the right contrast

6.1.1 unfiltered

In [ ]:
```
        #plot of the unfiltered image
        minval=0.0#0.0044
        maxval=0.12#fig=plotimage_contrast(im_array,maxval,minval, len(im_array),"Plasma")
        fig=plotimage(im_array,len(im_array),"Plasma")
```

In [ ]:
```
        fig.show()
```

6.1.2 filtered

In [ ]:
```
#plot of the filtered image
minval=0.00 #0.0044
maxval=0.014
fig=plotimage_contrast(fim_array,maxval,minval, len(fim_array),"Plasma")

fig.show()
```

6.2 we add a scale bar

In [ ]:
```
image=fim_array

px=(np.round((px1)))
bottomleft=(np.array(image.shape)/10).astype(int)
x=1

if len(image) == 64:
    height=(np.array(len(image))*0.08*x).astype(int) # 512 pixel
elif len(image) == 128:
    height=(np.array(len(image))*0.04*x).astype(int) # 512 pixel
elif len(image) == 256:
    height=(np.array(len(image))*0.02*x).astype(int) # 512 pixel
elif len(image) == 512:
    height=(np.array(len(image))*0.01*x).astype(int) # 512 pixel
elif len(image) == 1024:
    height=(np.array(len(image))*0.005*x).astype(int) # 1024 pixel
elif len(image) == 2048:
    height=(np.array(len(image))*0.0025*x).astype(int) # 2048 pixel
else:
    print(error)

length=1
scalebarlength=(length*px).astype(int)

print(bottomleft)
print(height)
print(scalebarlength)

colour="white"
#colour="black"
```

In [ ]:
```
fig.add_shape(
        go.layout.Shape(
            type="line",
            x0=bottomleft[0],
            y0=bottomleft[1],
            x1=bottomleft[0]+scalebarlength,
            y1=bottomleft[1],
```

```
                line=dict(
                    color=colour,
                    width=height
                )
            ))
```

7 the image is saved

```
In [ ]: name=select_image.value[0:-4]+"scalebar"+str(length)+colour+"with lineprofile-TESTPDFO
        print(name)
        print(source+select_folder.value+"/exported/"+name)
        fig.write_image(source+select_folder.value+"/exported/"+name, width=im_array.shape[1],
```

8 we can draw a line profile

```
In [ ]: def lineprof(data, begin, end, num, width):
            y, x = np.linspace(begin[0], end[0], num), np.linspace(begin[1], end[1], num)

            # Extract the values along the line, using cubic interpolation
            blurred = ndimage.gaussian_filter(data, sigma=width)
            line = ndimage.map_coordinates(blurred, np.vstack((x,y)))


            fig.add_trace(go.Scatter( x = [begin[0], end[0]], y = [begin[1], end[1]], line=dic
            fig.update_layout(showlegend=False)

            distances = np.array([np.sqrt(x+y) for x, y in np.power(np.vstack((x,y))[:,1:] - n
            d = np.append(np.array(0), np.cumsum(distances))

            return d, line

In [ ]: minval=0.00 #0.0044
        maxval=0.014
        fig=plotimage_contrast(data,maxval,minval, len(data)*2,"Plasma")

In [ ]: #draws a line profile with begin and endpoint begin and end, a width of width pixel an
        num = 300
        begin = (50,62)
        end = (33,59)
        width = 0.5

        #displays the line profile on the image
        d, line = lineprof(fim_array, begin, end, num, width)

In [ ]: fig.show()

In [ ]: length=1
        colour=""
```

```
In [ ]: name=select_image.value[0:-4]+""+str(length)+colour+"with lineprofiles_krypton"+".png"
        print(name)
        print(source+select_folder.value+"/exported/"+name)
        fig.write_image(source+select_folder.value+"/exported/"+name, width=len(im_array[1]), l
```

8.1 plot the line profile and identify peaks, measure the distances between them and the height of the peak

```
In [ ]: #px1=1
```

```
In [ ]: def plotline(line, x = None):
            fig = go.Figure()
            fig.add_trace(go.Scatter(
                            y = [np.average(cols) for cols in line],
                            x = x,
                            mode='lines',
                            #line=dict(color='black', width=4),
                            name="Intensity",
                            showlegend=True
                          ))

            fig.update_layout(
            width = 1024, height = 512,
            xaxis=dict(
                title="Distance (nm)",
            #    domain=[0.15, 0.7],
            ),
            yaxis=dict(
                title="Intinesity",
                titlefont=dict(
                    color="black"
                ),
                tickfont=dict(
                    color="black"
                )
            ),
        )

            return fig
```

```
In [ ]: lineprofile=plotline(line, x = d/px1)
        #print(np.average(line))
        lineprofile.show()
```

```
In [ ]: height=0.0028
        peaks, _= find_peaks(line, height)

        #saves the peaks in an array
        peak_x=d[peaks]
```

```
        peak_y=line[peaks]

        #calculates the distance in pixel between the peaks
        dist=peak_x[1:]-peak_x[:-1]
        print(dist/px1)
        print(peak_y)
```

```
In [ ]: #prints the line profile
        lineprofile.add_trace(go.Scatter(
                                          x=peak_x/px1,
                                          y=peak_y,
                                          mode='markers',
                                        #  marker_color='red',
                                          marker_size=15,
                                          name='maxima',
                                          showlegend=True
                                         )
                              )

        lineprofile.show()
```

```
In [ ]: name=select_image.value[0:-4]+""+"with lineprofile_graphene_krypton"+".pdf"
        print(name)
        print(source+select_folder.value+"/exported/"+name)
        #fig.write_image(source+select_folder.value+"/exported/"+name, width=im_array.shape[1]
        #lineprofile.write_image(source+select_folder.value+"/exported/"+select_image.value[0:
```

8.2 save the distances between the peaks

```
In [ ]: data_analysis=select_image.value[0:-4]+""+""+""+"-intercluster_dist.txt"

        entire_path=source+select_folder.value+"/exported/"+""+data_analysis

        print(entire_path)
        interatomdist_nm=dist/px1
```

```
In [ ]: f = open(entire_path,"a") #opens file with name of "test.txt"
        f.write(str(interatomdist_nm)),f.write("\n")
        f.close()
        print(i)
        i+=1
```

9 Extra stuff

9.1 make inset into the FFT

```
In [ ]: figfft.update_layout(
                legend=dict(x=0.1,y=0.9,traceorder="normal",
```

```
            font=dict(family="Times New Roman",size=20,color="black"),
            #bgcolor="LightSteelBlue",
            bordercolor="Black",
            borderwidth=1
        )
    )
```

In [ ]:
```
figfft2=figfft
```

In [ ]:
```
inset_x=0.02
inset_y=0.32

im_array2=rebin(im_array,(512,512))
figfft.add_trace(go.Heatmap(
                                z = im_array2,
                                zmax = np.min([maxval,np.max(im_array2)]),
                                zmin = np.max([minval,np.min(im_array2)]),
                                zauto=False,
                                showscale=False,
                                colorscale = "plasma",
                                xaxis='x2',
                                yaxis='y2',
                                #showlegend=False
                    ))
figfft.update_layout(
                        # width = size,
                        # height = size,
                         autosize=True,
                         margin=go.layout.Margin(
                                                 l=0,
                                                 r=0,
                                                 b=0,
                                                 t=0,
                                                ),
                         xaxis2=dict(domain=[inset_x, inset_y],
                                     anchor='y2'
                                     ),
                         yaxis2=dict(domain=[inset_x, inset_y],
                                     anchor='x2'
                                     ),
                                )


figfft.update_xaxes(showticklabels=False)
figfft.update_yaxes(showticklabels=False)
```

In [ ]:
```
#figfft.write_image("./images/Argon/Analysis-20190117-Hel-28-Ar+-50eV-dose15/exported/
```

9.2 Cut out a part of an image and plot it

```
In [ ]: start=[365,1540]
        area=2**7
        print(area)

In [ ]: data=fim_array[start[1]-area:start[1],start[0]:start[0]+area]

In [ ]: fig.add_shape(
                go.layout.Shape(
                    line=dict(color="red"),
                    type="rect",
                    x0=start[0],
                    y0=start[1],
                    x1=start[0]+area,
                    y1=start[1]-area,
                ))

In [ ]: def plotimage_subplotcontrast(im_array, maxval, minval, size, colorscale=None):
            fig = go.Figure()
            fig.add_trace(go.Heatmap(
                                        z = im_array,
                                        zmax = maxval,
                                        zmin = minval,
                                        zauto=False,
                                        showscale=False,
                                        colorscale = colorscale,
                            ))
            fig.update_layout(
                                width = size,
                                height = size,
                                autosize=True,
                                margin=go.layout.Margin(
                                                        l=0,
                                                        r=0,
                                                        b=0,
                                                        t=0,
                                                       )
                             )
            fig.update_xaxes(showticklabels=False)
            fig.update_yaxes(showticklabels=False)
            return fig

In [ ]: subplot_maxcontrast=np.max(fim_array)
        subplot_mincontrast=np.min(fim_array)
        fig2=plotimage_subplotcontrast(data,subplot_maxcontrast,subplot_mincontrast,len(data),'
        fig3=plotimage_contrast(data,subplot_maxcontrast,subplot_mincontrast,len(data),"Plasma'

        #fig=plotfft(data) #Plasma and gray sind die stufen die man verwenden kann
```

```
        fig2.show()
        fig3.show()
```

In [ ]:
```
        #name="halfcicrle"+str(i)+".png"
        #fig2.write_image(source+select_folder.value+"/exported/subplots/"+"bright_"+name, wid
        #fig3.write_image(source+select_folder.value+"/exported/subplots/"+"dark_"+name, width=
        #i+=1
```

Appendix B

imageanalysis

imageanalysis_appendix

June 24, 2020

In [ ]:
```
import numpy as np
from plotly import graph_objs as go
from plotly.subplots import make_subplots
from math import floor
from scipy import fftpack, ndimage
from scipy.signal import find_peaks
import scipy.ndimage.filters as filters

def maxfinder(data,neighborhood_size,threshold):
    data_max = filters.maximum_filter(data, neighborhood_size) #legt fest was die maxi
    maxima = (data == data_max) #stellt fest, ob ein maximum vorliegt oder nicht
    data_min = filters.minimum_filter(data, neighborhood_size) #legt fest was die mini
    diff = ((data_max - data_min) > threshold) #legt den gröenunterschied von maximum
    maxima[diff == 0] = 0
    labeled, num_objects = ndimage.label(maxima)
    slices = ndimage.find_objects(labeled)
    x, y = [], []
    for dy,dx in slices:
        x_center = (dx.start + dx.stop - 1)/2
        x.append(x_center)
        y_center = (dy.start + dy.stop - 1)/2
        y.append(y_center)
    ausgabe=[x,y]
    return ausgabe

def plotimage_contrast(im_array, maxval, minval, size, colorscale=None):
   # im_array=np.array([np.min([maxval,i]) for i in im_array.flatten()]).reshape(im_ar
   # im_array=np.array([np.max([minval,i]) for i in im_array.flatten()]).reshape(im_ar
    fig = go.Figure()
    fig.add_trace(go.Heatmap(
                              z = im_array,
                              zmax = np.min([maxval,np.max(im_array)]),
                              zmin = np.max([minval,np.min(im_array)]),
                              zauto=False,
                              showscale=False,
                              colorscale = colorscale,
                  ))
```

```
    fig.update_layout(
                        width = size,
                        height = size,
                        autosize=True,
                        margin=go.layout.Margin(
                                                l=1,
                                                r=1,
                                                b=1,
                                                t=1,
                                               )
                    )
    fig.update_xaxes(showticklabels=False)
    fig.update_yaxes(showticklabels=False)
    return fig

def plotimage(im_array, size, colorscale=None):
    fig = go.Figure()
    fig.add_trace(go.Heatmap(
                             z = im_array,
                             showscale=False,
                             colorscale = colorscale,
                  ))
    fig.update_layout(
                        width = size,
                        height = size,
                        autosize=True,
                        margin=go.layout.Margin(
                                                l=1,
                                                r=1,
                                                b=1,
                                                t=1,
                                               )
                    )
    fig.update_xaxes(showticklabels=False)
    fig.update_yaxes(showticklabels=False)
    return fig

def plotfft(im_array, colorscale=None):
   # im_array=np.array([np.min([maxval,i]) for i in im_array.flatten()]).reshape(im_ar
   # im_array=np.array([np.max([minval,i]) for i in im_array.flatten()]).reshape(im_ar
    fig = go.Figure()
    fig.add_trace(go.Heatmap(
                             z = im_array,
                             showscale=False,
                             colorscale = [[0, "rgb(255,255,255)"], [0.003, "rgb(0, 0
                  ))
    fig.update_layout(
                        width = 512,
```

```
                    height = 512,
        margin=go.layout.Margin(
                                                l=1,
                                                r=1,
                                                b=1,
                                                t=1,
                                               )
    )
    return fig

def plotline(line, x = None):
    fig = go.Figure()
    fig.add_trace(go.Scatter(
                    y = [np.average(cols) for cols in line],
                    x = x
                ))

    return fig

def plotline_EELS(line, x = None):
    fig = go.Figure()
    fig.add_trace(go.Scatter(
                    y = [np.average(cols) for cols in line],
                    x = x,
                    mode='lines',
                    line=dict(color='black', width=4)
                ))
    fig.update_layout(xaxis_title="Energy loss (eV)",
                yaxis_title="Counts",
                font={'family': "Times New Roman, serif", 'size': 32},
                paper_bgcolor='rgba(0,0,0,0)', # transparent background
                plot_bgcolor='rgba(0,0,0,0)',
                template = 'none',
                #width = 1024, height = 768,
                xaxis=dict(showgrid=False, zeroline=False),
                yaxis=dict(showgrid=False, zeroline=False, showticklabels=False),
               )

    return fig

def tripleplot(fft, filter, filtered_fft):
    fig = make_subplots(rows = 1, cols = 3, column_widths = [0.3, 0.3, 0.3], row_height
    fig.add_trace(
        go.Heatmap(
                    z = np.abs(fft),
                    colorscale = [[0, "rgb(0, 0, 0)"], [0.005, "rgb(255, 255, 255)"],
        ),
        row = 1,
```

```
            col = 1
        )
        fig.add_trace(
            go.Heatmap(
                        z = filter,
                        colorscale = 'gray'
            ),
            row = 1,
            col = 2
        )
        fig.add_trace(
            go.Heatmap(
                        z = np.abs(filtered_fft),
                        colorscale = [[0, "rgb(0, 0, 0)"], [0.005, "rgb(255, 255, 255)"],
            ),
            row = 1,
            col = 3
        )
        fig.update_layout(width = 1000, height = 400)
        return fig

    def tripleplot2(fft, filter, filtered_fft):
        fig = make_subplots(rows = 1, cols = 3, column_widths = [0.3, 0.3, 0.3], row_heigh
        fig.add_trace(
            go.Heatmap(
                        z = np.abs(fft),
                        colorscale = [[0, "rgb(255,255,255)"], [0.005, "rgb(0, 0, 0)"], [1
                        showscale=False
            ),
            row = 1,
            col = 1
        )
        fig.add_trace(
            go.Heatmap(
                        z = filter,
                        colorscale = 'gray',
                        showscale=False
            ),
            row = 1,
            col = 2
        )
        fig.add_trace(
            go.Heatmap(
                        z = np.abs(filtered_fft),
                        colorscale = [[0, "rgb(255,255,255)"], [0.005, "rgb(0, 0, 0)"], [1
                        showscale=False
            ),
            row = 1,
```

```
        col = 3
    )
    fig.update_layout(width = 1000, height = 400)
    return fig

def doublegaussian(data, sigma1, sigma2, weight):

        # first calculate the FFT
        fft_data = fftpack.fftshift(fftpack.fft2(data))

        # next, set up xx, yy arrays to be linear indexes for x and y coordinates rang
        # from -width/2 to width/2 and -height/2 to height/2.
        yy_min = int(floor(-data.shape[0] / 2))
        yy_max = int(floor(data.shape[0] / 2))
        xx_min = int(floor(-data.shape[1] / 2))
        xx_max = int(floor(data.shape[1] / 2))
        xx, yy = np.meshgrid(np.linspace(yy_min, yy_max, data.shape[0]),
                             np.linspace(xx_min, xx_max, data.shape[1]))

        # calculate the pixel distance from the center
        rr = np.sqrt(np.square(xx) + np.square(yy)) #/ (data.shape[0] * 0.5)

        # finally, apply a filter to the Fourier space data.
        filter = np.exp(-0.5 * np.square(rr / sigma1)) - (1.0 - weight) * np.exp(-0.5 *
        filtered_fft_data = fft_data * filter

        # and then do invert FFT and take the real value.
        result = fftpack.ifft2(fftpack.ifftshift(filtered_fft_data)).real

        return result, fft_data, filter, filtered_fft_data

def scalebar(fig, bottomleft, scalebarlength, width):
    fig.add_shape(
        go.layout.Shape(
            type="line",
            x0=bottomleft[0],
            y0=bottomleft[1],
            x1=bottomleft[0]+scalebarlength,
            y1=bottomleft[1],
            line=dict(
                color="white",
                width=width
            )
        ))

    return fig

def lineprof(data, begin, end, num, width):
```

```
    y, x = np.linspace(begin[0], end[0], num), np.linspace(begin[1], end[1], num)

    # Extract the values along the line, using cubic interpolation
    blurred = ndimage.gaussian_filter(data, sigma=width)
    line = ndimage.map_coordinates(blurred, np.vstack((x,y)))

    fig = plotimage(data,len(data))
    fig.add_trace(go.Scatter( x = [begin[0], end[0]], y = [begin[1], end[1]], line = {

    distances = np.array([np.sqrt(x+y) for x, y in np.power(np.vstack((x,y))[:,1:] - n
    d = np.append(np.array(0), np.cumsum(distances))

    return fig, d, line
```

```
#this function calculates the sum of the maxima of the line profile
def optimallineprof(data, begin, end, num, width, peakhight):
    y, x = np.linspace(begin[0], end[0], num), np.linspace(begin[1], end[1], num)

    # Extract the values along the line, using cubic interpolation
    blurred = ndimage.gaussian_filter(data, sigma=width)
    line = ndimage.map_coordinates(blurred, np.vstack((x,y)))

    distances = np.array([np.sqrt(x+y) for x, y in np.power(np.vstack((x,y))[:,1:] - n
    d = np.append(np.array(0), np.cumsum(distances))

    #read out the hight of the peaks
    peaks, _= find_peaks(line, height=peakhight)
    peak_y=line[peaks]
    totalheight=np.sum(peak_y)
    return d, line, peak_y, totalheight

def opt_pos(fim_array, begin, end, num, width, peakhight, size):
    area=np.linspace(-size,size,num=2*size+1)
    heights=np.array([0,0])

    for i in area:
        for j in area:
            pos=(end[0]+i,end[1]+j)
            d, line, peak_y, totalheight = optimallineprof(fim_array, begin, pos, num,
```

```
            if totalheight > heights[-1]:
                heights=np.append(heights,totalheight)
                bestend=(end[0]+i,end[1]+j)
    #print(bestend)

    heights=np.array([0,0])
    for i in area:
        for j in area:
            pos=(begin[0]+i,begin[1]+j)
            d, line, peak_y, totalheight = optimallineprof(fim_array, pos, end, num, w
            if totalheight > heights[-1]:
                heights=np.append(heights,totalheight)
                bestbegin=(begin[0]+i,begin[1]+j)

    #print(bestbegin)
    return bestend, bestbegin

def rebin(arr, new_shape):
    shape = (new_shape[0], arr.shape[0] // new_shape[0],
             new_shape[1], arr.shape[1] // new_shape[1])
    return arr.reshape(shape).mean(-1).mean(1)
```

Bibliography

[1] Novoselov, K. S. Electric Field Effect in Atomically Thin Carbon Films. *Science* **306**, 666–669 (2004). DOI: 10.1126/science.1102896.

[2] Geim, A. K. Graphene: Status and Prospects. *Science* **324**, 1530–1534 (2009). DOI: 10.1126/science.1158877.

[3] Castro Neto, A. H., Guinea, F., Peres, N. M. R., Novoselov, K. S. & Geim, A. K. The electronic properties of graphene. *Reviews of Modern Physics* **81**, 109–162 (2009). DOI: 10.1103/RevModPhys.81.109.

[4] Lee, C., Wei, X., Kysar, J. W. & Hone, J. Measurement of the Elastic Properties and Intrinsic Strength of Monolayer Graphene. *Science* **321**, 385–388 (2008). DOI: 10.1126/science.1157996.

[5] Lee, J.-U., Yoon, D. & Cheong, H. Estimation of Young's Modulus of Graphene by Raman Spectroscopy. *Nano Letters* **12**, 4444–4448 (2012). DOI: 10.1021/nl301073q.

[6] Stolyarova, E. *et al.* Observation of Graphene Bubbles and Effective Mass Transport under Graphene Films. *Nano Letters* **9**, 332–337 (2009). DOI: 10.1021/nl803087x.

[7] Bunch, J. S. *et al.* Impermeable Atomic Membranes from Graphene Sheets. *Nano Letters* **8**, 2458–2462 (2008). DOI: 10.1021/nl801457b.

[8] Sun, P. Z. *et al.* Limits on gas impermeability of graphene. *Nature* **579**, 229–232 (2020). DOI: 10.1038/s41586-020-2070-x.

[9] Vasu, K. S. *et al.* Van der Waals pressure and its effect on trapped interlayer molecules. *Nature Communications* **7**, 12168 (2016). DOI: 10.1038/ncomms12168.

[10] Mirzayev, R. *et al.* Buckyball sandwiches. *Science Advances* **3**, e1700176 (2017). DOI: 10.1126/sciadv.1700176.

[11] Ye, X. *et al.* Single-particle mapping of nonequilibrium nanocrystal transformations. *Science* **354**, 874–877 (2016). DOI: 10.1126/science.aah4434.

[12] Yuk, J. M. *et al.* High-Resolution EM of Colloidal Nanocrystal Growth Using Graphene Liquid Cells. *Science* **336**, 61–64 (2012). DOI: 10.1126/science.1217654.

[13] Kühne, M. *et al.* Ultrafast lithium diffusion in bilayer graphene. *Nature Nanotechnology* **12**, 895–900 (2017). DOI: 10.1038/nnano.2017.108.

[14] Kühne, M. *et al.* Reversible superdense ordering of lithium between two graphene sheets. *Nature* **564**, 234–239 (2018). DOI: 10.1038/s41586-018-0754-2.

[15] Åhlgren, E. H., Hämäläinen, S. K., Lehtinen, O., Liljeroth, P. & Kotakoski, J. Structural manipulation of the graphene/metal interface with Ar + irradiation. *Physical Review B* **88**, 155419 (2013). DOI: 10.1103/PhysRevB.88.155419.

[16] Binnig, G. & Rohrer, H. SCANNING TUNNELING MICROSCOPY 9.

[17] Herbig, C. *et al.* Interfacial Carbon Nanoplatelet Formation by Ion Irradiation of Graphene on Iridium(111). *ACS Nano* **8**, 12208–12218 (2014). DOI: 10.1021/nn503874n.

[18] Herbig, C. *et al.* Comment on "Interfacial Carbon Nanoplatelet Formation by Ion Irradiation of Graphene on Iridium(111)". *ACS Nano* **9**, 4664–4665 (2015). DOI: 10.1021/acsnano.5b02303.

[19] Herbig, C. *et al.* Xe irradiation of graphene on Ir(111): From trapping to blistering. *Physical Review B* **92**, 085429 (2015). DOI: 10.1103/PhysRevB.92.085429.

[20] Herbig, C., Åhlgren, E. H. & Michely, T. Blister-free ion beam patterning of supported graphene. *Nanotechnology* **28**, 055304 (2017). DOI: 10.1088/1361-6528/aa527c.

[21] Yoo, S. *et al.* Growth kinetics of Kr nano structures encapsulated by graphene. *Nanotechnology* **29**, 385601 (2018). DOI: 10.1088/1361-6528/aad019.

[22] Horn, P. M., Birgeneau, R. J., Heiney, P. & Hammonds, E. M. Melting of Submonolayer Krypton Films on Graphite. *Physical Review Letters* **41**, 961–964 (1978). DOI: 10.1103/PhysRevLett.41.961.

[23] Butler, D. M., Litzinger, J. A., Stewart, G. A. & Griffiths, R. B. Heat Capacity of Krypton Physisorbed on Graphite. *Physical Review Letters* **42**, 1289–1292 (1979). DOI: 10.1103/PhysRevLett.42.1289.

[24] Gangwar, R. & Suter, R. M. Thermodynamics and phase diagram of multilayer krypton on graphite. *Physical Review B* **42**, 2711–2714 (1990). DOI: 10.1103/PhysRevB.42.2711.

[25] Specht, E. D., Sutton, M., Birgeneau, R. J., Moncton, D. E. & Horn, P. M. Phase diagram and phase transitions of krypton on graphite in the one-to-two-layer regime. *Physical Review B* **30**, 1589–1592 (1984). DOI: 10.1103/PhysRevB.30.1589.

[26] Specht, E. D. *et al.* Phase diagram and phase transitions of Krypton on graphite in the extended monolayer regime. *Zeitschrift für Physik B Condensed Matter* **69**, 347–377 (1987). DOI: 10.1007/BF01307294.

[27] Butler, D. M., Litzinger, J. A. & Stewart, G. A. Completion of the Phase Diagram for the Monolayer Regime of the Krypton-Graphite Adsorption System. *Physical Review Letters* **44**, 466–468 (1980). DOI: 10.1103/PhysRevLett.44.466.

[28] Day, P., LaMadrid, M., Lysek, M. & Goodstein, D. Multilayer krypton phase diagram. *Physical Review B* **47**, 7501–7507 (1993). DOI: 10.1103/PhysRevB.47.7501.

[29] Wallace, P. R. The Band Theory of Graphite. *Physical Review* **71**, 622–634 (1947). DOI: 10.1103/PhysRev.71.622.

[30] Peierls, R. E. Bemerkungen über Umwandlungstemperaturen. *Helv. Phys. Acta* **8**, 81–83 (1934).

[31] Peierls, R. Quelques propriétés typiques des corps solides. *Annales de l'institut Henri Poincaré* **5**, 177–222 (1935).

[32] Landau, L. Zur Theorie der phasenumwandlungen II. *Phys. Z. Sowjetunion* **11**, 26–35 (1937).

[33] Landau, L. D., Lifshitz, E. M. & Pitaevskii, L. P. *Statistical physics*. No. v. 5, 9 in Pergamon international library of science, technology, engineering, and social studies (Pergamon Press, Oxford ; New York, 1980).

[34] Mermin, N. D. Crystalline Order in Two Dimensions. *Physical Review* **176**, 250–254 (1968). DOI: 10.1103/PhysRev.176.250.

[35] Mermin, N. D. & Wagner, H. Absence of Ferromagnetism or Antiferromagnetism in One- or Two-Dimensional Isotropic Heisenberg Models. *Physical Review Letters* **17**, 1133–1136 (1966). DOI: 10.1103/PhysRevLett.17.1133.

[36] Meyer, J. C. *et al.* The structure of suspended graphene sheets. *Nature* **446**, 60–63 (2007). DOI: 10.1038/nature05545.

[37] Nair, R. R. *et al.* Fine Structure Constant Defines Visual Transparency of Graphene. *Science* **320**, 1308–1308 (2008). DOI: 10.1126/science.1156965.

[38] Blake, P. *et al.* Making graphene visible. *Applied Physics Letters* **91**, 063124 (2007). DOI: 10.1063/1.2768624.

[39] Geim, A. K. & Novoselov, K. S. The rise of graphene. *Nature Materials* **6**, 183–191 (2007). DOI: 10.1038/nmat1849.

[40] Gross, R. & Marx, A. *Festkörperphysik* (Oldenbourg Wissenschaftsverlag, 2012)URL .

[41] Tripathi, M. *Modifying low-dimensional materials using energetic charged particles* (Wien, 2019).

[42] Grosso, G. & Pastori Parravicini, G. *Solid state physics* (Academic Press, an imprint of Elsevier, Amsterdam, 2014), second edition edn.

[43] Novoselov, K. S. *et al.* Two-dimensional atomic crystals. *Proceedings of the National Academy of Sciences of the United States of America* **102**, 10451 (2005). DOI: 10.1073/pnas.0502848102.

[44] Bolotin, K. *et al.* Ultrahigh electron mobility in suspended graphene. *Solid State Communications* **146**, 351–355 (2008). DOI: 10.1016/j.ssc.2008.02.024.

[45] Balandin, A. A. *et al.* Superior Thermal Conductivity of Single-Layer Graphene. *Nano Letters* **8**, 902–907 (2008). DOI: 10.1021/nl0731872.

[46] Mayorov, A. S. *et al.* Micrometer-Scale Ballistic Transport in Encapsulated Graphene at Room Temperature. *Nano Letters* **11**, 2396–2399 (2011). DOI: 10.1021/nl200758b.

[47] Rik, B. (ed.) *Aberration-Corrected Analytical Transmission Electron Microscopy* (John Wiley & Sons, Ltd, 2011), 1 edn.URL .

[48] Tripathi, M. *et al.* Cleaning graphene: comparing heat treatments in air and in vacuum. *physica status solidi (RRL) - Rapid Research Letters* **11**, 1700124 (2017). ArXiv: 1704.08038, DOI: 10.1002/pssr.201700124.

[49] Meyer, J. C. *et al.* Accurate Measurement of Electron Beam Induced Displacement Cross Sections for Single-Layer Graphene. *Physical Review Letters* **108**, 196102 (2012). DOI: 10.1103/PhysRevLett.108.196102.

[50] Susi, T. *et al.* Isotope analysis in the transmission electron microscope. *Nature Communications* **7**, 13040 (2016). DOI: 10.1038/ncomms13040.

[51] Pantelic, R. S., Meyer, J. C., Kaiser, U. & Stahlberg, H. The application of graphene as a sample support in transmission electron microscopy. *Solid State Communications* **152**, 1375–1382 (2012). DOI: 10.1016/j.ssc.2012.04.038.

[52] Yi, M. & Shen, Z. A review on mechanical exfoliation for the scalable production of graphene. *Journal of Materials Chemistry A* **3**, 11700–11715 (2015). DOI: 10.1039/C5TA00252D.

[53] Huang, Y. *et al.* Reliable Exfoliation of Large-Area High-Quality Flakes of Graphene and Other Two-Dimensional Materials. *ACS Nano* **9**, 10612–10620 (2015). DOI: 10.1021/acsnano.5b04258.

[54] Meyer, J. C., Girit, C. O., Crommie, M. F. & Zettl, A. Hydrocarbon lithography on graphene membranes. *Applied Physics Letters* **92**, 123110 (2008). DOI: 10.1063/1.2901147.

[55] Scheinecker, D. *TEM SAED Analysis of Corrugations in Low-Dimensional Materials* (Vienna, 2019).

[56] Muñoz, R. & Gómez-Aleixandre, C. Review of CVD Synthesis of Graphene: Review of CVD Synthesis of Graphene. *Chemical Vapor Deposition* **19**, 297–322 (2013). DOI: 10.1002/cvde.201300051.

[57] Mortimer, C. E. & Müller, U. *Chemie: das Basiswissen der Chemie ; 520 Formelbilder, 125 Tabellen* (Thieme, Stuttgart, 2003), 8., komplett überarb. und erw. aufl edn. OCLC: 76564589.

[58] Schubert, K. Ein Modell für die Kristallstrukturen der chemischen Elemente. *Acta Crystallographica Section B Structural Crystallography and Crystal Chemistry* **30**, 193–204 (1974). DOI: 10.1107/S0567740874002469.

[59] Phillips, W. D. The end of artefacts. *Nature Physics* **15**, 518–518 (2019). DOI: 10.1038/s41567-019-0514-8.

[60] Linnell, J. A. & Gallimore, A. D. Efficiency Analysis of a Hall Thruster Operating with Krypton and Xenon. *Journal of Propulsion and Power* **22**, 1402–1418 (2006). DOI: 10.2514/1.19613.

[61] Williams, D. B. & Carter, C. B. *Transmission Electron Microscopy* (Springer US, 2009)URL .

[62] Demtröder, W. Optische Instrumente. In *Experimentalphysik 2*, 331–353 (Springer Berlin Heidelberg, Berlin, Heidelberg, 2017)URL .

[63] Recherches sur la théorie des quanta (Researches on the quantum theory), Thesis (Paris), 1924; L. de Broglie, Ann. Phys. (Paris) 3, 22 (1925). *Ann. Phys. (Paris)* **3** (1925).

[64] Egerton, R. F. *Electron Energy-Loss Spectroscopy in the Electron Microscope* (Springer US, 2011), 3 edn.URL .

[65] Scherzer, O. Über einige Fehler von Elektronenlinsen. *Zeitschrift für Physik* **101**, 593–603 (1936). DOI: 10.1007/BF01349606.

[66] Scherzer, O. Spharische und chromatische korrektur von elktronen-linsen. *Optik* **2**, 114 (1947).

[67] Krivanek, O. L., Dellby, N., Spence, A. J., Camps, R. A. & Brown, L. M. Aberration correction in the STEM. *Inst. Phys. Conf. Ser. 153 (Proceedings 1997 EMAG meeting) Ed. Rodenburg JM* **35** (1997).

[68] Krivanek, O. L., Dellby, N. & Lupini, A. R. Towards sub-As electron beams 11 (1999).

[69] Batson, P. E., Dellby, N. & Krivanek, O. L. Sub-ångstrom resolution using aberration corrected electron optics. *Nature* **418**, 617–620 (2002). DOI: 10.1038/nature00972.

[70] Dellby, N., Krivanek, O. L., Nellist, P. D., Batson, P. E. & Lupini, A. R. Progress in aberration-corrected scanning transmission electron microscopy. *Microscopy* **50**, 177–185 (2001). DOI: 10.1093/jmicro/50.3.177.

[71] Crewe, A. V., Wall, J. & Langmore, J. Visibility of Single Atoms. *Science* **168**, 1338–1340 (1970). DOI: 10.1126/science.168.3937.1338.

[72] Crewe, A. V. The physics of the high-resolution scanning microscope. *Reports on Progress in Physics* **43**, 621–639 (1980). DOI: 10.1088/0034-4885/43/5/002.

[73] Pennycook, S. & Jesson, D. High-resolution Z-contrast imaging of crystals. *Ultramicroscopy* **37**, 14–38 (1991). DOI: 10.1016/0304-3991(91)90004-P.

[74] Krivanek, O. L. *et al.* Atom-by-atom structural and chemical analysis by annular dark-field electron microscopy. *Nature* **464**, 571–574 (2010). DOI: 10.1038/nature08879.

[75] Krivanek, O. *et al.* An electron microscope for the aberration-corrected era. *Ultramicroscopy* **108**, 179–195 (2008). DOI: 10.1016/j.ultramic.2007.07.010.

[76] EELS.infoURL .

[77] Wolf, B. H. & Company, C. R. (eds.) *Handbook of ion sources* (CRC Press, Boca Raton, 1995). OCLC: 246955207.

[78] Hjorth Larsen, A. *et al.* The atomic simulation environment—a Python library for working with atoms. *Journal of Physics: Condensed Matter* **29**, 273002 (2017). DOI: 10.1088/1361-648X/aa680e.

[79] scipy.ndimage.map_coordinates — SciPy v1.4.1 Reference GuideURL .

[80] Susi, T. *et al.* Efficient first principles simulation of electron scattering factors for transmission electron microscopy. *Ultramicroscopy* **197**, 16–22 (2019). DOI: 10.1016/j.ultramic.2018.11.002.

[81] Kirkland, E. J. *Advanced computing in electron microscopy* (Plenum Press, New York, 1998).

[82] Biersack, J. Calculation of projected ranges — analytical solutions and a simple general algorithm. *Nuclear Instruments and Methods* **182-183**, 199–206 (1981). DOI: 10.1016/0029-554X(81)90688-1.

[83] Biersack, J. P. New projected range algorithm as derived from transport equations. *Zeitschrift für Physik A Atoms and Nuclei* **305**, 95–101 (1982). DOI: 10.1007/BF01415015.

[84] Ziegler, J. F., Biersack, J. P. & Ziegler, M. D. *SRIM: the stopping and range of ions in matter* (SRIM Co, Chester, Md, 2008). OCLC: 845361947.

[85] Schimel, J. *Writing science: how to write papers that get cited and proposals that get funded* (Oxford University Press, Oxford ; New York, 2012). OCLC: ocn738354410.

[86] Inani, H. *et al.* Silicon Substitution in Nanotubes and Graphene via Intermittent Vacancies. *The Journal of Physical Chemistry C* acs.jpcc.9b01894 (2019). DOI: 10.1021/acs.jpcc.9b01894.